Acceleration Sensing, Feedback Cooling, and Nonlinear Dynamics with Nanoscale Cavity-Optomechanical Devices

Thesis by

Alexander Grey Krause

In Partial Fulfillment of the Requirements

for the Degree of

Doctor of Philosophy

California Institute of Technology

Pasadena, California

2015

(Defended February 4th, 2015)

Acknowledgments

I've been incredibly lucky to have recieved great help from family, friends, and colleagues. Your support has meant everything to me and I would like to give some small measure of the appropriate thanks here. First, to my father for discussing relativity with me in kindergarten and to my mother for always asking how my day was. To Erica, who helped keep me grounded. To Libby for never giving up on me more than once. To Kerry Walton for being generous and a role model in life.

To Oskar, I'll always appreciate the knowledge and experience I gained working with you. Ever since I started working in the lab as a lowly undergraduate, your mentorship has been invaluable. You helped make me the scientist I am today.

Also, to my past scientific advisers I owe a great debt. To Rudolpho Llinás for accepting me to work in his lab for my first research experience. To Anna Swan, because your patience with my (slow) development as a scientist seemed infinite. To Nick Vamivakas for teaching me that science should be slow and careful. Finally, to Florian Marquardt for your guidance and well wishes.

To my Oklahoma friends, thank you for always being there (both literally and figuratively): Andrew Ruffin, Jake Kelley, Courtney Klein, Chris Hardin, Ben Dabiri, and others.

To my BU friends, thank you for putting up with how much less fun I've become since studying at CalTech. To Claire Thomas, surprisingly, for your good advice. To Ted Stinson for being great. To Tessa for trying (usually in vain) to keep all of us honest. To Emily Hostage for never letting time nor distance change our friendship.

Thank you to everyone in the Painter Group and at Caltech that made this experience enjoyable. To Jeff Bosco for helping me learn how to climb. To Shaun Maguire thank you for teaching me the value of networking, and more importantly, how to do it without being obnoxious. To my comrades in arms, Ari Weinstein, Laura DeLorenzo, and Emma Wollman. To Justin and Sean for commiserating. To Jasper Chan for teaching me to have the humility to just let the machines do the work. To Tim Blasius for being a great colleague and helping me learn that there are important things outside of the lab... but mostly for putting up with me. To Martin Winger for his beautiful code (and hair). To Simon Gröblacher for BBQ. To Jeff Hill for always being a devil's advocate, but also for never giving up. To Amir Safavi-Naeini for his friendship, and mentorship. To my library-buddy Norte, 'geeteefo'. And to everyone else in the group, thank you!

And finally, to Tyler; you've helped me more than you will ever know. For Science.

Abstract

Light has long been used for the precise measurement of moving bodies, but the burgeoning field of optomechanics is concerned with the interaction of light and matter in a regime where the typically weak radiation pressure force of light is able to push back on the moving object. This field began with the realization in the late 1960's that the momentum imparted by a recoiling photon on a mirror would place fundamental limits on the smallest measurable displacement of that mirror. This coupling between the frequency of light and the motion of a mechanical object does much more than simply add noise, however. It has been used to cool objects to their quantum ground state, demonstrate electromagnetically-induced-transparency, and modify the damping and spring constant of the resonator. Amazingly, these radiation pressure effects have now been demonstrated in systems ranging 18 orders of magnitude in mass (kg$\leftrightarrow$fg).

In this work we will focus on three diverse experiments in three different optomechanical devices which span the fields of inertial sensors, closed-loop feedback, and nonlinear dynamics. The mechanical elements presented cover 6 orders of magnitude in mass (ng$\leftrightarrow$fg), but they all employ nano-scale photonic crystals to trap light and resonantly enhance the light-matter interaction. In the first experiment we take advantage of the sub-femtometer displacement resolution of our photonic crystals to demonstrate a sensitive chip-scale optical accelerometer with a kHz-frequency mechanical resonator. This sensor has a noise density of ≈ 10 μg/rt-Hz over a useable bandwidth of ≈ 20 kHz and we demonstrate at least 50 dB of linear dynamic sensor range. We also discuss methods to further improve performance of this device by a factor of 10.

In the second experiment, we used a closed-loop measurement and feedback system to damp and cool a room-temperature MHz-frequency mechanical oscillator from a phonon occupation of 6.5×10^6 down to 66. At the time of the experiment, this represented a world-record result for the laser cooling of a macroscopic mechanical element without the aid of cryogenic pre-cooling. Furthermore, this closed-loop damping yields a high-resolution force sensor with a practical bandwidth of 200 kHZ and the method has applications to other optomechanical sensors.

The final experiment contains results from a GHz-frequency mechanical resonator in a regime where the nonlinearity of the radiation-pressure interaction dominates the system dynamics. In this device we show self-oscillations of the mechanical element that are driven by multi-photon-phonon

scattering. Control of the system allows us to initialize the mechanical oscillator into a stable high-amplitude attractor which would otherwise be inaccessible.

To provide context, we begin this work by first presenting an intuitive overview of optomechanical systems and then providing an extended discussion of the principles underlying the design and fabrication of our optomechanical devices.

Contents

List of Figures

List of Tables

Chapter 1

Classical Theory of Optomechanical Systems

In this section, we will introduce a conceptual model of an optomechanical system and then derive the governing equations and basic optomechanical relations. We will first do this in an intuitive model typically used for experiments with low-frequency classical optomechanical systems. Then we will present a second more complete formalism appropriate for optomechanics in nonlinear and high-frequency systems. Experimental results employing both descriptions will be presented in this thesis.

1.1 Introduction

The standard example of an optomechanical system is that of a Fabry-Pérot optical cavity consisting of two opposing mirrors which trap light between them, but one of the mirrors is free to oscillate (Fig. 1.1). Due to the boundary condition imposed by the mirrors, only an integer number of wavelengths can fit inside the optical cavity, of total effective length, $\mathrm{L_{eff}}$. This causes the cavity to have a series of optical resonances around the discreet frequencies where this integer condition is met, $\omega_\mathrm{j}/2\pi = \mathrm{j}\frac{\mathrm{c}}{2\mathrm{L_{eff}}}$, where j is an integer, and c is the speed of light in free space. Since the resonances are determined by the effective length, small changes in this length due to the moving end-mirror change the optical resonance according to $\omega_\mathrm{j} = \mathrm{j}\frac{\pi \mathrm{c}}{\mathrm{L_{eff}}+x(t)}$. This modulation changes the light inside the cavity and thus modulates the amount of outgoing light from the optical cavity, allowing one to detect the mirror's motion. This simple effect is useful for sensitively measuring displacements.

However, there is another effect to consider because the light inside the cavity also exerts a radiation pressure force back onto the moveable mirror. Thus, if the mirror is small enough, or there is enough light inside the cavity, the mirror can be pushed around by this optical photon pressure. This additional effect causes optomechanical systems to be full of interesting dynamics

because this force can change the mirror's position, which then changes the amount of force on the mirror, causing a change in the mirror's motion, etc. etc. etc. These dynamics allow one to use the light to effectively stiffen or soften the spring the mirror is attached to, as well as amplify or damp the mirror's motion [1].

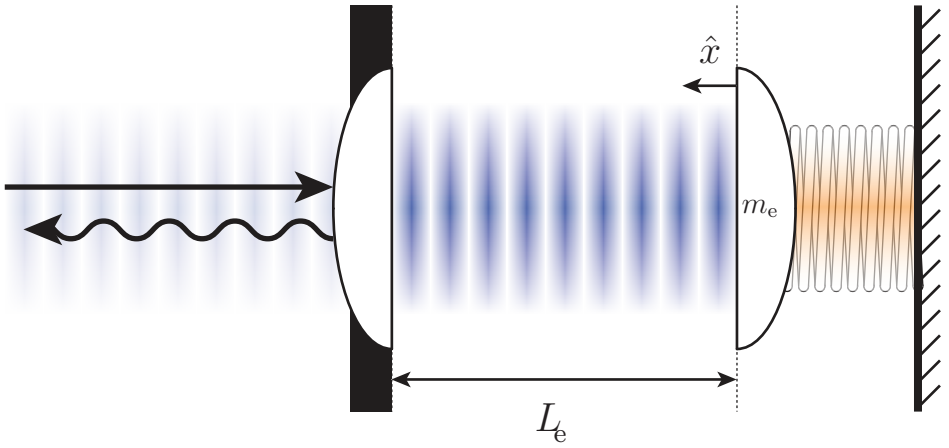

Figure 1.1: **Fabry-Perot Cavity.** The two mirrors trap the incoming resonant light (blue) between them. The left mirror is slightly less reflective in order to allow light to couple into and out of the optical cavity. The right mirror is free to oscillate with its energy stored in a simple spring (orange). This motion, x, changes the effective length of the cavity, $\mathrm{L_{eff}}$, which modulates the light inside of the cavity, and causes the outgoing light to be modulated.

In the following sections, we will dive into the details of this coupling, and in later chapters present optomechanical systems that have little apparent resemblance to Fig. 1.1, but keep in mind that nearly all of the relevant physics in these devices is contained within this simple model system of mirrors and a spring.

1.2 Sideband Unresolved Optomechanics

The following formalism is most convenient when describing low-frequency systems where the mechanical frequency, ω_{m}, is much slower than the optical energy decay rate, κ. When this is the case, $\omega_{\mathrm{m}} \ll \kappa$, light can enter and exit the optical cavity much faster than the mechanical mode undergoes one oscillation. This allows some simplifications, and it is useful for the intuitive picture it provides, but can lead to errors when considering systems with too-fast mechanical frequencies, $\omega_{\mathrm{m}} \gtrsim \kappa$ (see Section 1.3).

Starting from our equation for the resonance frequency in the Fabry-Pérot cavity, we consider only one particular optical cavity resonance with bare frequency, $\omega_{\mathrm{c},0} \equiv k\frac{\pi \mathrm{c}}{\mathrm{L_{eff}}}$, which is modified by the mechanical motion to $\omega_{\mathrm{c}}(t) = \frac{\omega_{\mathrm{c},0}}{1+x(t)/\mathrm{L_{eff}}}$. We can further assume that the displacement is small relative to the effective length of the cavity, $|x| \ll \mathrm{L_{eff}}$, which is valid for every experiment presented

here. This allows us to expand the changes to the optical frequency in a Taylor series:

$$\begin{aligned}\omega_{\mathrm{c}}(t) &= \omega_{\mathrm{c},0} + \frac{d\omega_{\mathrm{c},0}}{dx}x(t) + \frac{1}{2!}\frac{d^2\omega_{\mathrm{c},0}}{dx^2}x^2(t) + \ldots \\ &= \omega_{\mathrm{c},0} - \frac{\omega_{\mathrm{c},0}}{\mathrm{L_{eff}}}x(t) + \frac{1}{2}\frac{\omega_{\mathrm{c},0}^2}{\mathrm{L_{eff}^2}} + \ldots.\end{aligned} \tag{1.1}$$

We have truncated the series after the first two terms because in practice these are the most experimentally relevant. All of the work presented here, including the nonlinear work discussed in Chapter 5, is still well within the regime where the first term, linear in $\frac{\omega_{\mathrm{c},0}}{\mathrm{L_{eff}}}$, dominates. Engineering systems where the linear term is absent or small compared to the x^2 term is of recent interest for quantum measurement applications, but will not be discussed here (see [2–10]).

Finally, we get this form for the coupling between the two systems, $\omega_{\mathrm{c}} = \omega_{\mathrm{c},0} - g_{\mathrm{OM}}x(t)$, where the frequency change per unit displacement of the optical cavity is defined by $g_{\mathrm{OM}} = \frac{d\omega_{\mathrm{c},0}}{dx} = \frac{\omega_{\mathrm{c},0}}{\mathrm{L_{eff}}}$. This constant, g_{OM}, is known as the optomechanical coupling strength and it is a critical parameter because it sets the amount of information imparted on the optical field by the mechanical motion, as well as the amount of radiation force transferred from the optical field to the mechanical resonator.

The connection between g_{OM} and the optical force can be seen by considering the interaction Hamiltonian of this system:

$$H_{\mathrm{int}} = -\hbar n_{\mathrm{c}} g_{\mathrm{OM}} x, \tag{1.2}$$

where $n_{\mathrm{c}} = a^\dagger a$ is the number of photons stored in the optical cavity, with a ($a^\dagger$) representing the destruction (creation) operator of the optical field. Classically, then, the force on the oscillator is given by $F_{\mathrm{rp}} = -\frac{dH_{\mathrm{int}}}{dx} = \hbar n_{\mathrm{c}} g_{\mathrm{OM}}$. A single photon inside the optical cavity 'pushes' on the mechanical element by an amount $\hbar g_{\mathrm{OM}}$, and thus displaces the mirror by an amount, $\Delta x = \frac{\hbar g_{\mathrm{OM}}}{\mathrm{k}}$, where k is the system spring constant. From these relations, one can see that systems with large optomechanical couplings and low mechanical stiffness will be ideal for observing effects of the light-field acting on the mechanical resonator.

1.2.1 Equations of Motion

To derive these effects, we start with the standard equations of motion for the mechanical position, x, and the optical field, a:

$$\dot{a}(t) = -i\left(\omega_{\rm c} - x\left(t\right) g_{\rm OM}\right) a(t) - \frac{\kappa}{2} a(t) + \sqrt{\kappa_{\rm in}} a_{\rm in}(t) \tag{1.3}$$

$$\ddot{x}(t) = -\gamma_{\rm i}\dot{x}(t) - \omega_{\rm m}^2 x(t) + \frac{F_{\rm th}}{m_{\rm eff}} + \frac{\hbar g_{\rm OM}}{m_{\rm eff}} n_{\rm c}(t)\,, \tag{1.4}$$

where to describe the optical mode we have defined the bare optical resonance frequency $\omega_{\rm c}$, the total optical cavity field decay rate κ, the input coupling rate $\kappa_{\rm in}$, and the input driving laser field $a_{\rm in}$. For the mechanical mode, we have used $\gamma_{\rm i}$ as the intrinsic mechanical decay rate, $\omega_{\rm m}$ as the angular resonance frequency, and $m_{\rm eff}$ as the effective motional mass of the mechanical mode (which is not, in general, equal to the physical mass). Also, we account for thermal noise to drive the oscillator in the term $F_{\rm th}$. It is important to note here that the number of photons in the cavity is calculated from the optical cavity field as $n_{\rm c}(t) = |a(t)|^2$ because we are treating the system classically. Thus, in general, the dynamics of the system are governed by two coupled differential equations which are not linear in their interaction.

First, because the optical frequency is almost always much much larger than any other frequency in the system ($\omega_{\rm c}/2\pi \approx 200$ THz), it is useful to solve for the slowly varying amplitude of the field $\tilde{a}$. To do this, we first note that if we are driving the system with a single laser at frequency ω_ℓ, then the input field is given by $a_{\rm in}(t) = a_{\rm in} e^{-i\omega_\ell t}$, where the input rate of photons is $a_{\rm in} = \sqrt{\frac{P_{\rm in}}{\hbar\omega_\ell}}$, with $P_{\rm in}$ the laser power. So, we can solve for $\tilde{a}$ by making the substitution $a(t) = \tilde{a}(t)\, e^{-i\omega_\ell t}$ in Eq. (1.3):

$$\dot{\tilde{a}}(t) - i\omega_\ell \tilde{a}(t) = -i\left(\omega_{\rm c} - x\left(t\right) g_{\rm OM}\right) \tilde{a}(t) - \frac{\kappa}{2}\tilde{a}(t) + \sqrt{\kappa_{\rm in}} a_{\rm in} \tag{1.5}$$

$$\dot{\tilde{a}} = i\left(\Delta + x\left(t\right) g_{\rm OM}\right) \tilde{a}(t) - \frac{\kappa}{2}\tilde{a}(t) + \sqrt{\kappa_{\rm in}} a_{\rm in}, \tag{1.6}$$

where we have defined the detuning of the laser from the cavity as $\Delta = \omega_\ell - \omega_{\rm c}$, so that the detuning is negative when the laser has a lower frequency than the optical resonance. Now, for simplicity, we replace $\tilde{a} = a$, with the implicit understanding, that we're now solving the equations in a rotating frame and we've just dropped the tildes. Here we restate these equations for clarity:

$$\dot{a}(t) = i\left(\Delta + x(t)\, g_{\rm OM}\right) a(t) - \frac{\kappa}{2} a(t) + \sqrt{\kappa_{\rm in}} a_{\rm in}(t) \tag{1.7}$$

$$\ddot{x}(t) = -\gamma_{\rm i}\dot{x}(t) - \omega_{\rm m}^2 x(t) + F_{\rm th}/m_{\rm eff} + \frac{\hbar g_{\rm OM}}{m_{\rm eff}} n_{\rm c}(t)\,. \tag{1.8}$$

1.2.2 Mechanical Mode Solution

In general, the coupled set of equations, (1.7) & (1.8), is nonlinear and cannot be solved analytically. However, in practice, the optomechanical coupling g_{OM} and the mechanical amplitudes x are small enough that an iterative approach yields accurate results. First, then, we will drop the optical coupling ($g_{\text{OM}} = 0$), and solve for the behavior of the mechanical mode. We start by Fourier transforming (1.8):

$$-\omega^2 x(\omega) = i\gamma_{\text{i}}\omega x(\omega) - \omega_{\text{m}}^2 x(\omega) + \mathcal{F}_{\text{th}}/m_{\text{eff}}, \tag{1.9}$$

where we have used the property of the Fourier transform, $\mathcal{F}\left[\dot{x}(t)\right] = i\omega x(\omega)$ (see Appendix A), and defined $\mathcal{F}\left[F_{\text{th}}(t)\right] = \mathcal{F}_{\text{th}}(\omega)$. Now, solving for the displacement spectrum of x, we find:

$$x(\omega) = \frac{1}{\omega^2 - \omega_{\text{m}}^2 + i\gamma_{\text{i}}\omega}\frac{\mathcal{F}_{\text{th}}}{m_{\text{eff}}} = \chi(\omega)\,\frac{\mathcal{F}_{\text{th}}}{m_{\text{eff}}}, \tag{1.10}$$

where it is useful to define the oscillator's susceptibility as $\chi(\omega) = \left(\omega^2 - \omega_{\text{m}}^2 + i\gamma_{\text{i}}\omega\right)^{-1}$. This function has a standard Lorentzian shape near resonance, and has the other following notable properties:

$$\chi\left(0\right) = \frac{1}{\omega_{\text{m}}^2} = \frac{m_{\text{eff}}}{\text{k}}, \tag{1.11}$$

$$\chi\left(\omega_{\text{m}}\right) = -i\frac{Q_{\text{m}}}{\omega_{\text{m}}^2} = -iQ_{\text{m}}\chi\left(0\right), \tag{1.12}$$

$$\left|\chi\left(\omega \gg \omega_{\text{m}}\right)\right| \propto \frac{1}{\omega_{\text{m}}^2}. \tag{1.13}$$

Here we have used the quality factor of the mechanical mode, $Q_{\text{m}} = \omega_{\text{m}}/\gamma$. Obtaining mechanical resonators with large Q_{m} (i.e., good quality) will prove to be an important subject of this work. Physically, it is related to the number of oscillations, $\#_{\text{osc}}$, that a resonator undergoes before its energy decays to $1/e \approx 37\%$ of its initial value: $Q_{\text{m}}/2\pi = \#_{\text{osc}}$. A diagram of the susceptibility function is shown in Fig. 1.2.

The term $\mathcal{F}_{\text{th}}$ arises from the oscillator being in equilibrium with a heat bath and is thus subject to thermal Brownian motion. The equipartition theorem tells us that the root-mean-square (RMS) displacement of a harmonic oscillator subject to this noise must be

$$x_{\text{rms}}^2 = \frac{k_{\text{B}}T_{\text{b}}}{\text{k}} = \frac{k_{\text{B}}T_{\text{b}}}{m_{\text{eff}}\omega_{\text{m}}^2}, \tag{1.14}$$

where we have used the temperature of the thermal bath T_{b} and Boltzmann's constant k_{B}.

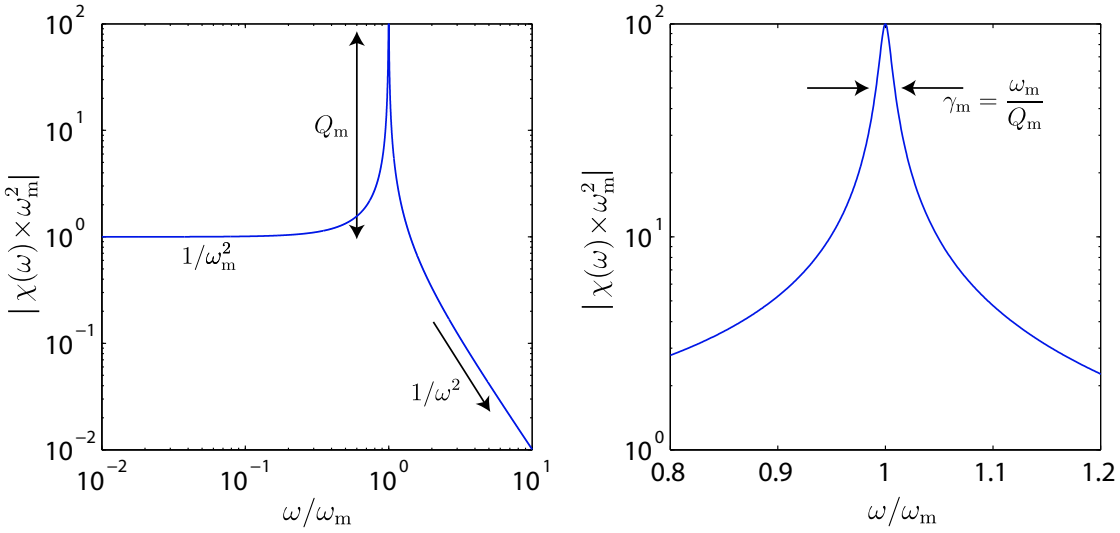

Figure 1.2: **Resonator Susceptibility.** (**a**) Widespan plot of the normalized magnitude of the resonator susceptibility $|\chi(\omega)\,\omega_{\rm m}^2|$ with $Q_{\rm m} = 100$. (**b**) Plot of $\chi(\omega)$ near resonance indicating that the full-width-at-half-max of this curve is the mechanical damping rate γ.

Also, we have the additional relation that integrating this force noise over the susceptibility must be equal to the RMS displacement,

$$x_{\rm rms}^2 = \int_0^\infty |\chi(\omega)\,|^2 S_{\rm ff}^{\rm th}, \tag{1.15}$$

where we have denoted the spectral density of the thermal force noise as $S_{\rm ff}^{\rm th}$. We assume this force noise to be spectrally-white (e.g., no frequency dependence). Equating Eqs. (1.14),(1.15) and integrating over the susceptibility function, we find the magnitude of this thermal noise to be

$$S_{\rm ff}^{\rm th} = \frac{4k_{\rm B}T_{\rm b}\gamma_{\rm i}}{m_{\rm eff}} = \frac{4k_{\rm B}T_{\rm b}\omega_{\rm m}}{m_{\rm eff}Q_{\rm m}}. \tag{1.16}$$

This spectral density has units of Force^2/Hz and is related to the original force noise in the equation of motion (Eq. (1.8)) via its autocorrelation, $S_{ff}(\omega) = \int_{-\infty}^{\infty} d\omega' \langle \mathcal{F}_{\rm th}^*(\omega)\,\mathcal{F}_{\rm th}(\omega')\rangle$, where $\mathcal{F}_{\rm th}^*$ is the complex conjugate of the thermal force noise spectrum $\mathcal{F}_{\rm th}$.

We now finally have an equation for the displacement spectrum of our thermally driven oscillator:

$$S_{\rm xx}^{\rm th}(\omega) = S_{\rm ff}^{\rm th}/m_{\rm eff}|\chi(\omega)\,|^2 = \frac{4k_{\rm B}T_{\rm b}\omega_{\rm m}m_{\rm eff}}{Q_{\rm m}}\frac{1}{\left(\omega^2-\omega_{\rm m}^2\right)^2+\left(\gamma_{\rm i}\omega\right)^2}, \tag{1.17}$$

which has units of meters^2/Hz.

This unavoidable thermal noise on the mechanical element will be relevant in our discussion of an optomechanical accelerometer in Chapter 3 and our attempt to cool our mechanical object in Chapter 4.

1.2.2.1 Quantum 'Mechanics'

Although this thesis will not cover any experiments that observe quantum effects, reaching such a regime is the motivation for the feedback cooling experiment in Chapter 4 and we will use the language of quantum mechanics to discuss the results, so we briefly introduce it here. The starting point for this analysis is to write the displacement operator in terms of the operators for creation ($\hat{b}^\dagger$) and annihilation ($\hat{b}$) of the mechanical mode, $\hat{x} = x_{\rm zp}\left(\hat{b}^\dagger + \hat{b}\right)$, ehere the proper normalization is that of the quantum zero-point (ground-state) amplitude $x_{\rm zp} = \sqrt{\frac{\hbar}{2m_{\rm eff}\omega_{\rm m}}}$. Similar to photons for the optical field, the quantum of mechanical excitations is the phonon and the number operator is given by $\hat{n}_b = \hat{b}^\dagger\hat{b}$. A thermal state again is one which is in equilibrium with a bath at a given temperature, and the phonons are described by a Maxwell-Boltzmann distribution:

$$\langle\hat{n}_b\rangle = \langle\hat{b}^\dagger\hat{b}\rangle = \frac{1}{e^{\frac{\hbar\omega_{\rm m}}{k_{\rm B}T_{\rm b}}} - 1} \approx \frac{k_{\rm B}T_{\rm b}}{\hbar\omega_{\rm m}}, \tag{1.18}$$

where we have used in the final expression the high-temperature approximation, which is valid for $\langle\hat{n}_b\rangle \gg 1$. It can be easily verified that this relation for $\langle\hat{n}_b\rangle$ leads to the same thermal displacement as in the classical case, namely, $\langle\hat{x}\rangle = x_{\rm rms} = k_{\rm B}T_{\rm b}/m_{\rm eff}\omega_{\rm m}^2$. The quantum regime is typically defined as one where $\langle\hat{n}_b\rangle < 1$, which has recently been achieved in a number of optomechanical systems [11–13].

1.2.3 Optical Mode Solution

Similar to the mechanical case, we start by first dropping the mechanics ($g_{\rm OM} = 0$) and solving for the steady state of the optical field, $\dot{a} = 0$:

$$a = \frac{\sqrt{\kappa_{\rm in}}a_{\rm in}}{\frac{\kappa}{2} - i\Delta} \tag{1.19}$$

$$n_{\rm c} = |a|^2 = a^*a = \frac{\kappa_{\rm in}a_{\rm in}^2}{\left(\frac{\kappa}{2}\right)^2 + \Delta^2} = \frac{\kappa_{\rm in}}{\left(\frac{\kappa}{2}\right)^2 + \Delta^2}\frac{P_{\rm in}}{\hbar\omega_\ell}. \tag{1.20}$$

The intracavity field, a, typically cannot be directly observed, and so although the mechanical mode experiences $n_{\rm c}$, the experimenter only has access to the transmitted or reflected outgoing optical field $a_{\rm out}$. The form for this outgoing field in terms of the input field can be found from standard

input-output theory [14] as

$$a_{\text{out}} = a_{\text{in}} - \sqrt{\kappa_{\text{in}}}a \tag{1.21}$$

$$= a_{\text{in}}\left(1 - \frac{\kappa_{\text{in}}}{\frac{\kappa}{2} - i\Delta}\right). \tag{1.22}$$

But this light field is detected on a photodetector that is sensitive only to the incident optical power so the detected signal is,

$$\mathrm{T}_{\text{det}} = \hbar\omega_\ell |a_{\text{out}}|^2 = \hbar\omega_\ell a_{\text{in}}^2 \left(1 - \frac{\kappa_{\text{in}}\left(\kappa - \kappa_{\text{in}}\right)}{\left(\frac{\kappa}{2}\right)^2 + \Delta^2}\right). \tag{1.23}$$

It is useful to note that $|a_{\text{out}}|^2$ and $|a_{\text{in}}|^2$ have units of photons/s, whereas $|a|^2$ has only units of photon number, so one must be careful switching between the intracavity field and the detected signal.

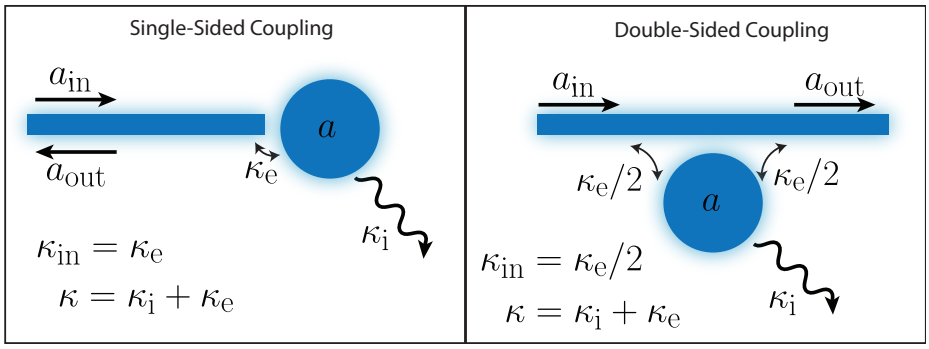

Figure 1.3: **Single & Double-Sided Coupling.** (a) Single-sided coupling showing a waveguide (blue rectangle) that carries the input optical field a_{in} and the reflected optical field a_{out}. It couples this light into the optical cavity (blue circle, a) at the extrinsic coupling rate $\kappa_{\text{in}} = \kappa_{\text{e}}$. The optical cavity also has an intrinsic loss rate, κ_{i}. (b) In a double-sided coupling scheme, the input light is coupled into the cavity at $\kappa_{\text{e}}/2$, and the output light a_{out} is transmitted past the optical cavity. The optical cavity can now couple to the waveguide in both forward and backward directions at rate $\kappa_{\text{e}}/2$, so light is still lost from the cavity at the same total rate $\kappa = \kappa_{\text{i}} + 2 * \kappa_{\text{e}}/2$. Half of the intracavity light ends up being 'lost' when it is emitted in the backwards direction.

1.2.3.1 Single Sided and Double Sided Cavities

So far we have only stated that κ is the total decay rate of the optical cavity, but we have not discussed what goes into this loss rate. This is because there are two distinct schemes, for coupling light into the cavity, and it has a large effect on the observed transmission signal. The two coupling schemes as shown in Fig. 1.3a, are called single and double-sided couplings because of the number of

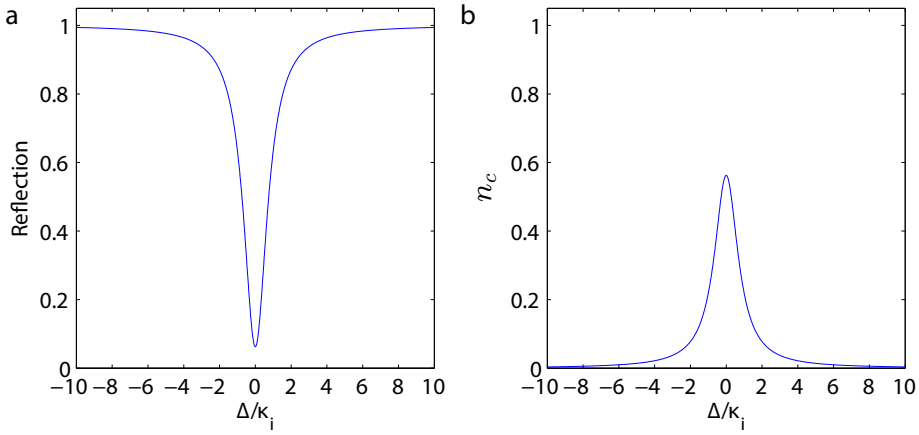

Figure 1.4: **Cavity Transmission & Photon Number.** (a) Plot of the normalized reflection of light from a single-sided optical cavity using Eq. (1.23) with $\kappa_{\rm in} = \kappa_{\rm e}, \kappa_{\rm e}/\kappa_{\rm i} = 0.6$ (b) Plot of the intracavity photon number for the same parameters as in (a), using Eq. (1.20) and setting $a_{\rm in} = \sqrt{\kappa_{\rm in}}$.

routes that light has to exit the cavity. The optical decay rate is typically split into two components. The first is an intrinsic component, $\kappa_{\rm i}$, which is the rate at which photons are inherently lost due to imperfect mirrors, absorption, or defects. The second is the extrinsic component, $\kappa_{\rm e}$, which is loss rate intentionally added to couple laser light into and out of the optical cavity.

In both systems, $\kappa = \kappa_{\rm i} + \kappa_{\rm e}$, but the difference is the rate at which light couples into/out of the system. In the single-sided cases, light leaving the optical cavity has only one direction to emit into (reflection) see Fig. 1.3a, but in the double-sided case, the waveguide is coupled in such a way as to allow light to leave either forward (transmission) or backward (reflection),see Fig. 1.3b. Thus, for single-sided cavities, $\kappa_{\rm in} = \kappa_{\rm e}$, but for double-sided cavities, $\kappa_{\rm in} = \kappa_{\rm e}/2$.

An example of the reflection spectrum from a single-sided optical cavity is shown in Fig. 1.4a, along with the intracavity photon number in Fig. 1.4b. A comparison of the transmitted and reflected spectrum for the two types of coupling is presented in Fig. 1.5. For single-sided coupling, the reflection directly on resonance is 0 for the special condition when $\kappa_{\rm e}/\kappa_{\rm i} = 1$, shown as the green line in Fig. 1.4b. This indicates that all of the input power couples into the optical cavity. For the double-sided cavity, this limit of complete power absorption only happens at $\kappa_{\rm e}/\kappa_{\rm i} = \infty$, where the cavity linewidth is also going to $+\infty$. Results from a single-sided sideband unresolved cavity experiment will be presented in Chapter 3 and experimental results using a single-sided cavity will be discussed in Chapter 4, where the main difference is that in a double-sided cavity, half of the information about the mechanical motion is lost to the backward direction. Explicitly, the upper-limit on detection efficiency is the ratio of photons emitted into the waveguide compared to the total photon loss rate, $\eta_{\rm max} = \kappa_{\rm in}/\kappa$. It can easily be shown that for the double-sided case, $\eta_{\rm max}$ cannot be greater than $\frac{1}{2}$.

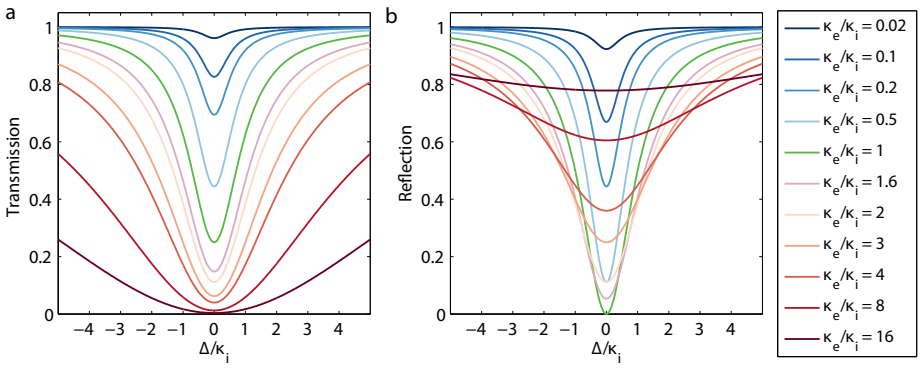

Figure 1.5: **Over and Under Coupled.** Plot of the transmission/reflection spectrum for double-sided (a) and single-sided (b) optical cavities for a wide range of the coupling ratio κ_e/κ_i. Note the difference in the curves at the value $\kappa_e/\kappa_i = 1$ (green), whereas for single-sided coupling, there is no reflected light.

The value of transmission (reflection) on resonance, $T(\Delta = 0)$, is commonly called the 'transmission dip' and is given by

$$T_d = \frac{\left(\frac{\kappa}{2} - \kappa_{in}\right)^2}{\left(\frac{\kappa}{2}\right)^2}, \tag{1.24}$$

$$= \frac{(\kappa_i - \kappa_e)^2}{\kappa^2}, \quad \text{when} \quad \kappa_{in} = \kappa_e, \tag{1.25}$$

$$= \frac{\kappa_i^2}{\kappa^2}, \quad \text{when} \quad \kappa_{in} = \frac{\kappa_e}{2}. \tag{1.26}$$

Since experimentally it is difficult to measure κ_{in}, but simple to measure T_d, this equation is usually inverted to solve for κ_{in}. However, it should be noted that for single-sided cavities, $\kappa_{in} = \kappa_e$, the resulting equation has two different solutions for κ_{in} for each T_d, corresponding to the oscillator being either over-coupled $\kappa_e > \kappa_i$ or under-coupled $\kappa_e < \kappa_i$. Therefore, establishing κ_{in} from T_d in this situation requires some other additional information to determine which solution is valid. In Chapter 4 we do this by measuring the total efficiency of the system.

1.2.3.2 Detecting Mechanical Motion

The effect of the mechanical motion on the transmitted signal is, to first order, proportional to the derivative of the transmitted signal with respect to detuning:

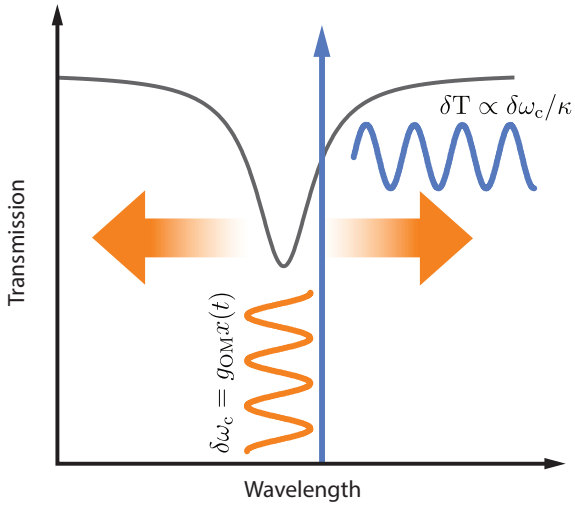

Figure 1.6: **Mechanical Transduction Cartoon.** Schematic diagram of the detection of mechanical motion. An input mechanical displacement, $x(t)$, causes a modulation of the cavity resonance frequency ($\delta\omega_c = g_{OM}x(t)$, orange) which, for laser detuned to the side of the optical resonance (blue arrow), linearly modulates the transmission $\delta T \propto g_{OM}x(t)/\kappa$.

$$T_{det}(t,\Delta) = T_{det}(\Delta) + \frac{dT_{det}}{d\Delta}\frac{d\Delta}{dx(t)} = T_{det}(\Delta) + \frac{dT_{det}}{d\Delta}g_{OM}x(t) \tag{1.27}$$

$$\frac{dT_{det}}{d\Delta} = 2\hbar\omega_\ell|a_{in}|^2\frac{\kappa_{in}(\kappa-\kappa_{in})\Delta}{\left(\left(\frac{\kappa}{2}\right)^2+\Delta^2\right)^2}, \tag{1.28}$$

where, by definition, the mechanical motion causes a change in the detuning of $\Delta_x(t) = g_{OM}x(t)$, and here we have ignored the possibility of the optical field influencing the mechanical motion, which we'll consider in Section 1.2.4. So, the first term is just the DC or steady-state value of the transmission, as plotted in Fig. 1.4, and then it is the second term that contains information about the mechanical motion. This transduction of mechanical motion is shown conceptually in Fig. 1.6. The derivative component $\frac{dT_{det}}{d\Delta}$ is shown in Fig. 1.7 for the same parameters as were used to plot the example reflection lineshape in Fig. 1.4.

We can now use this to calculate the total signal due to $x(t)$:

$$P_m(t) = \frac{dT_{det}}{d\Delta}g_{OM}x(t) \tag{1.29}$$

$$= 2\hbar g_{OM}\omega_\ell|a_{in}|^2\frac{\kappa_{in}(\kappa-\kappa_{in})\Delta}{\left(\left(\frac{\kappa}{2}\right)^2+\Delta^2\right)^2}x(t)\,. \tag{1.30}$$

Typically, for amplitude detection of the laser light (as opposed to phase detection as in Chapter 4), the laser is positioned at $\Delta = \kappa/2$ because here the slope $\frac{dT_{det}}{d\Delta}$ is maximized. So, at this detuning

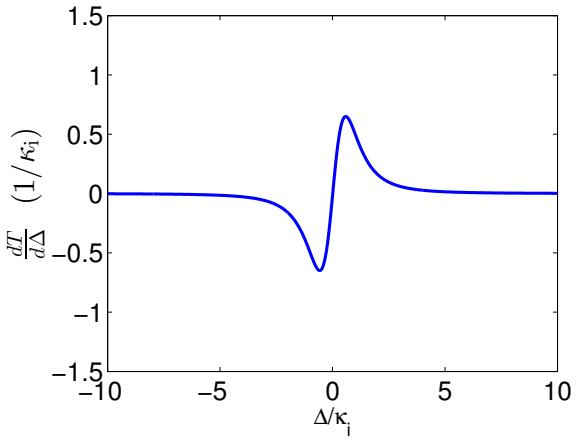

Figure 1.7: **Cavity Transmission Slope.** Plot of the slope of the reflection from a single-sided optical cavity using Eq. (1.28) with $\kappa_{\rm in} = \kappa_{\rm e}, \kappa_{\rm e}/\kappa_{\rm i} = 0.6$. Note the slope and detuning are both in units of the intrinsic mechanical linewidth $\kappa_{\rm i}$

we have

$$P_{\rm m}(t)\,|_{\Delta=\frac{\kappa}{2}} = 4g_{\rm OM}P_{\rm in}\frac{\kappa_{\rm in}\left(\kappa-\kappa_{\rm in}\right)}{\kappa^3}, \tag{1.31}$$

where we used $P_{\rm in} = \hbar\omega_\ell|a_{\rm in}|^2$. This optical power is then measured on a photodetector, which yields a detected voltage proportional to $V_{\rm m} = P_{\rm m}R_{\rm i}T_{\rm ig}$, where the detector responsivity in Amps/Watt is $R_{\rm i}$ and the transimpedence gain of the detector in Volts/Amp is $T_{\rm ig}$. This is usually detected on a spectrum analyzer as electrical power, $P_{\rm e} = V_{\rm m}^2/{\rm R}$, where R is the effective electrical impedance of the detector. Thus, in the spectral domain, our detected signal power is given by

$$\begin{aligned} P_{\rm e}(\omega) &= \left\langle \left(R_{\rm i}T_{\rm ig}\frac{d{\rm T}_{\rm det}}{d\Delta}g_{\rm OM}x(\omega)\right)^2\right\rangle/{\rm R}, \\ &= \frac{\left(R_{\rm i}T_{\rm ig}\frac{d{\rm T}_{\rm det}}{d\Delta}g_{\rm OM}\right)^2}{\rm R}\langle x(\omega)^2\rangle, \\ &= \frac{\left(R_{\rm i}T_{\rm ig}\frac{d{\rm T}_{\rm det}}{d\Delta}g_{\rm OM}\right)^2}{\rm R}S_{\rm xx}(\omega)\,, \end{aligned} \tag{1.32}$$

where in the final expression we have related the expectation value and the spectral density via the relation given in Appendix A.

When directly on resonance ($\Delta = 0$) the derivative vanishes and to first order there is no detection of the mechanical motion. However, the change in the phase of the outgoing light, $\frac{d\phi}{d\Delta}$, undergoes a maximum at this detuning, so one can achieve detection sitting directly on resonance when using a phase-sensitive method, such as homodyning with a second laser beam (see Appendix B).

1.2.4 Radiation Pressure Back-Action

We now consider the effect of the optical radiation pressure on the mechanical element by taking a perturbative approach. We start by taking the ansatz of the mechanical motion as sinusoidal, $x(t) = x_0\epsilon_x \cos\omega_{\rm m}t$, and expanding the optical mode in the small parameter ϵ_x as $a(t) = \sum_n \epsilon_x^n a_n(t)$. The optics interacts with the mechanics via the forcing term on the RHS of Eq. (1.8), where we need to solve for $n_{\rm c}(t) = a^*(t)\,a(t)$. Plugging in our expansion gives

$$n_{\rm c}(t) = a^*(t)a(t) = a_0^2 + \epsilon_x a_1^* a_0 + \epsilon_x a_0^* a_1, \tag{1.33}$$

where we have considered terms up to first-order in ϵ_x. To obtain these terms, we next put our ansatz into the equation of motion for the optical field (Eq. (1.7)), and collecting like powers in ϵ_x yields two equations:

$$\dot{a}_0 = i\left(\Delta^{'} - \frac{\kappa}{2}\right)a_0 + \sqrt{\kappa_{\rm in}}a_{\rm in}, \tag{1.34}$$

$$\dot{a}_1 = i\left(\Delta^{'} - \frac{\kappa}{2}\right)a_1 + ix_1 g_{\rm OM} a_0, \tag{1.35}$$

$$\tag{1.36}$$

where we have defined $\Delta^{'} = \Delta + x_0 g_{\rm OM}$, and $x_1(t) = \cos\omega_{\rm m}t$. By throwing our an-satz for $x(t)$ into our equation of motion, it's simple to show that since x_0 is a constant, $\dot{a}_0 = 0$. This allows us to solve for the steady state component of the optical field as:

$$a_0 = \frac{\sqrt{\kappa_{\rm in}}a_{\rm in}}{\frac{\kappa}{2} - i\Delta^{'}}. \tag{1.37}$$

To solve for the harmonic component of the field, a_1, we compute the Fourier transform:

$$\begin{aligned} i\omega a_1 &= \left(i\Delta^{'} - \frac{\kappa}{2}\right)a_1 + ix_1(\omega)\,g_{\rm OM}a_0, \\ \rightarrow a_1 &= \frac{ix_1(\omega)\,g_{\rm OM}a_0}{i\,(\omega - \Delta^{'}) + \frac{\kappa}{2}}, \qquad a_1^* = -\frac{ix_1(\omega)\,g_{\rm OM}a_0^*}{i\,(\omega + \Delta^{'}) + \frac{\kappa}{2}}. \end{aligned} \tag{1.38}$$

In this result we have used a property of the fourier transform listed in Appendix A, namely, $A^*(\omega) = A(-\omega)$. Also, we didn't write it explicitly, but the fourier transform of the mechanical motion is $x(\omega) = |x|\left(\delta\left(\omega - \omega_m\right) + \delta\left(\omega + \omega_m\right)\right)/2$. Putting these two together, we have

$$(a_1^* a_0 + a_0^* a_1) = i x_1 g_{\rm OM} |a_0|^2 \left(\frac{1}{i\,(\omega - \Delta') + \frac{\kappa}{2}} - \frac{1}{i\,(\omega + \Delta') + \frac{\kappa}{2}} \right), \tag{1.39}$$

$$\begin{aligned} &= \frac{g_{\rm OM}|a_0|^2}{\omega} \left(\frac{\frac{\kappa}{2}}{(\omega - \Delta')^2 + \left(\frac{\kappa}{2}\right)^2} - \frac{\frac{\kappa}{2}}{(\omega + \Delta')^2 + \left(\frac{\kappa}{2}\right)^2} \right) i\omega x_1 \\ &\quad - g_{\rm OM}|a_0|^2 \left(\frac{\Delta' + \omega}{(\omega + \Delta')^2 + \left(\frac{\kappa}{2}\right)^2} + \frac{\Delta' - \omega}{(\omega - \Delta')^2 + \left(\frac{\kappa}{2}\right)^2} \right) x_1. \end{aligned} \tag{1.40}$$

In the final expression we have explicitly separated out the real and imaginary terms because when we Fourier transform back to the time domain, we can use the fact that $\mathcal{F}^{-1}[i\omega x_1] = \dot{x}_1$. Explicitly, after performing the inverse Fourier transform, we have in the time domain

$$\begin{aligned} (a_1^* a_0 + a_0^* a_1) &= \frac{g_{\rm OM}|a_0|^2}{\omega_{\rm m}} \left(\frac{\frac{\kappa}{2}}{(\omega_{\rm m} - \Delta')^2 + \left(\frac{\kappa}{2}\right)^2} - \frac{\frac{\kappa}{2}}{(\omega_{\rm m} + \Delta')^2 + \left(\frac{\kappa}{2}\right)^2} \right) \dot{x}_1(t) \\ &\quad - g_{\rm OM}|a_0|^2 \left(\frac{\Delta' + \omega_{\rm m}}{(\omega_{\rm m} + \Delta')^2 + \left(\frac{\kappa}{2}\right)^2} + \frac{\Delta' - \omega_{\rm m}}{(\omega_{\rm m} - \Delta')^2 + \left(\frac{\kappa}{2}\right)^2} \right) x_1(t)\,, \\ &= g_{\rm OM}|a_0|^2 \left(\frac{\dot{x}_1}{\omega_{\rm m}} \mathrm{A}\left(\Delta'\right) - x_1 \mathrm{B}\left(\Delta'\right) \right), \end{aligned} \tag{1.41}$$

where in the last step we have introduced the simpler notation $\mathrm{A}\left(\Delta'\right)$ and $\mathrm{B}\left(\Delta'\right)$.

Armed with this final result, we can substitute this expression into our x equation of motion,

$$\begin{aligned} \ddot{x} &= -\gamma_{\rm i}\dot{x} - \omega_{\rm m}^2 x + F_{\rm th}/m_{\rm eff} + \frac{\hbar g_{\rm OM}^2 |a_0|^2}{m_{\rm eff}} \left(\frac{\dot{x}}{\omega_{\rm m}} \mathrm{A} - x\mathrm{B} \right), \\ &= -\gamma_{\rm OM}\dot{x} - \omega_{\rm OM}^2 x + F_{\rm th}/m_{\rm eff}, \end{aligned} \tag{1.42}$$

where we have introduced the optomechanically-modified damping rate and mechanical frequency:

$$\begin{aligned} \gamma_{\rm OM} &= \gamma_{\rm i} - \frac{\hbar g_{\rm OM}^2 |a_0|^2}{m_{\rm eff}\omega_{\rm m}} \mathrm{A} \\ &= \gamma_{\rm i} - \frac{\hbar g_{\rm OM}^2 \kappa}{2 m_{\rm eff}\omega_{\rm m}} \frac{\kappa_{\rm in}|a_{\rm in}|^2}{\left(\frac{\kappa}{2}\right)^2 + \Delta'^2} \frac{4\omega_{\rm m}\Delta'}{\left[(\omega_{\rm m} - \Delta')^2 + \left(\frac{\kappa}{2}\right)^2\right]\left[(\omega_{\rm m} + \Delta')^2 + \left(\frac{\kappa}{2}\right)^2\right]}, \end{aligned} \tag{1.43}$$

$$\begin{aligned} \omega_{\rm OM} &= \sqrt{\omega_{\rm m}^2 + \frac{\hbar g_{\rm OM}^2 |a_0|^2}{m_{\rm eff}} \mathrm{B}} \\ &= \sqrt{\omega_{\rm m}^2 + \frac{\hbar g_{\rm OM}^2}{m_{\rm eff}} \frac{\kappa_{\rm in}|a_{\rm in}|^2}{\left(\frac{\kappa}{2}\right)^2 + \Delta'^2} \left(\frac{\omega_{\rm m} + \Delta'}{(\omega_{\rm m} + \Delta')^2 + \left(\frac{\kappa}{2}\right)^2} - \frac{\omega_{\rm m} - \Delta'}{(\omega_{\rm m} - \Delta')^2 + \left(\frac{\kappa}{2}\right)^2} \right)}. \end{aligned} \tag{1.44}$$

Here we have written out the full terms explicitly. We can see that, to first order, the effect of the radiation pressure back-action on the mechanical oscillator is to modify both its damping rate and its oscillation frequency. These terms are quite complicated, but a few general features can be observed. The first is that both modifications are 0 for $\Delta^{'} = 0$, i.e., when the laser is directly on resonance with the optical cavity. Also, the effect switches sign with the sign of $\Delta^{'}$, so detuning the laser to the lower frequency side, $\Delta^{'} < 0$, increases the damping, $\gamma_{\mathrm{OM}} > \gamma_{\mathrm{i}}$, but decreases the frequency, $\omega_{\mathrm{OM}} < \omega_{\mathrm{m}}$. Detuning the laser to higher-frequencies $\Delta^{'} > 0$ has the opposite effect. This simple linearized theory breaks down when the damping or frequency becomes negative $\gamma_{\mathrm{OM}}, \omega_{\mathrm{OM}} < 0$, when the mechanical amplitude, ϵ_x, is too large, or when the steady-state displacement due to the radiation pressure, x_0, is too large. A full description of these effects can be found in Ref. [15].

In the sideband unresolved regime, $\omega_{\mathrm{m}} \ll \kappa$, we can simplify these equations a bit:

$$\begin{aligned}
\gamma_{\mathrm{OM}} &= \gamma_{\mathrm{i}} - \frac{\hbar g_{\mathrm{OM}}^2 \kappa}{m_{\mathrm{eff}}} \frac{\kappa_{\mathrm{in}}|a_{\mathrm{in}}|^2}{\left(\frac{\kappa}{2}\right)^2 + \Delta^{'2}} \frac{2\Delta^{'}}{\left(\Delta^{'2} + \left(\frac{\kappa}{2}\right)^2\right)^2}, \\
&= \gamma_{\mathrm{i}} - \frac{\hbar g_{\mathrm{OM}}^2 \kappa}{m_{\mathrm{eff}}} n_{\mathrm{c}}(\Delta^{'}) \frac{2\Delta^{'}}{\left(\Delta^{'2} + \left(\frac{\kappa}{2}\right)^2\right)^2}, \qquad (1.45) \\
&= \gamma_{\mathrm{i}} \left[1 - \left(\frac{2\kappa/\gamma_{\mathrm{i}}}{\Delta^{'2} + \left(\frac{\kappa}{2}\right)^2}\right)\left(\frac{\hbar g_{\mathrm{OM}}^2}{m_{\mathrm{eff}}} \frac{\Delta^{'} n_{\mathrm{c}}(\Delta^{'})}{\Delta^{'2} + \left(\frac{\kappa}{2}\right)^2}\right)\right], \qquad (1.46)
\end{aligned}$$

$$\begin{aligned}
\omega_{\mathrm{OM}} &= \sqrt{\omega_{\mathrm{m}}^2 + \frac{\hbar g_{\mathrm{OM}}^2}{m_{\mathrm{eff}}} \frac{\kappa_{\mathrm{in}}|a_{\mathrm{in}}|^2}{\left(\frac{\kappa}{2}\right)^2 + \Delta^{'2}} \frac{2\Delta^{'}}{\Delta^{'2} + \left(\frac{\kappa}{2}\right)^2}}, \\
&\approx \omega_{\mathrm{m}} + \frac{\hbar g_{\mathrm{OM}}^2}{m_{\mathrm{eff}} \omega_{\mathrm{m}}} n_{\mathrm{c}}(\Delta^{'}) \frac{\Delta^{'}}{\Delta^{'2} + \left(\frac{\kappa}{2}\right)^2}, \qquad (1.47) \\
&= \omega_{\mathrm{m}} \left[1 + \left(\frac{1}{\omega_{\mathrm{m}}^2}\right)\left(\frac{\hbar g_{\mathrm{OM}}^2}{m_{\mathrm{eff}}} \frac{\Delta^{'} n_{\mathrm{c}}(\Delta^{'})}{\Delta^{'2} + \left(\frac{\kappa}{2}\right)^2}\right)\right], \qquad (1.48)
\end{aligned}$$

where we have used our formula for the intracavity photon number, $n_{\mathrm{c}}(\Delta)$, in Eq. (1.20), and the approximation in the final expression for ω_{OM} holds for small frequency shifts: $|\omega_{\mathrm{OM}} - \omega_{\mathrm{m}}| \ll \omega_{\mathrm{m}}$. Finally, we note that, in principle, the static shift, x_0, must be iteratively solved for in terms of $|a_0|^2$ because the extra detuning changes the static intracavity field and vice-versa. However, in practice, this shift is very small or easily corrected, and so we will ignore it and use $\Delta^{'} \to \Delta$. For some systems, this radiation pressure displacement is non-negligible and yields interesting nonlinear effects [16].

In Fig. 1.8 we have plotted an example of the frequency shift and damping as the laser is swept across the optical cavity, assuming the mechanical element frequency is much less than the optical loss rate of the cavity, i.e., the regime where Eqs. 1.46 and 1.48 are valid. The specific parameters

used (detailed in the figure caption) are very similar to that of the device in the feedback-cooling experiment detailed in Chapter 4.

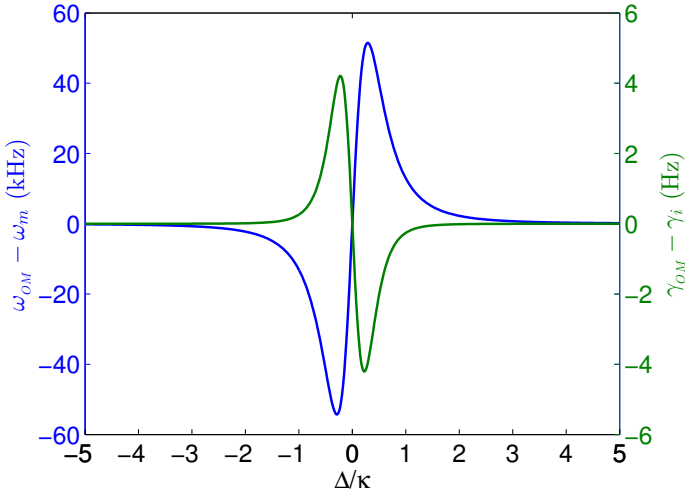

Figure 1.8: **Frequency and Damping; Sideband Unresolved.** Plot of the frequency shift ($\omega_{\rm OM} - \omega_{\rm m}$, blue) and change in the damping rate ($\gamma_{\rm OM} - \gamma_{\rm i}$, green) versus normalized laser detuning in the regime where Eqs. 1.46 & 1.48 are valid: $\omega_{\rm m}/\kappa = 1.2{\times}10^{-5}$. Parameters used: $P_{\rm in} = 150\ \mu$W, $g_{\rm OM}/2\pi = 100$ GHz/nm, $\omega_{\rm m}/2\pi = 1$ MHz, $\kappa/2\pi = 80$ GHz, $\kappa_{\rm in} = \frac{3}{8}\kappa$, $m_{\rm eff} = 90$ femto-kg.

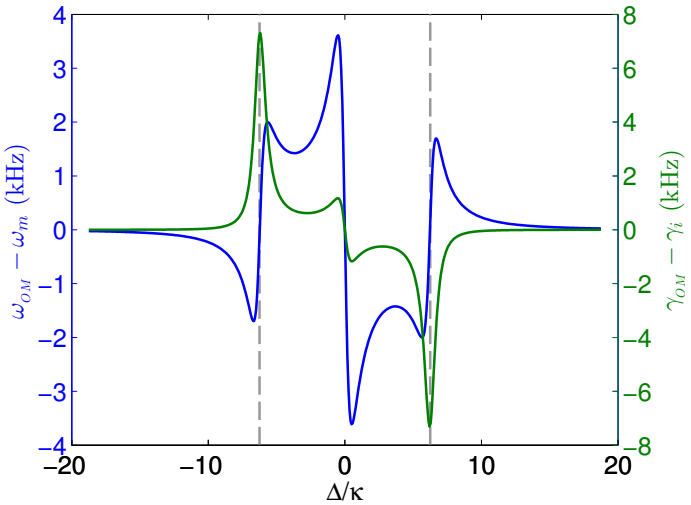

Figure 1.9: **Frequency and Damping; Sideband Resolved.** Plot of the frequency shift ($\omega_{\rm OM} - \omega_{\rm m}$, blue) and change in the damping rate ($\gamma_{\rm OM} - \gamma_{\rm i}$, green) versus normalized laser detuning in the regime where the full form of the optomechanical backaction, Eqs. 1.43 and 1.44, must be used: $\omega_{\rm m}/\kappa = 6.25$. Grey dashed lines indicate a detuning from the optical cavity equal to one mechanical frequency. Parameters used: $P_{\rm in} = 150$ nW, $g_{\rm OM}/2\pi = 100$ GHz/nm, $\omega_{\rm m}/2\pi = 4$ GHz, $\kappa/2\pi = 640$ MHz, $\kappa_{\rm in} = \frac{3}{8}\kappa$, $m_{\rm eff} = 50$ atto-kg.

In Fig. 1.9 we have plotted an example of the frequency shift and damping when the device is in

the sideband resolved regime, i.e., $\omega_{\rm m}/\kappa = 6.25$. The specific parameters used (detailed in the figure caption) are similar to that of the device used in the nonlinear multistability experiment detailed in Chapter 5. It can be seen immediately that this regime can lead to more complicated interactions between the mechanical element and optical field. The additional peaked regions on either side of the optical resonance occur at precisely $\Delta = \pm\omega_{\rm m}$. This regime will be discussed in more detail in Section 1.3.

1.3 Sideband Resolved Optomechanics

This section introduces the optomechanical equations in a method more suitable for tackling high-frequency systems, and going beyond the linear approximation used in Section 1.2. The mechanical modulation of the laser light generates two sidebands at frequencies $(\omega_\ell - \omega_{\rm m})$ and $(\omega_\ell + \omega_{\rm m})$. The regime where $\omega_{\rm m} \gg \kappa$ is known as sideband 'resolved' because, since optical linewidth is narrower than the frequency spread in these two sidebands, the optical cavity can be used to filter out just one of the sidebands, as shown in Fig. 1.10. This regime is very useful for quantum physics experiments, where one of the sidebands is useful, but the unwanted second sideband (if not filtered by the optical cavity) adds additional noise to the system. This additional noise can act to obscure any quantumness. This filtering property was necessary in two of the experiments I worked on: to cool a resonator to its quantum ground-state [11], and to observe the quantum nature of the mechanical resonator [17]. This thesis will not cover these quantum aspects in detail, but for an authoritative review of these experiments and this regime, see the thesis of Dr. Amir Safavi-Naeini [18] and Dr. Jeff Hill [2], as well as these reviews from the literature [15, 19, 20].

A second interesting feature of the sideband-resolved regime is that these distinct sidebands lead to very interesting behavior when the mechanical amplitude is large enough that the linear approximation used earlier no longer holds. The theory for this situation is presented here, and our experiment in this regime is discussed in Chapter 5. The starting point for the analysis is, of course, the equations of motion for the system [15]:

$$\ddot{x}(t) = -\gamma_{\rm i}\dot{x}(t) - \omega_{\rm m}^2 x(t) + 2\omega_{\rm m} g_0 x_{\rm zp}|a(t)|^2, \tag{1.49}$$

$$\dot{a}(t) = \left[-\frac{\kappa}{2} + i\left(\Delta + \frac{g_0}{x_{\rm zp}}x(t)\right)\right] a(t) + \sqrt{\kappa_{\rm in}}a_{\rm in}, \tag{1.50}$$

where we have defined $g_0 = g_{\rm OM}x_{\rm zp}$, with the quantum zero-point fluctuation amplitude being given by $x_{\rm zp} = \sqrt{\frac{\hbar}{2m_{\rm eff}\omega_{\rm m}}}$. Following the derivation given in Ref. [21], we again start by assuming that the motion is sinusoidal, $x(t) = {\rm A}\sin\omega_{\rm m}t$, and we seek to find the homogenous, a_h, and then the particular, a_p, form of the solution to the differential equation for the optical field, where our final

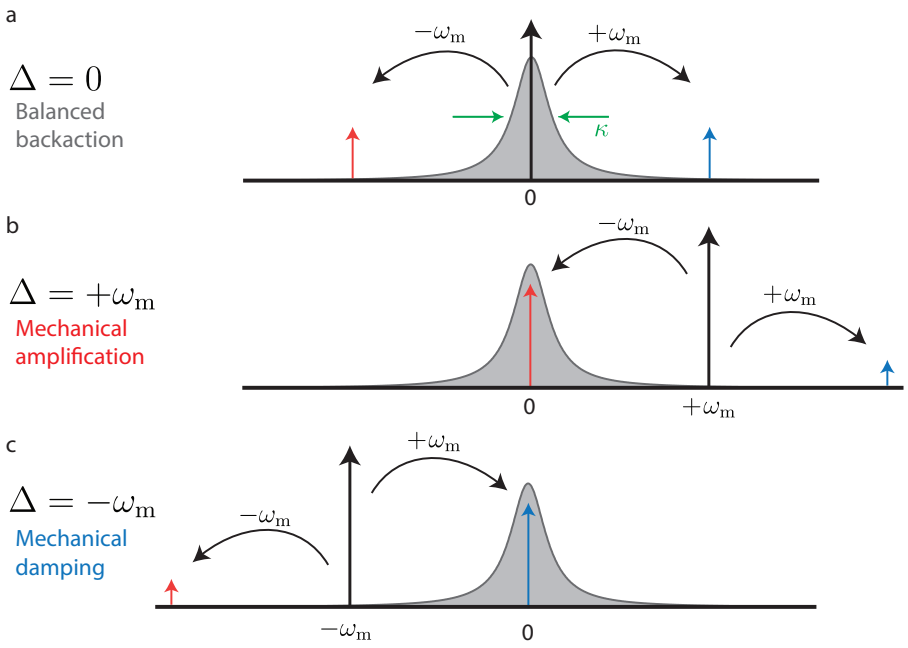

Figure 1.10: **Sideband Resolved System.** (a) With the laser (thick black arrow) sitting directly on resonance with the optical cavity (grey) at $\Delta = 0$, there are two optical sidebands generated by the mechanical motion that show up at $\Delta = \pm\omega_{\rm m}$. The lower (higher) frequency sideband is denoted with a red (blue) arrow. With the laser directly on resonance there is (to first order) no back-action of the laser onto the mechanical mode, because the red and blue sidebands are of equal magnitude and offset each other. (b) With the laser 'blue-detuned' at $\Delta = +\omega_{\rm m}$, the lower-frequency red sideband is significantly enhanced because it overlaps with the response of the optical cavity. The higher-frequency blue sideband is suppressed because it is far off-resonance with the optical mode. It can be seen that photons in the red optical sideband have less energy than the incoming photons, and thus from energy conservation they have transferred energy into the mechanical resonator. Thus, since this is the dominant sideband, the mechanical amplitude is amplified. (c) With the laser 'red-detuned' at $\Delta = -\omega_{\rm m}$, the higher-frequency blue sideband is significantly enhanced because it overlaps with the response of the optical cavity, and similarly the lower-frequency red sideband is suppressed. Now, since photons in the blue optical sideband have more energy than the incoming photons the laser tends to extract energy from the mechanical resonator. This damps and cools the mechanical mode.

solution will be of the form $a(t) = a_p(t) + a_h(t)$. First, the homogenous solution is easily found:

$$\begin{aligned} \dot{a}_h(t) &= \left[-\frac{\kappa}{2} + i\left(\Delta + \frac{g_0}{x_{\rm zp}}{\rm A}\sin\omega_{\rm m}t\right)\right] a_h(t)\,, \\ \rightarrow\ a_h &= {\rm C}_0 e^{\left(-\frac{\kappa}{2}+i\Delta\right)t - i\frac{g_0{\rm A}}{x_{\rm zp}\omega_{\rm m}}\cos\omega_{\rm m}t}. \end{aligned} \tag{1.51}$$

Note that in integrating to obtain Eq. (1.51) we have taken care to integrate the mechanical motion component as well. We can see that without the laser driving term, the particular solution is damped exponentially at rate $\kappa/2$, and thus the solution converges to $a(t) = a_p(t)$. So, now we find

the particular solution by noting that it can take the form $a_p = C(t)\, a_h(t)$, where,

$$\dot{C}(t) = \frac{1}{a_h(t)}\sqrt{\kappa_{\rm in}}a_{\rm in} = \frac{\sqrt{\kappa_{\rm in}}a_{\rm in}}{\rm C_0}e^{\left(\frac{\kappa}{2}-i\Delta\right)t+i\frac{g_0 \rm A}{x_{\rm zp}\omega_{\rm m}}\cos\omega_{\rm m}t}. \tag{1.52}$$

This differential equation can be directly integrated if we use the Jacobi-Anger expansion,

$$e^{i\beta\cos\theta} = \sum_{\rm n=-\infty}^{\infty} i^{\rm n} J_{\rm n}(\beta)\, e^{i{\rm n}\theta}, \tag{1.53}$$

where $J_{\rm n}$ is the Bessel function of the first kind, n-th order, and β is known as the modulation index.

Making this substitution and integrating gives for C,

$$C(t) = \sqrt{\kappa_{\rm in}}a_{\rm in}e^{\left(\frac{\kappa}{2}-i\Delta\right)t}\sum_{\rm n}\frac{i^{\rm n}J_{\rm n}(\beta_{\rm m})}{\frac{\kappa}{2}+i\left({\rm n}\omega_{\rm m}-\Delta\right)}e^{i{\rm n}\omega_{\rm m}t}, \tag{1.54}$$

where we have identified the unitless optomechanical modulation index, $\beta_{\rm m} = {\rm A}\frac{g_0}{x_{\rm zp}\omega_{\rm m}}$. Finally, we obtain the steady-state solution for our optical field:

$$\begin{aligned} a(t) = a_p(t) &= C(t)\, a_h(t) \\ &= \sqrt{\kappa_{\rm in}}a_{\rm in}e^{-i\beta_{\rm m}\cos\omega_{\rm m}t}\sum_{\rm n}\frac{i^{\rm n}J_{\rm n}(\beta_{\rm m})}{\frac{\kappa}{2}+i\left({\rm n}\omega_{\rm m}-\Delta\right)}e^{i{\rm n}\omega_{\rm m}t}. \end{aligned} \tag{1.55}$$

Here, each of the n terms in the sum is a mechanical sideband of the optical field oscillating at frequency $\rm n\omega_m$. For relatively small mechanical amplitudes this system can be linearized to obtain simpler expressions for the field because the Bessel functions have the property that $J_0(\beta_{\rm m}\ll 1)\approx 1$, $J_{n\neq 0}(\beta_{\rm m}\ll 1)\propto \beta_{\rm m}^{|{\rm n}|}$. However, in the large-modulation regime, $\beta_{\rm m}\gtrsim 1$, the relative amplitudes of the Bessel functions have a non-trivial dependence on $\beta_{\rm m}$. For practical calculations, a good rule of thumb is to sum over at least ${\rm n} = \pm 2\beta_{\rm m}$. The presence of so many interacting sidebands means that the system is highly nonlinear in this regime, and the dynamics can be very complicated. It is this nonlinearity that many quantum experiments seek to exploit [22]. However, this is difficult because it requires the system to be both sideband resolved, and nonlinear at the ground-state amplitude (${\rm A} = x_{\rm zp}$). Thus, it requires that $\beta_{\rm m} = g_0/\omega_{\rm m}\gtrsim 1$, which has not yet been achieved in an optomechanical system. We will focus on the classical effects of these multiple sidebands on the mechanical oscillator and the optical transmission in the experiment presented in Chapter 5.

Chapter 2

Design and Fabrication of Optomechanical Devices

In this chapter we will discuss the full life-cycle of making an optomechanical device. First we will focus in detail on the process for the stoichiometric silicon nitride (Si_3N_4) devices used in Chapter 3 and 4. Then we will briefly discuss the (similar) design and fabrication process for the optomechanical crystals used in Chapter 5. The primary design consideration for both of these systems is to simultaneously maximize the coupling, g_{OM}, while maintaining large optical and mechanical quality factors. However, the differences in the material and in the desired mechanical frequency lead to differences in the designs and methods.

2.1 Device Design: Silicon Nitride Beam Resonators

Material	Si_3N_4 (LPCVD)		
Structure	Glass	Tensile Stress	900 MPa
Layer Thickness	420 nm	Index (@ 1550nm)	2
Density	3100 kg/m^3	Electrical Resistivity	>10^{14} Ω-m
Young's Modulus	290 GPa	Thermal Conductivity	30 W/m/K
Hardness	35 GPa	Specific Heat	0.7 J/g/K

Table 2.1: **Si_3N_4 Properties.**

In our research group we tend to try to answer the question of what can be achieved using

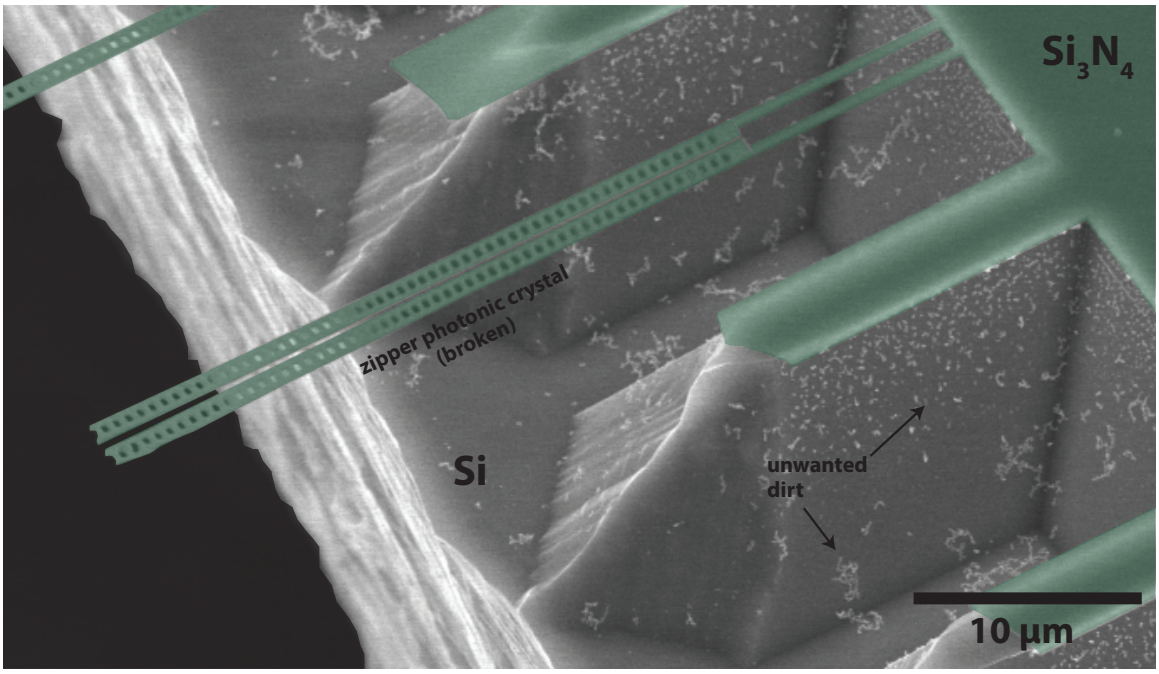

Figure 2.1: **Cleaved Optomechanical Device.** (a) False-color SEM image where a Si_3N_4 photonic crystal consisting of two 1D photonic crystal cavities side-by-side (a 'zipper' cavity) supported on thin tethers is shown in green with the undercut and cleaved silicon sitting below.

widely-available and standard fabrication methods by employing smart design and engineering. As such, we use commercially grown material silicon nitride in many of our investigations. This material is used as an advanced ceramic because of its strength and high-heat handling capability in many industrial applications [23] such as bearings [24], cutting tools [25], and rocket nozzles [26]. Its stability, low-friction, and bio-compatibility even allow it to be used for joint-replacements [27, 28]. However, for its use as an optomechanical resonator we care primarily that it has high optical index ($n = 2$ @ 1550 nm), low optical loss [29], and large mechanical $Q_{\rm m}$ at room temperature [30, 31]. In Table 2.1 we have collected some of the relevant properties of this material.

The silicon nitride that we use is stoichiometric, Si_3N_4, and consists of a thin-layer, $t_{SiN} = 420$ nm, deposited by a process known as low-pressure chemical vapor deposition (LPCVD) onto a much thicker silicon handle wafer, $t_{Si} = 0.5$ mm, as shown schematically (but not to scale) in the first panel of Fig. 2.9. This method of fabricating Si_3N_4 makes a glassy material with a large electronic band-gap, ≈ 5 eV which means that the material is transparent and low-loss over a wide wavelength span from visible to telecom frequencies. This deposition technique is also important because it leaves the film with an extremely large in-plane tensile (pulling) stress [32] of $\sigma = 0.8 - 1$ GPa, which, as we will discuss, is a critical component of the good mechanical quality factor of resonators made from this material. Finally, it's useful that it is deposited onto Silicon because this material is readily available, and easy to selectively etch away to release our structures (as in Fig. 2.9), allowing

them to freely move. Fig. 2.1 shows a false-color scanning electron microscope (SEM) image of a finished device that has been cleaved in half and shows two side-by-side Si_3N_4 photonic crystals supported on thin tethers (green overlay) extending off the broken edge of the silicon chip. In the following sections we will discuss the design of such devices.

2.1.1 Si_3N_4 Optics

In contrast to the cartoon sketched in Fig. 1.1 we do not trap light using standard bulk mirrors, but rather confine it using engineered 1D photonic crystals. This allows us to trap light on-chip while still allowing for devices with good optical quality, $Q_o = \omega_o/\kappa_i$. These structures rely on periodic patterning of the dielectric constant to create band-gaps for light similar to those for electrons traveling in an atomic crystal lattice. Our method of fabrication only allows for drilling straight air-holes through our thin layer of material and thus the periodic patterning consists of regions of $n_{air} = 1$ and $n_{SiN} = 2$. In Fig. 2.2a we show a top-view SEM of one such photonic crystal, and below it is the same photonic crystal with the simulated energy density of the first-order optical mode that it confines.

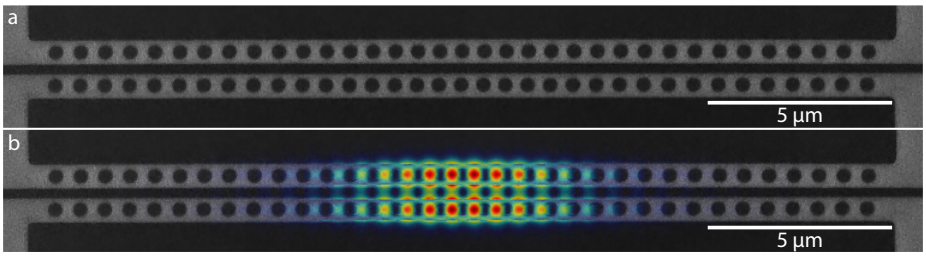

Figure 2.2: **'Zipper' Photonic Crystal.** (a) SEM image of Si_3N_4 photonic crystal consisting of two 1D cavities side-by-side (a 'zipper' cavity) as used in Chapter 3. (b) Same image as (a) with the simulated energy density of the first-order optical mode overlaid where red corresponds to the highest energy density and blue to the lowest. Because of the high concentration of energy in the slot between the beams, the resonance frequency is strongly modified by motion of the gap between the beams.

The method of trapping light in these structures can be understood by first considering an infinite beam that has been periodically patterned with holes, as in the inset of Fig. 2.3a. In Fig. 2.3a we show the bandstructure for this simple 1D crystal and note that at the band-edge there is a range of wavelengths that cannot propagate in the structure. Thus, this pattern has a bandgap (BG) for light. By placing two such crystals next to each other (Fig. 2.3b) it is possible to get a similar (but typically smaller) bandgap between bands that have a different symmetry about the axis of the beams (for a full discussion of optical symmetries see [33]). We are interested in the 'bonded' symmetry where the field is maximized in the gap, as in Fig. 2.3(iii), because the strong localization of field within the gap means that the optical frequency of this band is more strongly modified by

relative motion of the beams than for the band in (iv). We will go into the method of calculating this coupling in more detail in Section 2.1.3.

Finally, armed with this zipper crystal, we make a localized optical resonance by perturbing the lattice constant of the crystal in a central region. This change of the crystal parameters modifies the frequency (wavelength) of light at the band-edge in this region such that it is different from the surrounding unchanged crystal. If done correctly, the new wavelength lies inside the bandgap of the outside periodic crystal and thus light in this region cannot propagate in the rest of the beam. It is thus trapped between the ends, which act effectively as mirrors. The first few such trapped optical modes of the fully-designed structure are shown in Fig. 2.3c.

Conceptually, this is the full process by which we design/imagineer our photonic crystals, but in practice there are many parameters to vary that can effect the mode profile, optical quality factor, and feasibility of fabrication. This is why we employ the COMSOL multiphysics simulation environment to numerically solve for the resonant mode profiles and test out our photonic crystal designs. It is from these simulations that we have obtained the fields shown in Fig. 2.2b and Fig. 2.3c. We refer the reader to these theses from other members of Oskar Painter's group as a reference for performing such simulations: [34, 35]. After discussing the motivationg for the design of our mechanical elements in Section 2.1.2 we will discuss how these simulated optical fields are used to estimate the optomechnical coupling, g_{OM}, and briefly discuss the design of one particular photonic crystal that was used in the feedback cooling experiment presented in Chapter 4.

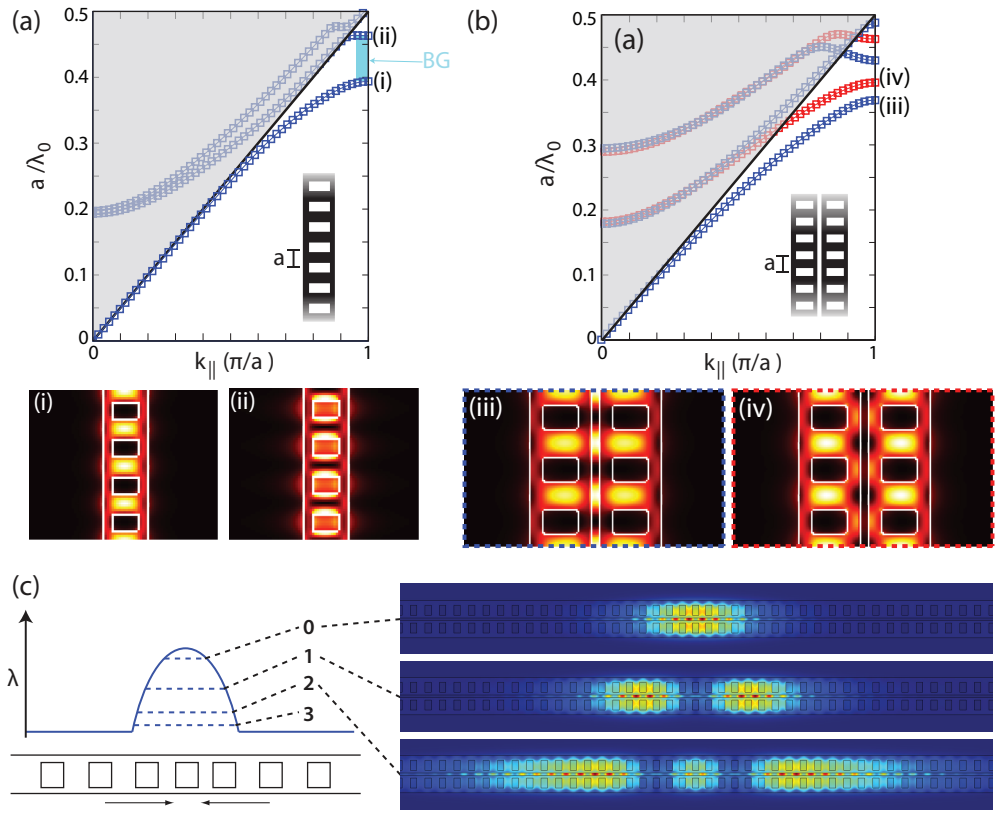

Figure 2.3: **Photonic Crystals 101.** This figure is adapted from the wonderful thesis of Dr. Matt Eichenfield [34]. (a) Band structure for the 1D photonic crystal with rectangular holes as shown in the inset, where black indicates silicon nitride and white indicates air holes. The band structure is plotted for a given wavevector of light along the direction of the lattice, $k_{||}$, in units of π/a, where, a, is the periodicity of the lattice and a/λ_0 is the normalized frequency of the the allowed optical modes at each wavevector. The light cone is denoted by the shaded grey region, which is the area where light can freely radiate away. Optical modes in this region are not well-confined to the photonic crystal because in this region there exist an infinite number of free-space modes it can propagate into. As denoted by the teal region, there is a band-gap (BG) region where light at this k-vector and frequency cannot propagate within the structure. The two images below, (i) and (ii), show the simulated optical energy density for the correspondingly-labeled bands in the plot above where the outline of the photonic crystal is shown in white. (b) Band structure diagram for two 1D photonic crystals separated by a small slot-gap, as shown in the inset, known as a 'zipper' photonic crystal. Here the bands are colored with respect to their symmetry along the axis between the two beams. (iii) The blue bands correspond to the electric field maximized in the center of the slot-gap, which is known as the bonded symmetry. (iv) The red bands correspond to the higher-energy optical mode solution where there is a zero-crossing of the field at the center of the gap, which is known as the anti-bonded symmetry. (c) An optical cavity to trap light is formed by slightly modifying the lattice constant in some central region of the crystal. If this change in the lattice constant is sufficiently smooth, it smoothly changes the wavelength λ of the bonded optical mode from its original value (solid blue line). This generates a potential well for light in this region and so there exist discrete optical mode solutions at different wavelengths (dashed blue lines). At the bottom of this potential well (shortest wavelength) is the 0th order optical mode. A simulation of the energy density mode-profile is shown to the right. Similarly, we show the mode-profiles of the 1st and 2nd order optical modes. Modification of the central region could also consist of changing the hole size and shape as well.

2.1.2 Si_3N_4 Mechanics

Stress: the pain and the promise

As indicated by the title of this section, the large in-plane stress of silicon nitride can be both useful and frustrating. A tensile stress of 0.8 GPa means that the thin film is being isotropically pulled in the X-Y plane as if it were a drum-head pulled taught across the silicon below. This corresponds to an in-plane pressure of $\approx$8,000 atmospheres on the material! Therefore it is not too surprising that at an only slightly higher stress of $\approx$ 5-8 GPa, the material begins to spontaneously crack and facture. If one is not careful, certain designs or fabrication methods can cause the stress to locally exceed this fracture threshold. In Fig. 2.4 we show a small gallery of such stressful failures.

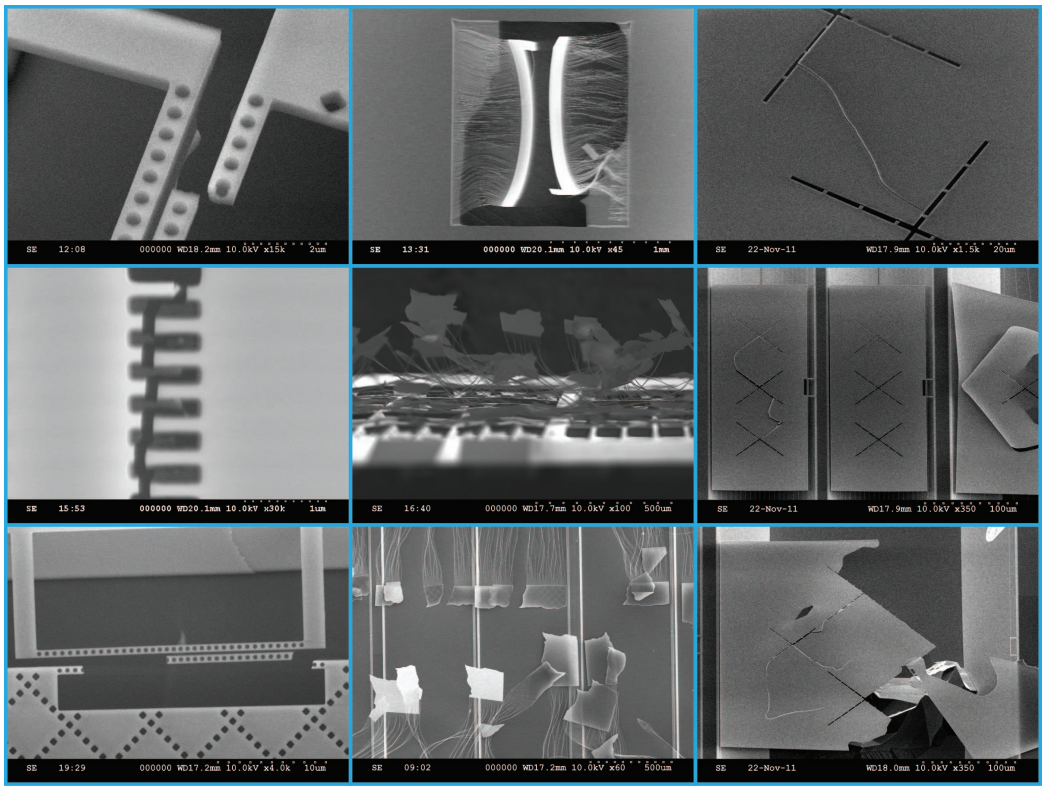

Figure 2.4: **Stress-Fractured Silicon Nitride Devices.** Various SEM images of devices broken and cracked by poorly-managed stress in Si_3N_4.

We can start to understand the mechanics of Si_3N_4 by considering the Euler equation for the frequency of a double-clamped rectangular beam:

$$f_{\mathrm{m}} = \frac{\pi}{2L^2}\sqrt{\frac{EI}{\rho A}}\sqrt{1+\frac{\sigma A L^2}{EI\pi^2}}, \tag{2.1}$$

where L is the beam length, E is the Young's modulus, I is the beam's moment of inertia about the direction of motion, ρ is the material's density, A is the beam's cross-sectional area, and σ is the

tensile (positive) or compressive (negative) stress. However, instead of dwelling on the details, we'll first consider the final term underneath the square root. For a rectangular beam made out of our thin nitride layer (420 nm × 420 nm) and using the parameters in Table 2.1, we find

$$\frac{\sigma A L^2}{EI\pi^2} = 4.6\times10^9 L^2, \tag{2.2}$$

which means that for $L > 15$ μm this term is greater than 1. Since the typical beam lengths we'll be considering for our devices are $L > 50$ μm, we can consider this term to be always $\gg 1$. Dropping the 1+ in Eq. (2.1) allows us to simplify the formula as

$$f_{\mathrm{m}} = \frac{1}{2L}\sqrt{\frac{\sigma}{\rho}}, \tag{2.3}$$

which can be recognized as the equation for the frequency of a string. Thus, our stress-dominated beams can be thought of simply as taught vibrating strings. The fact that this simplification is valid indicates that the beam's stiffness, k, is dominated by the stress, and thus that the energy of the beam's motion, $\propto \frac{1}{2}\mathrm{k}(\Delta x)^2$, is also dominated by the stress.

An example of the simple first-order motions of such string-like beams is shown in Fig. 2.5. It is the in-plane differential motion between the two beams presented in Fig. 2.5b that has the highest g_{OM} and is thus the one of most interest. The thicker section in the center of these beams is where the photonic crystal would be placed. For clarity, the tethers shown here are only ≈ 20 μm, which is shorter than typically used. The small pinning tether between the two beams near their connection to the frame couples the motion of the two beams. Without it, the beams resonate independently instead of being composed of common and differential pairs.

One of the first explanations of the improvements this stress has on the mechanical quality factor of such a beam was laid out in the wonderfully-titled paper "Stress and Silicon Nitride: A Crack in the Universal Dissipation of Glasses" [30]. In this work, they showed that despite being a glass, the presence of stress caused the quality factor to be nearly 3 orders of magnitude larger than un-stressed Si_3N_4. This was in contrast to previous experimental and theoretical work showing that glasses exhibit near-universal (large) mechanical losses [36, 37]. There is still debate in the literature about the precise microscopic mechanism that limits the quality-factors in these stressed materials [38–41], but there is now wide agreement that the stress is the origin of the improvement [31, 42].

This stress-enhancement can be analytically modeled by considering that the material has two different quality factors. One is the quality factor corresponding to energy lost due to the beam undergoing bending, Q_{bend}, and the other is that due to the string undergoing elongation which is related to the stress, Q_σ. Empirically, $Q_{\mathrm{bend}} \ll Q_\sigma$, which means that the loss due to Q_σ is

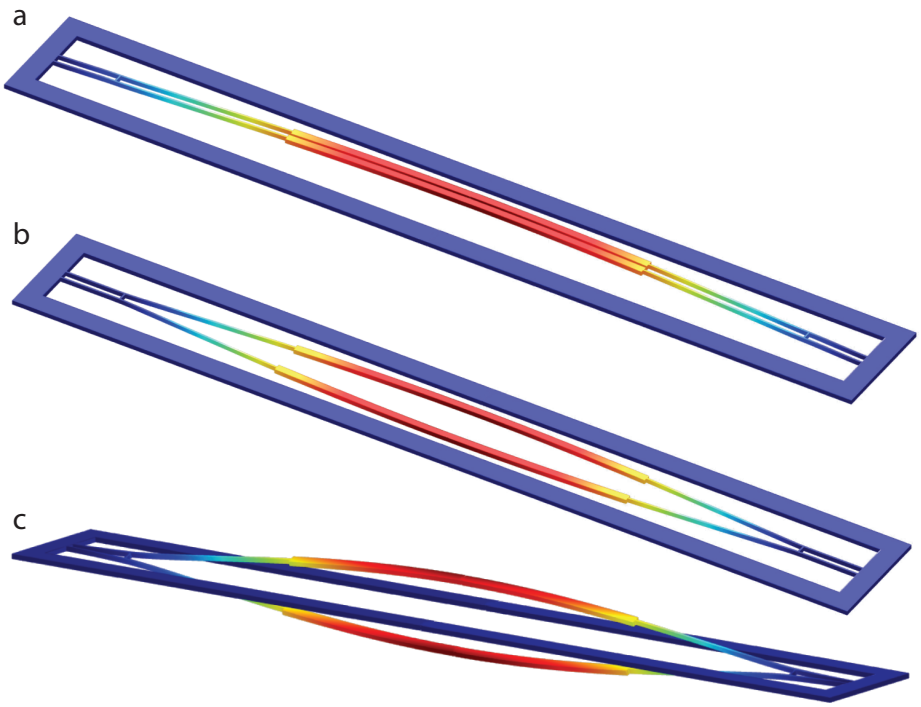

Figure 2.5: **Example Beam Motion.** (a) Fundamental in-plane common motion of two beams. (b) Fundamental in-plane differential motion. (c) Fundamental out-of-plane differential motion. This is the structure used in the experiment presented in Chapter 4.

negligible and so the effective quality factor of a beam is $Q_{\mathrm{m}} = \frac{E_{\mathrm{bend}}}{E_\sigma} Q_{\mathrm{bend}}$, where E_{bend} is the bending energy and E_σ is the stress (or flexural) energy of the beam. For a rectangular beam these quantities can be calculated analytically and explicitly give [42]:

$$Q_{\mathrm{m}} = \left[\frac{(\mathrm{n}\pi)^2}{12} \frac{E}{\sigma} \left(\frac{w}{L}\right)^2 + \sqrt{\frac{E}{\sigma}} \frac{w}{L} \right]^{-1} Q_{\mathrm{bend}} \tag{2.4}$$

$$\approx \sqrt{\frac{\sigma}{E}} \frac{L}{w} Q_{\mathrm{bend}}, \tag{2.5}$$

where w is the beam width and n indicates the n-th harmonic mode of the beam. However, for a Si_3N_4 string of width, $w = 450$ nm, the approximation made in the final step is valid for $L \gg 6\mu\mathrm{m} \times \mathrm{n}^2$. Which will always be satisfied since we will only be considering the fundamental string mode, $\mathrm{n} = 1$, of very long strings, $L > 50$ μm. Measuring several such beams, we have observed this very simple relation of the Q_{m} varying linearly with the length (Fig. 2.6). However, since there is not currently a good microscopic theory for the origin (and thus magnitude) of Q_{bend}, this must be determined empirically (and may vary depending on material quality and growth). In our experiments we find that $Q_{\mathrm{bend}} \approx 14,000$ in reasonable agreement with the $Q_{\mathrm{bend}} = 17,000$ reported in Ref. [42].

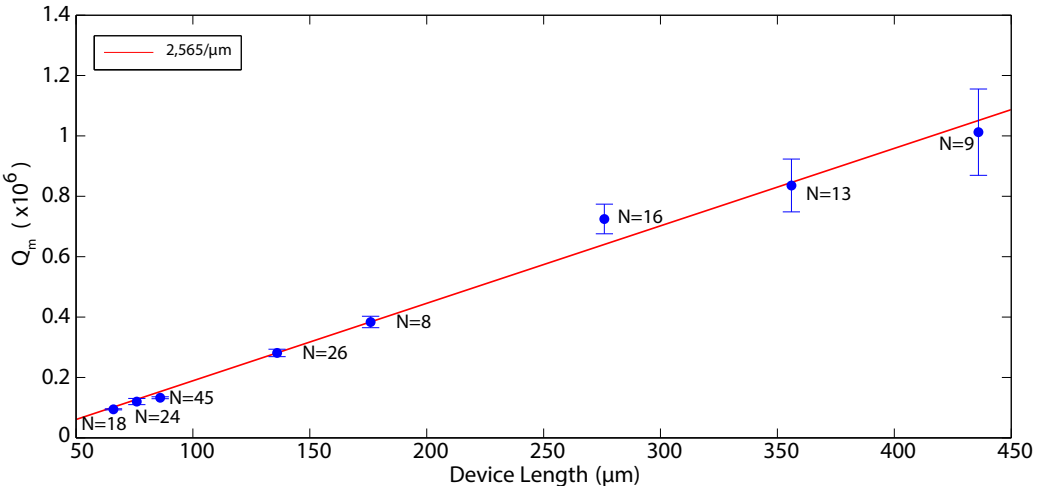

Figure 2.6: **Mechanical Q vs. Device Length.** Plot of the average measured mechanical quality factor versus total device length for devices consisting of 36 μm long photonic crystals supported on either side by 200 nm wide tethers of varying length similar to those shown in Fig. 2.7 (blue dots). The numbers next to each point show how many devices were measured at each length and error bars show the standard deviation of the Q_{m} measurement. The best fit linear slope is $Q_{\mathrm{m}} \propto 2,565/\mu\mathrm{m}$ (red curve).

Thus, guided by this insight, all of the photonic crystal structures we fabricate are suspended on long, thin strings, as shown in Fig. 2.7. As can be seen in Fig. 2.7c-d, the extreme aspect ratios of these devices make it difficult to image them in a single field of view.

2.1.3 Si_3N_4 Optomechanical Coupling – g_{OM}

In silicon nitride devices, the primary coupling between the beam motion (Fig. 2.5) is due to the index contrast between moving Si_3N_4 and air. For small displacements of the beams, perturbation theory can be used to calculate the exact optical frequency shift that a given vector displacement field ($\boldsymbol{Q}(\boldsymbol{r})$) will have on a given optical field ($\boldsymbol{E}(\boldsymbol{r})$) [43]. It essentially amounts to calculating the change in the stored energy of the optical resonance mode due to forcing components of the optical field that lie at the interface of the moving material to be moved into or out of the beam. This is called the moving boundary contribution to the coupling, $g_{\mathrm{OM,MB}}$. It can be calculated explictly with this formula that looks intimidating, but is easily implemented in COMSOL for simulation of our coupling rates [18, 43, 44]:

$$g_{\mathrm{OM,MB}} = -\frac{\omega_{\mathrm{c}}}{2}\frac{\int (\boldsymbol{Q}(\boldsymbol{r})\cdot\boldsymbol{n})\,(\Delta\epsilon|\boldsymbol{E}_{||}|^2 - \Delta(\epsilon^{-1})|\boldsymbol{D}_{\perp}|^2)\mathrm{d}A}{\max(\boldsymbol{Q})\int \epsilon(\boldsymbol{r})\,|\boldsymbol{E}(\boldsymbol{r})|^2\mathrm{d}^3\boldsymbol{r}}, \tag{2.6}$$

where the index contrast at the boundary is given by $\Delta\epsilon = \epsilon_{\mathrm{Si_3N_4}} - \epsilon_{\mathrm{air}}$, and similarly $\Delta(\epsilon^{-1}) = \epsilon^{-1}_{\mathrm{Si_3N_4}} - \epsilon^{-1}_{\mathrm{air}}$,

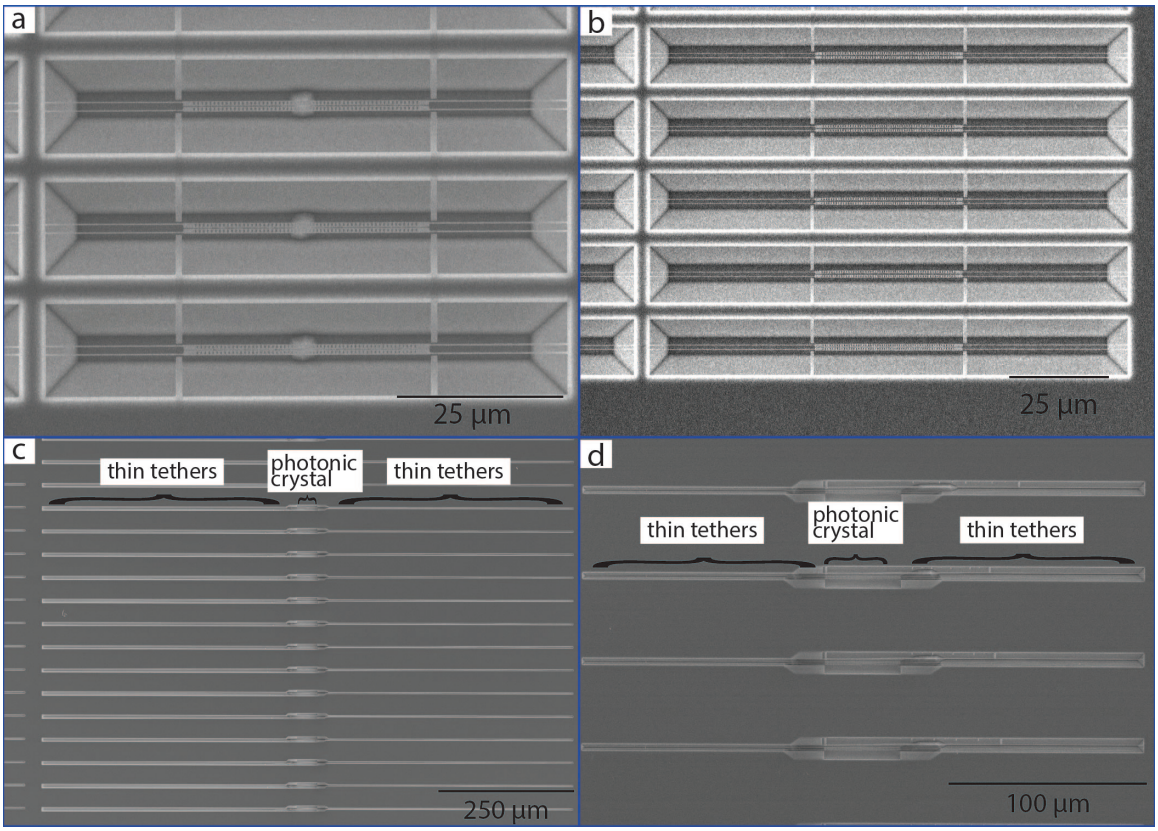

Figure 2.7: **Tethered Photonic Crystals.** (a) Photonic crystals suspended on 20 μm tethers of width $\approx$ 150 nm. (b) Photonic crystals suspended on 40 μm tethers of width $\approx$ 150 nm. (c) Photonic crystals suspended on 500 μm tethers of width $\approx$ 150 nm. (d) Photonic crystals suspended on 120 μm tethers of width $\approx$ 150 nm.

$\boldsymbol{n}$ is the surface normal vector of unit length, the electric displacement vector is given by $\boldsymbol{D}$, and the $||$ and $\perp$ marks indicate values that are parallel or perpendicular to the boundary surface, respectively. The integral in the numerator is over the surface area of all the the moving boundaries and represents the energy change in the field due to the motion, and the denominator values provide the suitable normalizations.

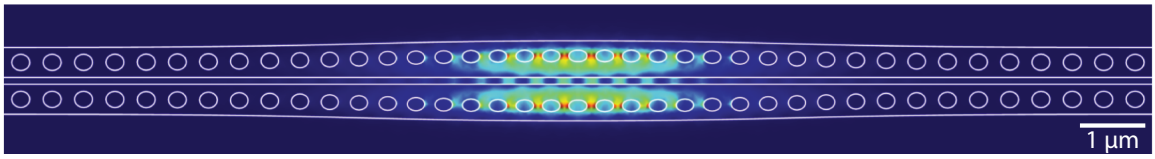

Figure 2.8: **Zipper Mark II Design.** The optical energy density for the first-order bonded optical mode of the designed photonic crystal where the regions of high (low) field are indicated by red (blue). The outline of the Si_3N_4 material is shown in white. The calculated g_{OM} for this device is $g_{\text{OM}}/2\pi = 64$ GHz/nm for a gap of 100 nm between the two beams.

For the systems considered here where the mechanical displacement profile, $\boldsymbol{Q}$, has variation

over a scale much larger than the ≈ 5 μm extent of the confined optical mode, it's typically a good approximation to replace the full vector form of $\boldsymbol{Q}$ with a suitable unit-vector norm displacement such as $\boldsymbol{Q} = \mathbf{1}\hat{x}$. This approximation amounts to saying that every boundary is moving in the same direction and by the same amount. This allows us to estimate the g_{OM} of a designed optical cavity without also explicitly simulating the mechanical displacement vector in COMSOL. This approximation is accurate to the percent level for the very-long fundamental mechanical modes of the beams shown in Fig. 2.7c-d. This is not valid for calculating the coupling of smaller localized mechanical modes such as those discussed in Section 2.3.2, where the full COMSOL simulated solution, $\boldsymbol{Q}$, must be used.

To give an insight into the methods for maximizing this coupling, we will discuss briefly the motivations and method behind our design of the photonic crystal used in the feedback cooling experiment of Section 4. Previous designs for the photonic crystals had required that the two photonic crystal beams that compose the zipper be identical, and that the holes lie always in the center of each respective beam. We sought to determine if the g_{OM} could be enhanced by allowing the beams to have more complicated hole placement profiles. As such, we modified the algorithmic optimization code developed in the group by Jasper Chan [35] to design a new zipper cavity. The algorithm uses Matlab's native nonlinear maximization functions to evaluate different photonic crystal designs and determine which is the best according to the fit function $F = g_{\mathrm{OM}}^2 \cdot \min\left(Q_{\mathrm{o}}, 2\times 10^6\right)$. This fit function was chosen because the goal is to maximize the coupling strength, but to guarantee that the optical Q is maintained in the process. We applied a ceiling of $Q_{\mathrm{o}} = 2\times 10^6$ on the optical quality factor, because this is larger than the highest ever achieved in our Si_3N_4 photonic crystal devices, $\max(Q_{o,\mathrm{Si_3N_4}}) \approx 0.3\times 10^6$. If the optical quality component of the fit function is allowed to be un-bounded, the algorithm tends to get stuck finding solutions with only moderate g_{OM}, but unreasonably large optical quality of $Q_{\mathrm{o}} \approx 50\times 10^6$.

Employing this code, we found that more optical field could be concentrated toward the center of the beams by displacing the holes towards the outer edge and by making the holes more elliptical along the axis of the beams. Intuitively this makes sense because the optical field has lower energy when it lies inside the dielectric material, and higher energy when it is forced into the air. Thus, the optical field 'likes' to live inside the beam to minimize its total energy cost, and thus it tends to avoid the holes. So, as the holes move outward, the field moves inward to escape. The final designed photonic crystal and the simulated optical field for a gap of 100 nm between the two beams is shown in Fig. 2.8 and has a simulated $g_{\mathrm{OM}}/2\pi = 64$ GHz/nm, which is larger than that of a simpler zipper without any lateral modification of the holes, which yields only $g_{\mathrm{OM}}/2\pi \approx 50$ GHz/nm. This is *not* the design that we found to maximize the fit function (which had a larger coupling strength, $g_{\mathrm{OM}}/2\pi \approx 83$ GHz/nm), because that design was unsuitable due to the way the stresses relaxed in that structure caused the beams to bow away from each other, which made it impossible to achieve

gaps between the two beams of less than ≈ 200 nm.

2.2 Si_3N_4 Device Fabrication

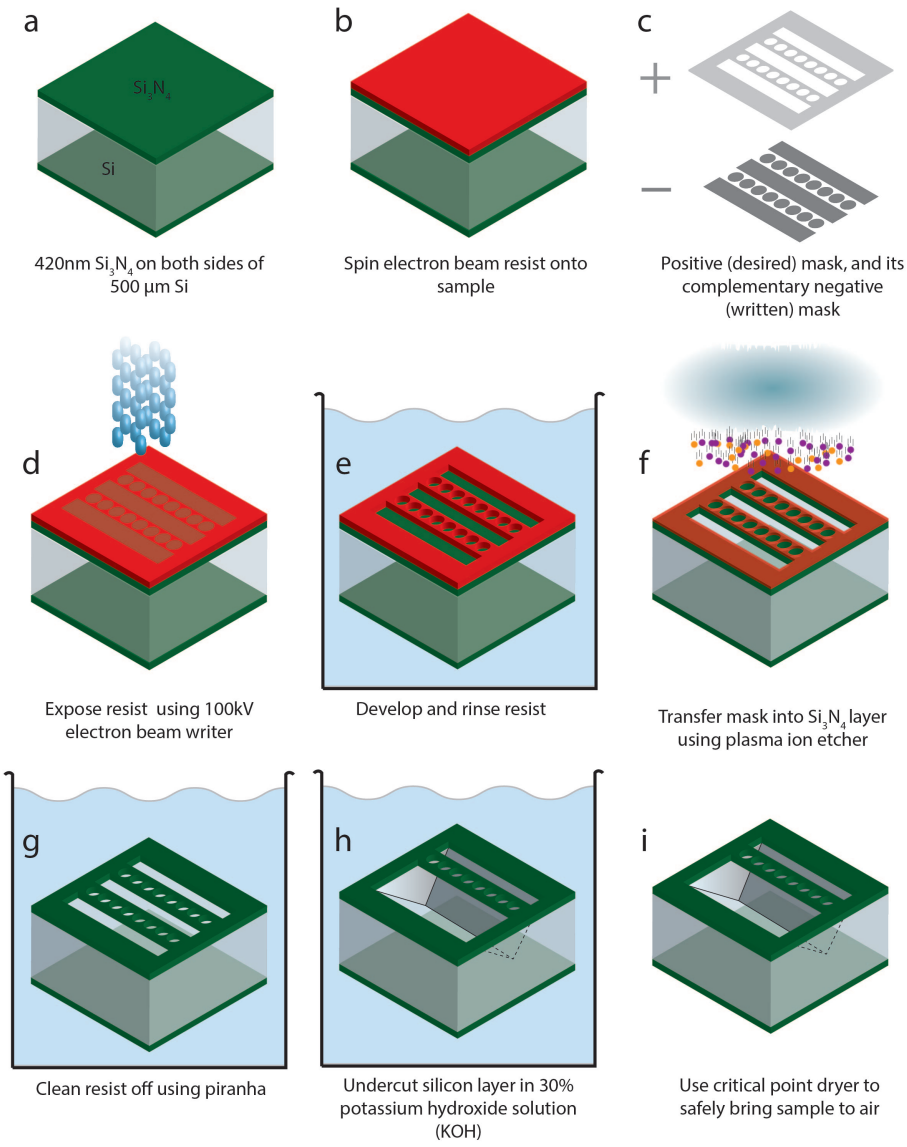

Figure 2.9: **Fabrication Process for Si_3N_4 Optomechanical Resonators.** See text for details. (f) Two colors of impinging atoms represent different molecule species present in the SF_6/C_4F_8 plasma. In (h),(i) one of the photonic crystal beams has been removed to more easily see the undercut trench below released devices.

Here we are going to cover the relatively simple fabrication process for our silicon nitride devices. We describe the fabrication as simple not because it is easy, but because the devices are single-layer and, with a little elbow grease, can be fabricated in a single day. This is in stark contrast to the mul-

tilayer and (at least) week-long turn-around times required to fabricate chip-scale 'optomechanical' devices, which utilize microwave instead of optical light [45]. A simplified version of our fabrication process is shown in Fig. 2.9, and this section will consist of providing details behind each step of this process. Two great references for further details on our methods of fabrication can be found in the theses of Dr. Jeff Hill [2] and Dr. Richard Norte [46].

2.2.1 Pattern Writing

a

Action	Name	Composition	Cost	Vol/use	Cost/use
EB resist	ZEP-520A	Proprietary	25,000$/L	0.6 mL	15$
Developer	ZED-N50	n-Amyl acetate	88$/L	40 mL	3.5$/L
Rinse	ZMD-D	Methyl isobutyle ketone	240$/L	40 mL	9.6$/L
Remover	ZDMAC	Dimethylacetamide	88$/L	40 mL	3.5$/L

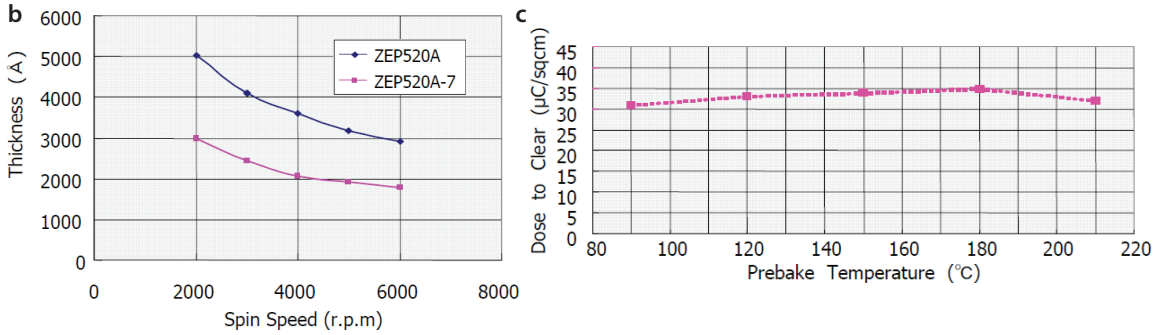

Figure 2.10: **Electron Beam Resist Properties.** (a) Table of the ZEON chemical family used to electron beam pattern our chips before etching and their approximate costs. Note that the sensitive resist is extremely expensive but this is offset by the typically small volume per use (i.e., what is needed to cover a 1cm x 1cm chip). (b) Approximate resulting thickness of ZEP520 films after 120 s spins at given speeds. (c) Plot showing electron dose needed to fully expose (clear) the ZEP520A resist as a function of bake temperature, indicating that precise pre-bake temperature is not critical. Note that the total magnitude of the dose we use differs greatly from that reported in this chart because of the differences between the EBL tool used to take this data compared to the machine we use. All data taken from Ref. [47], except the pricing information comes from a quote from ZEON received on 11/14/2013.

After the design of the optomechanical device is finished, the desired pattern must be etched into the layer of silicon nitride. Due to the small scales ($\approx$ 100 nm) of our Si_3N_4 optomechanical devices, we use Electron Beam Lithography (EBL) to define our structures, which is able to expose patterns with $\approx$ 5 nm resolution and 2.5 nm precision. In this process a stream of electrons is accelerated towards a sample using high voltages (100 kV) and the beam is steered to write the desired pattern

into an electron-sensitive resist in an "Etch-a-Sketch" raster pattern. Limitations of the resist layer's sensitivity and the subsequent processing steps cause the effective smallest-feature-size to be slightly larger at $\gtrsim 30$ nm. Although state-of-the-art optical lithography techniques can create features on the order of 10-20nm, this requires very expensive and complicated masking technologies typically only available in wafer-scale commercial fabrication facilities. At CalTech, the optical lithography equipment we have access to is limited to feature sizes of $\gtrsim 800$ nm. The key reason that (EBL) is able to directly write (i.e., without using any mask) such small structures is that the wavelength of the UV light used for lithography is about 365 nm, but the Compton wavelength for an electron particle is negligible at 2.4 pm.

To prepare our sample for writing, we first spin-on a sensitive electron-beam resist (Fig. 2.9b). In the group we use the resist ZEP520A (see Fig. 2.10), which is useful for its high sensitivity to exposure (i.e., it requires low doses of electrons, $\approx 175\ \mu\text{C/cm}^2$), which significantly reduces the time it takes to write a chip. Even more importantly, it is very good at withstanding the dry-etching process used to transfer our mask into the Si_3N_4. To create a thin and uniform layer of this resist, the sample chip (1 cm $\times$ 1 cm) is secured onto the vacuum-chuck of a spinner (Fig. 2.11) and then 3-4 small drops of the resist are deposited onto the surface of the chip. The spinner then ramps up to a high rotation speed for 60 s. As plotted in Fig. 2.10b, the resulting layer thickness is a function of the rotation speed used. The silicon nitride is very tough to etch and so we use spin rates of 2,000 rpm to create a relatively thick layer, which due to differences in our setup from the data provided in Fig. 2.10b yields a resist thickness of ≈ 400 nm. After spinning, the resist is baked on a hot-plate at 180^o C for 4 min to harden the resist and bake off any excess solvent dissolved in the polymer.

The next step is to expose this chip in the EBL tool (which, at CalTech, is a Leica EBPG 5000+). This machine doses the resist layer in the desired pattern (see Fig. 2.9d). The ZEP520a is a positive resist, which means that the exposed area is the material that gets removed upon application of the developer, and so we write the negative of the desired mask (Fig. 2.9c). It usually does a very good job of faithfully reproducing the desired pattern, but occasionally has difficulties, typically due to failures of its driving electronics. A surprisingly-heartfelt error pattern is shown in Fig. 2.12.

After exposure, the mask is developed by submerging it in ZED-N50 for 2.5 min and then rinsing the chip in ZMD-D for 30 s. The chip is then blow-dried using clean, filtered nitrogen. After this step, the resist has taken on the physical shape that we wish to transfer in to the Si_3N_4 layer. This is shown schematically in Fig. 2.9e and an actual image is shown in Fig. 2.13.

2.2.2 Etching

We then use dry-etching to transfer the resist pattern into the underlying silicon nitride layer. To do this, we use inductively-coupled plasma reactive ion etching (ICP-RIE) whereby a gas of atoms

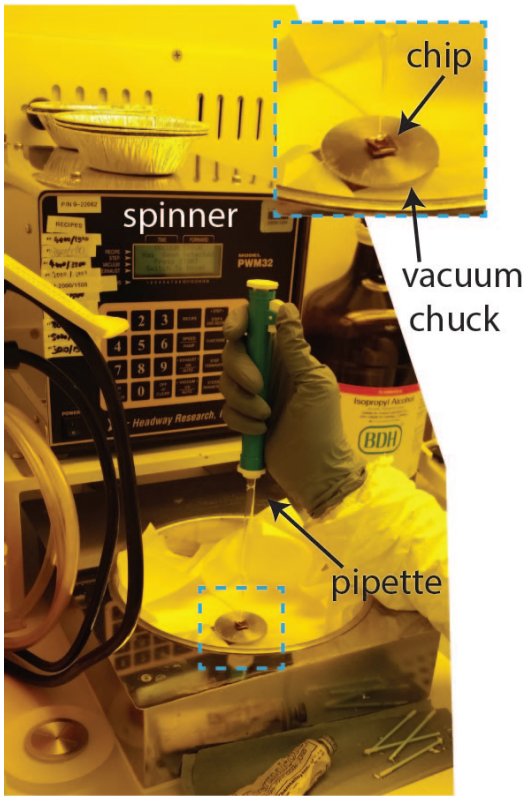

Figure 2.11: **Resist Deposition and Spinning.** Image of device used to spin resist layer on our chips ('spinner') showing someone in the act of pipetting small droplets of ZEP520A onto a 1cm × 1cm chip.

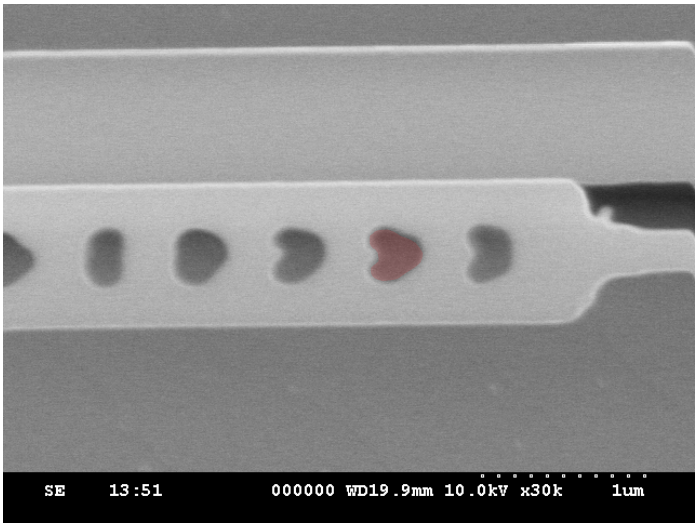

Figure 2.12: **Electron Lithography Failure.** An example of what occurs when the driving electronics of the electron beam gun fail. Although the pattern file contained circles, what has instead been drawn are inexplicably modified shapes.

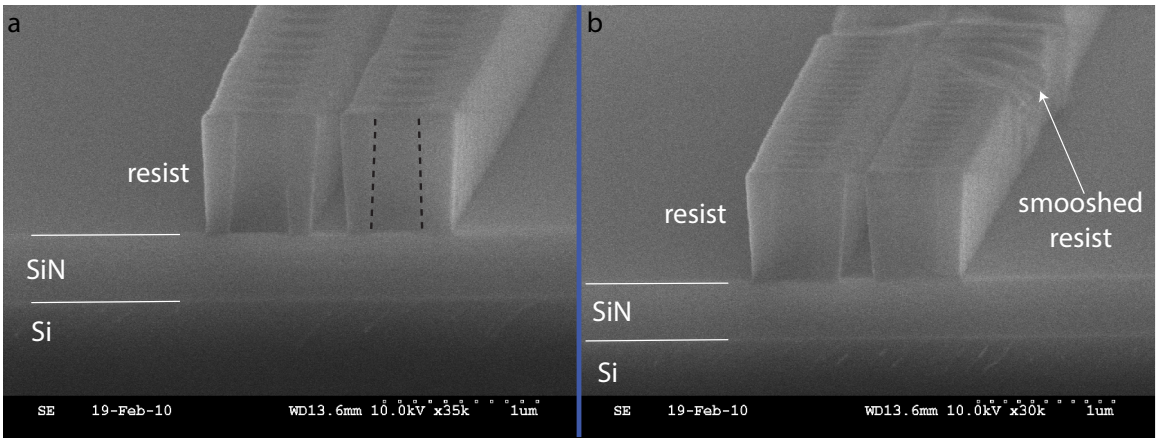

Figure 2.13: **Developed Resist.** (a) Image showing electron-beam resist after exposure and development sitting atop the Si_3N_4-on-Si wafer. The pattern written consists of a zipper cavity with two photonic crystals separated by a small gap. Note that the holes in the resist are wider at the bottom than the top (dashed black lines are a guide to the eye). In the etching step this can cause the holes in the Si_3N_4 to have tilted side-walls as well. The chip has been cleaved in half to allow for this on-edge image to be taken. (b) This cleaving process can damage the relatively soft polymer of the resist as shown here.

is excited into a plasma above the chip and then this plasma is accelerated vertically downward into the chip to etch straight down into it (Fig. 2.9f). The gas chemistry we use consists of a ratio of SF_6 and C_4F_8. The SF_6 is the dominant material etchant because the gas dissociates into SF_x and F_y. The heavy SF_x ions impact the material and vertically mill downwards, while the lighter F_y ions chemically etch the material in an isotropic fashion. The ideal etch would be perfectly vertical, and so to prevent the chemical etching from the free fluorine atoms, the C_4F_8 is added. This gas dissociates primarily into CF_2 and C_z species. Instead of contributing to the etching process, the CF_2 ions tend to deposit on the surface of the material (and everywhere else) and form a cross-linked Teflon-like polymer that inhibits the chemical etching of fluorine. However, the heavy SF_x ions can punch through this forming layer, and therefore the etch is very vertical. This is known as a **pseudo Bosch etch** [48–51], because the better-known Bosch etching process uses these same gases, but alternates between SF_6 and then C_4F_8 instead of using them simultaneously in a continuous fashion. A series of devices with a range of etching quality are shown in Fig. 2.14.

The primary issue with this etch is that it etches the ZEP mask at approximately the same rate as it etches the Si_3N_4 below it. This means that etching our 400 nm thick nitride layer requires a 400 nm thick layer of resist, and for such a thick layer of resist, it is difficult to expose in a way that leave vertical sidewalls in the resist (as in Fig. 2.13a). Also, even when using such a thick masking layer, there is a relatively narrow window in the (large) parameter space for the etching, over which we are able to cut all the way through the Si_3N_4 without also eroding all of the mask away (Fig. 2.14a-e). This is because the high strength of the Si_3N_4 makes it difficult to etch. The

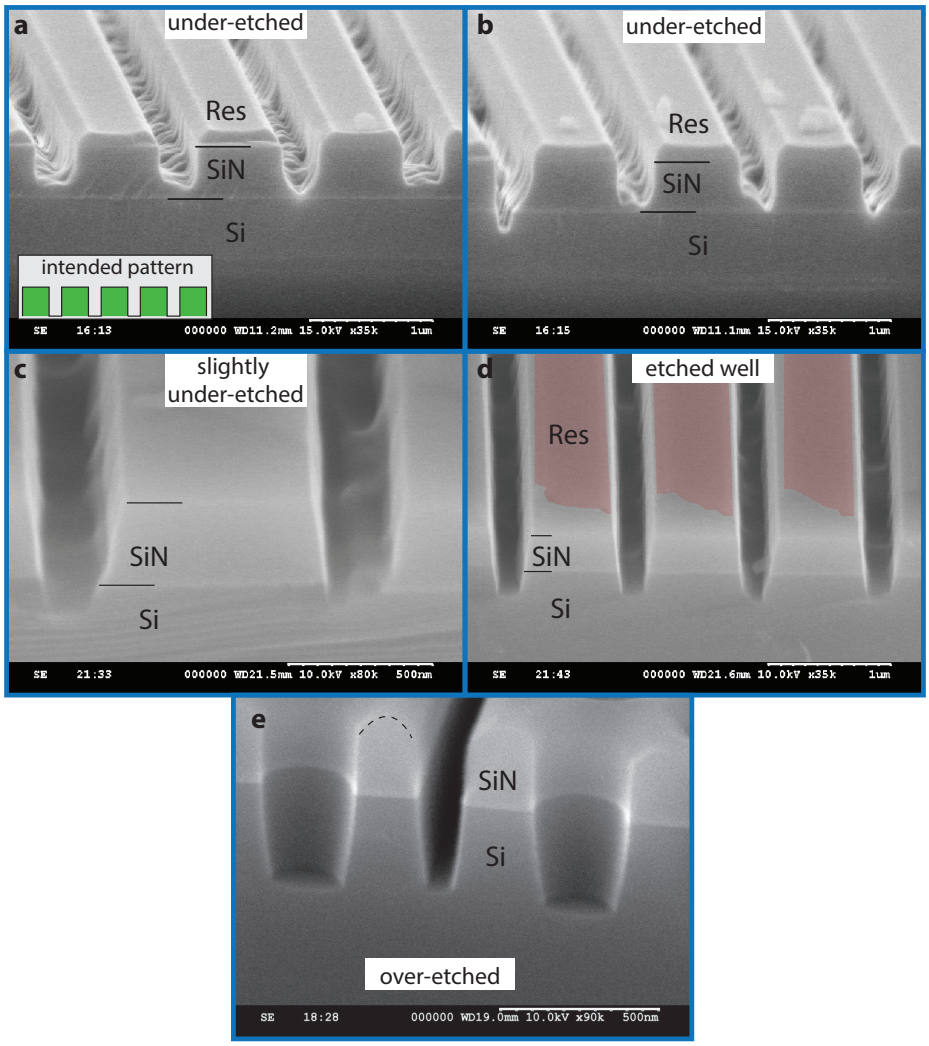

Figure 2.14: **Etching Guide.** (a) Image showing a significantly under-etched sample. The ideal etched pattern of steps is shown in green in the bottom left inset. There is a significant layer of resist left on top of the nitride layer, but there is still a lot of material left in the gaps between the steps. (b) A sample slightly more etched than that in (a), but still very under-etched. (c) Image showing a sample with very small bits of Si_3N_4 left in between the steps. (d) A sample that is etched reasonably well showing nearly-straight sidewalls in the SiN layer. The remaining debris between the beams is unevenly etched Silicon. The very thin remaining layer of resist is highlighted in red. This shows that we don't have good selectivity of our etch between the device layer and the resist layer. (e) Different pattern than in (a-d), but showing clearly an over-etched sample. Note the rounding of the top corners of the nitride layer (black dashed line is a guide to the eye) and the unnecessarily-deep etching of the silicon layer underneath. The resist layer has been completely etched away at this point.

silicon layer underneath is much softer and etches at a significantly faster rate, requiring significantly thinner resist layers ($\approx$ 200 nm, see Section 2.4). There exist other, possibly better, etch chemistries for silicon nitride (such as CHF_3 and O_2) but we have not attempted to use them.

2.2.3 Wet Chemistry and Final Release

The first step after finishing an etch is to image it in the SEM to determine the quality of the etch and decide whether the parameters need adjusting. Then we clean off most of the remaining resist layer in a strong solvent such as trichloroethylene (TCE). To remove the last vestiges of the resist and anything else on the chip we place the chip in a very strong cleaning solution known as piranha (Fig. 2.9g). This solution consist of a 3:1 mixture of sulfuric acid (H_2SO_4) and 30% hydrogen peroxide solution (H_2O_2). Either substance by itself is dangerous, and combining them yields a rapid exothermic reaction that can bubble violently and even explode if mixed incorrectly. Contrary to most other solutions, when making piranha, the acid should be poured *first* and then the hydrogen peroxide is later added. The benefit to this danger is that it is a very strong oxidizer and in 10 minutes is able to remove nearly all organic material, even very stable elemental carbon allotropes (i.e., soot). The piranha clean is followed by several rinses in filtered de-ionized water (DI) to ensure there is no lingering acidity.

After cleaning, we release the Si_3N_4 from the underlying Si layer by dipping the chip into a solution of 30% potassium-hydroxide (KOH) heated to $\approx 70^\circ$ for 10 min (Fig. 2.9h). At this temperature, the KOH removes silicon at a rate of nearly 1 μm/min while etching the Si_3N_4 at an imperceptibly slow rate. It should be noted that the KOH etch proceeds quickly only along specific crystal planes of silicon [52–54] with a selectivity approaching 100:1 for the $\langle 100 \rangle$ direction compared to the $\langle 110 \rangle$ direction. The resulting undercut etch profile resembles a 'V' or inverted pyramid shape with the walls inclined at 54.74° from the plane of the chip, as shown in Fig. 2.9h-i. We don't take advantage of this fact in the experiments presented here, but our colleagues have used it to design self-aligned couplers for getting light efficiently onto and off of the chip [55], and this coupling scheme could prove to be an enabling technology for more practical versions of the optical accelerometer presented in Chapter 3.

The final wet chemical step is to again piranha clean the sample to remove any debris present after the KOH undercut.

2.2.4 Critical Point Drying

Unlike in the previous steps, now that the devices have been released and are able to flexibly move, we *cannot* simply blow-dry the sample in nitrogen. For our nanoscale devices, the capillary and surface tension forces imparted to our devices from this drying action are very significant. If the devices are dried in the presence of these forces, the narrow gaps between the two sides of the zipper photonic crystal are pulled towards each other and result in the devices being permanently stuck together by van der Waals forces. To avoid this we employ a critical point dryer (CPD), which takes a fluid (usually CO_2) around its phase-diagram critical point through a mix of temperature

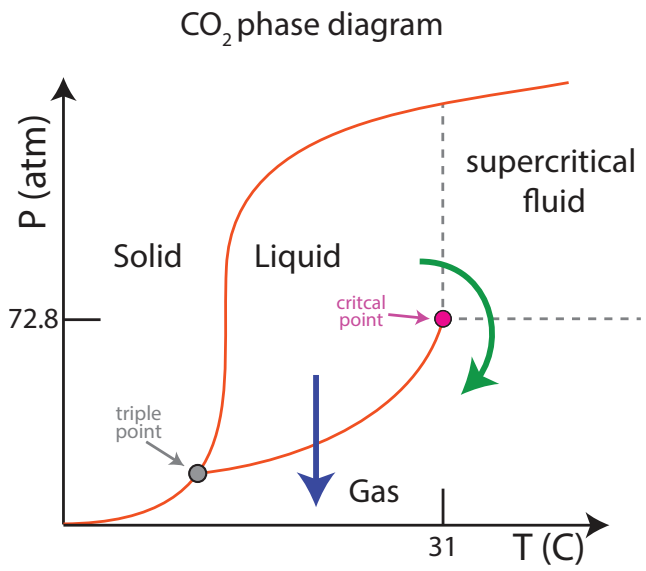

Figure 2.15: **Going Around the Critical Point.** The phase diagram of CO_2 showing schematically the path taken by simply air-drying the sample (blue arrow) and the path taken by the CPD around the critical point (green arrow).

control and high-pressures. This works because, for a fluid past its critical point, there is no longer a meaningful difference between the liquid and gaseous phases. It is at the interface between liquid and gas where the surface tension forces are present, so such a path through the supercritical region avoids these forces.

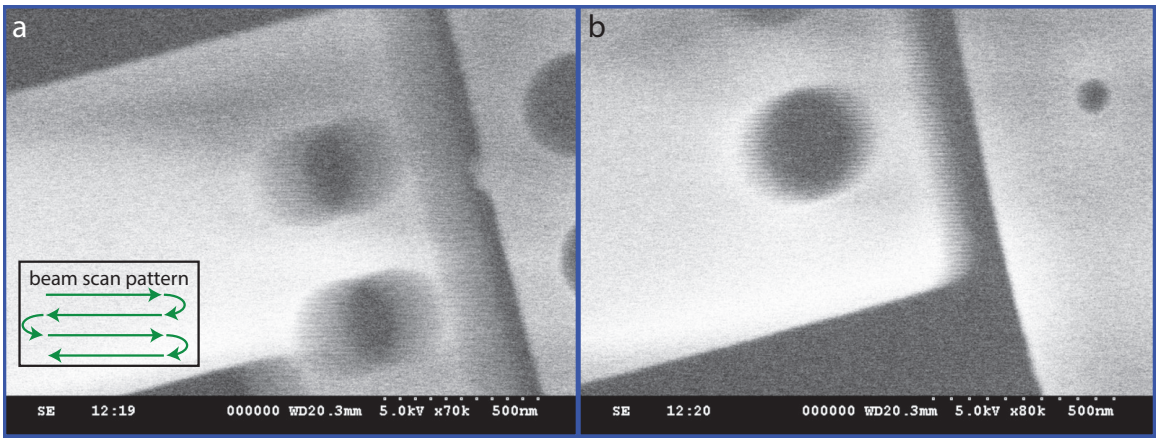

Figure 2.16: **SEM Excitation of Mechanical Motion.** (a) SEM image of the top of the 'zipper' photonic crystal where the left side is attached to a low-frequency ($f_{\mathrm{m}} = 27$ kHz) high-quality $Q_{\mathrm{m}} \approx 1\times10^{6}$ mechanical oscillator. Blurring and aliasing of image on the left hand side indicates rapid motion of that beam induced by the scanning electron beam. Scanning pattern of electrons is shown in bottom left inset. (b) Same as (a) but of the bottom section of the photonic crystal again displaying motion. Note that rotating the photonic crystal by ≈ 90 degrees so that the photonic crystal axis is along the scanning direction of the electron beam can prevent this problem.

The sample is first removed from the KOH etchant into several DI water rinses, which must be done carefully and quickly to avoid the samples drying while in between the liquid baths. Then the sample is immersed in filtered isopropyl alcohol (IPA) and transferred into the CPD chamber containing filtered IPA. The machine cools down, then slowly displaces the IPA with liquid CO_2, and begins the path through the supercritical phase region, as illustrated in Fig. 2.15.

One of the most important aspects of this process is avoiding any contamination of the CPD chamber. If the sample gets dirty during this drying step one cannot clean the chip without again introducing it to a liquid piranha solution (or strong solvent), which then requires using the possibly contaminated CPD chamber. The most common source of dirt at this stage is due to residual chemicals in the chamber other than CO_2, such as small volumes of piranha trapped in parts of whatever chip-holder one is using. Also, if the purging of IPA does not proceed slowly enough there will still be some in the chamber when the cycle begins, and due to its much higher critical point ($= 235°$ C, 53 atm) the IPA will just pass directly from liquid to gas. However, if operated properly and with care, one rarely encounters problems at this stage.

Finally, one should always check the finished device in both the optical microscope and the SEM to ensure there is no unwanted dirt/debris or other issues with the finished chip. However, one must be careful when doing this, because the fabricated devices can be very fragile. One unexpected problem we encountered when fabricating our low-frequency optomechanical accelerometer devices (Chapter 3) was that we would occasionally collapse the two sides of the photonic crystal together. We found that the raster-scanning of the SEM's electrons imparted a small lateral force to the insulating Si_3N_4 layer, which would tend to ring-up the mechanical element to very large oscillation amplitudes until, often, it slammed into and then stuck to the other half of the photonic crystal. In Fig. 2.16 we show a couple images taken while the SEM was inducing oscillations in one such released mechanical resonator.

Now armed with a finished set of devices, the next step is to determine the optical and mechanical characteristics of the fabricated devices as laid out in the experiments of Chapter 3 and Chapter 4.

2.3 Device Design: Silicon Optomechanical Crystals

In this section we will go through all of the steps required to design and fabricate a silicon optomechanical crystal. However, having just covered these topics in detail in the context of Si_3N_4, we will focus primarily on the differences between the two systems. For a full account of the process we recommend reading the corresponding sections for Si_3N_4 as well (also, the thesis of Dr. Matt Eichenfield [34] and Dr. Jasper Chan [35]).

Silicon is an exciting optomechanical material because it is one of the most commonly-used materials in standard electronics and MEMs applications, so it is compatible with many existing

Material	Si (undoped)		
Structure	Crystal (interpenetrated fcc)		
Layer Thickness	220 nm	Index (@ 1550nm)	3.4
Density	2330 kg/m^3	Electrical Resistivity	1400 Ω-m
Young's Modulus	160 GPa	Thermal Conductivity	149 W/m/K
Hardness	10 GPa	Specific Heat	0.7 J/g/K

Table 2.2: **Si Properties.**

processes for real-world devices. It is also better than Si_3N_4 in that it has a much higher optical index, $n_{Si} = 3.4$, is a crystalline material with high thermal conductivity, and as discussed in Section 2.3.3, silicon has a second additional contribution to the coupling strength (g_{OM}). The main drawback of silicon is that its room-temperature mechanical quality factors are typically low ($Q_m < 5,000$), but because it is a crystalline material, as it gets cooled down to cryogenic temperatures, these quality factors improve significantly to $Q_m > 1\times10^5 - 10^6$. In contrast, silicon nitride improves by only a factor of 2 while going from 295 K to 20 K. This difference leads us to typically employ silicon in sufficiently scientifically valuable experiments where the use of expensive cryogenic equipment can be justified [11, 17, 56, 57] (Chapter 5), but we choose Si_3N_4 for more practical applications [55, 58] (Chapters 3 and 4).

Finally, because of the higher index and secondary coupling mechanism present in Si, this material is much better for doing experiments with high-frequency, $f_m \gtrsim 1$ GHz, side-band resolved optomechanical systems. Using Si_3N_4, it is simply extremely difficult to get the large g_{OM}'s that these challenging experiments require. The devices in this section are referred to as 'optomechanical crystals' (OMC) because in the same way that the modified periodicity of the holes traps optical waves of certain frequencies of ≈ 200 THz, it simultaneously traps mechanical waves of frequencies in the GHz band.

2.3.1 Silicon: Optics

At the telecom wavelengths that we use ($\lambda \approx 1550$ nm), silicon has very low loss and photonic crystals have been realized with $Q_o > 1\times10^6$ [59, 60]. These large quality factors can be achieved in part because silicon's higher index allows for more optical field to be localized in the material, and

also this higher index leads to larger and more robust optical bandgaps (as in Fig. 2.3). The most significant drawback of silicon as an optical material originates from its status as a semiconductor with a small *electronic* bandgap of 1.1 eV (compared to that of Si_3N_4 at 5 eV). A photon at 1550 nm (= 0.8 eV) does not have enough energy to excite free carriers across this bandgap, but the small mode-volumes of our photonic crystals lead to non-negligible two-photon absorption processes capable of delivering enough energy (= 1.6 eV) to span this bandgap and excite free electrons (and holes) in the material. This process can cause the photonic crystal to heat up and can degrade both the optical and mechanical quality factors [11].

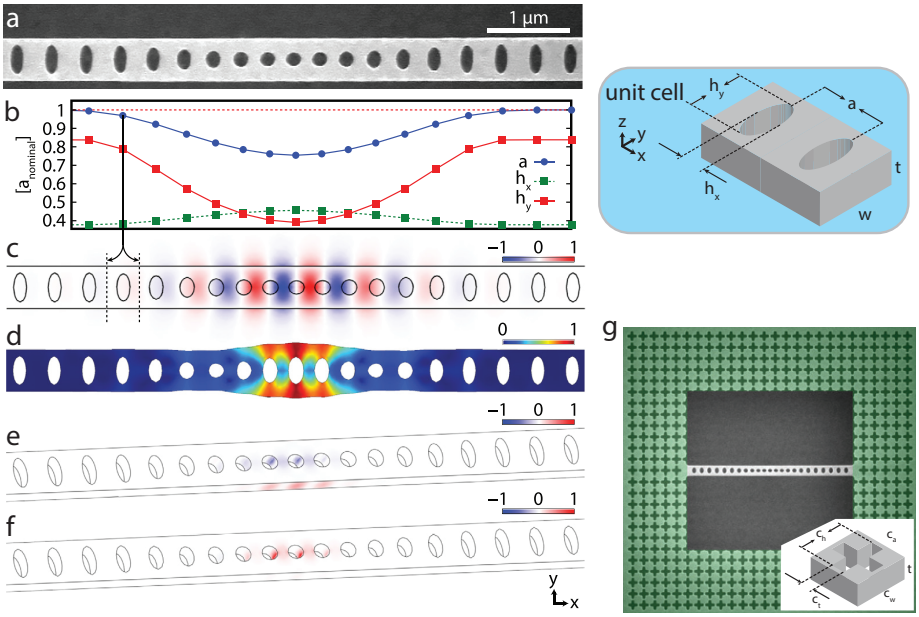

Figure 2.17: **Silicon OMC.** (a) SEM image of the central cavity region of a silicon optomechanical crystal similar to that used in Chapter 5. (b) Chart of the change in the lattice constant (a, blue), hole height (red, h_y), and hole width (green, h_x), in units of the nominal lattice constant in the periodic mirror region, $a_{nominal}$. Unit cell figure on the right demonstrates what each parameter corresponds to in the crystal. (c) Simulated normalized electric field component, E_y, of the fundamental optical mode. (d) Simulated normalized motion of the fundamental mechanical mode (displacement greatly exaggerated). (e) Density color plot of the moving boundary component of the optomechanical coupling $g_{OM,MB}$ corresponding to the integrand of Eq. (2.6). (e) Density color plot of the photo-elastic component of the optomechanical coupling $g_{OM,PE}$ corresponding to the integrand of Eq. (2.7). (g) SEM showing the entire device and surrounding phonon radiation shield (green overlay). Figure adapted from Ref. [61].

Design of silicon photonic crystals follows the same principles of band-gap engineering and small modulations of a periodic structure as described previously (Fig. 2.3). In Fig. 2.17 we show a single 1D photonic crystal that is designed for coupling to a colocalized mechanical mode [61]. This optomechanical crystal was designed in our group using an algorithmic optimization process developed by Dr. Jasper Chan, and this was the inspiration for re-designing the zipper photonic crystal as

described in Section 2.1.3. Realizations of this photonic crystal in our group have demonstrated $Q_o > 1\times10^6$, but the most interesting components of this design are the mechanical and optomechanical properties.

2.3.2 Silicon: Mechanics

As indicated by the 'breathing' motion shown in Fig. 2.17d, the mechanical modes of interest that we are going to focus on are very different from the whole-beam modes of Fig. 2.5. This mechanical mode exists because it is trapped by the phononic crystal created by the same periodicity of the holes. These mechanical modes are very useful because their high-frequencies allow us to enter the regime of sideband resolved optomechanics where $\omega_m > \kappa/2$ (see Section 1.3). Secondly, by using the same crystal to trap both fields, they naturally tend to have large overlap, and thus large coupling to each other. The mechanical design principles behind this structure are laid out clearly in Ref. [61].

One significant difference of these mechanical modes is that their wavelengths are so small ($\approx$ 2 μm) that it is feasible to prevent emission of energy into the bulk substrate using a 'radiation shield' as shown in Fig. 2.17g (green overlay). The unit cell of this cross structure is shown in the bottom right inset. The series of small bridges connecting large masses leads to a structure that has a very large band-gap ($\Delta f_{BG} \approx 800$ MHz) and so mechanical waves emitted from the center of the beam are unable to propagate in this shield, and are thus trapped in the beam. At room-temperature the quality factors of these high-frequency modes are limited by thermo-elastic damping (TED) effects and so the shield has little effect. However, as the structure is cooled down to cryogenic temperatures of $\lesssim 100$ K the quality factor begins to be limited instead by radiation into the bulk, and here the phononic shield is necessary to achieve $Q_m \approx 600,000$ as measured in these devices [35].

2.3.3 Silicon: Optomechanical Coupling

The optomechanical coupling in silicon crystals is composed primarily of a moving boundaries component ($g_{OM,MB}$) and a component due to the photo-elastic effect ($g_{OM,PE}$). Due to its higher optical index, the moving boundaries component, $g_{OM,MB}$, tends to be larger for a given moving face element than for that in Si_3N_4. However, the colocalized nature of the optical and mechanical modes often causes there to be just as many faces moving towards regions of higher electric field density (positive contribution to $g_{OM,MB}$) as there are faces moving towards lower electric field density (negative contribution to $g_{OM,MB}$), as shown in both the positive and negative components in Fig. 2.17f. When integrated over the entire surface of the beam, these effects tend to cancel each other out, and the $g_{OM,MB}$ component can be smaller than expected.

Instead, the dominant optomechanical coupling in these devices is the photo-elastic component whereby a local strain of the material causes a change in the material's index. It can be calculated

using first-order perturbation theory as [35]

$$g_{\mathrm{OM,PE}} = -\frac{\omega_{\mathrm{o}}}{2}\frac{\langle \boldsymbol{E}|\frac{\partial \epsilon}{\partial \alpha}|\boldsymbol{E}\rangle}{\int \boldsymbol{E}\cdot\boldsymbol{D}dV}, \tag{2.7}$$

where α is a generalized coordinate for the amplitude of the mechanical deformation vector, $\boldsymbol{Q}$. The form of the photo-elastic contribution can be quite complicated, but for an isotropic medium with a given index n, it can be written as $\frac{\partial \epsilon}{\partial \alpha} = -\epsilon_0 n^4 p_{ijkl} S_{kl}$, where $\boldsymbol{p}$ is the material's rank-four photo-elastic tensor and $\boldsymbol{S}$ is the strain tensor (which is determined along with the simulation of the mechanical mode, $\boldsymbol{Q}$). The normalized contribution of this component to the g_{OM} is shown in Fig. 2.17f, where it should be noted that it has the same sign nearly everywhere (positive, red). The reason we do not need to consider this coupling in Si_3N_4 is the n^4 dependence of this term means that we would expect this effect to be much smaller (the components of p_{ijkl} are smaller as well).

The device presented here has $g_{\mathrm{OM,MB}}/2\pi = -33$ GHz/nm and $g_{\mathrm{OM,PE}}/2\pi = +306$ GHz/nm. In practice it is extremely difficult to design a structure where these two components add together with the same sign instead of subtracting (and thus lowering the overall g_{OM}). The measured coupling in this device is actually larger than expected, $g_{\mathrm{OM}}/2\pi = 354$ GHz/nm, which we attribute to imprecision in our knowledge of silicon's photo-elastic tensor values at $\lambda = 1550$ nm.

2.4 Silicon: Device Fabrication

The creation of our silicon optomechanical crystals is laid out schematically in Fig. 2.18 and explained in the following sections.

2.4.1 Pattern Writing

We first spin-on electron beam resist to evenly cover the 220 nm silicon top layer of the chip (Fig. 2.18b). The silicon layer is nearly half as thick as our Si_3N_4 layer because the higher index of Si requires a correspondingly thinner photonic crystal to achieve the same resonant wavelength (all else being equal). Due to this fact, we spin-on resist at a much faster 5,000 rpm rate, which yields a ZEP520A layer of approximately 200 nm. We then bake it at 180° C to harden the resist.

After the subsequent electron beam exposure (Fig. 2.18d) we develop and rinse the resist again in ZED-N50 and ZMD-D respectively (Fig. 2.18e) .

2.4.2 Etching

We use the same C_4F_8/SF_6 gas chemistry to etch the silicon. The etching of silicon is significantly easier than that of silicon nitride, because it etches at a rate ≈ 4 times faster than the masking ZEP

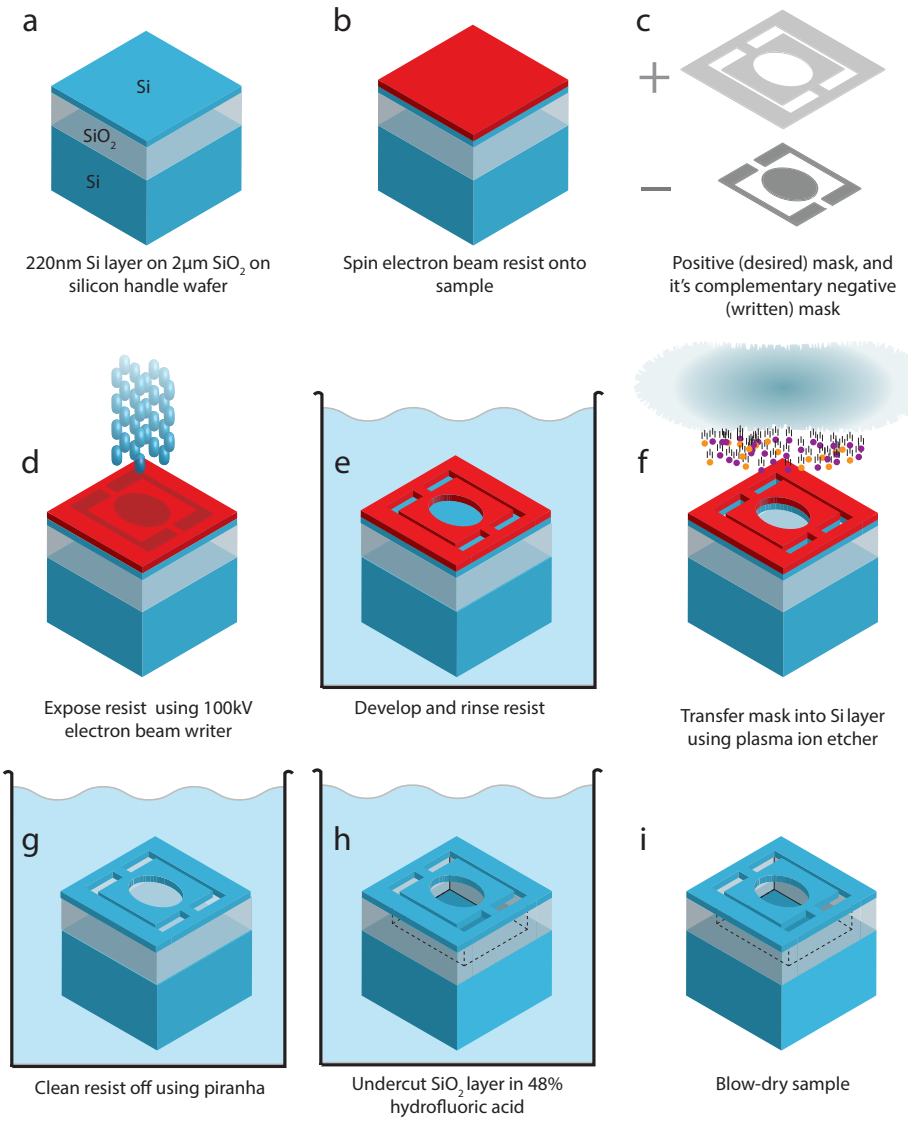

Figure 2.18: **Fabrication Process for Si Optomechanical Crystals.** See text for details. (f) Two colors of impinging atoms represent different molecule species present in the SF_6/C_4F_8 plasma.

layer. This means that, if done correctly, the sample can be fully etched through with very little erosion of the mask (see Fig. 2.19). The thesis of Dr. Jeff Hill covers etch optimization processes for both silicon and silicon nitride in fantastic detail [2].

2.4.3 Wet Chemistry and Final Release

It is in these final steps that the fabrication process really diverges from that of Si_3N_4. After removing the resist layer in a piranha clean, we undercut the glass layer below using 48% hydrofluoric acid (HF) for 90 sec (Fig. 2.18h). Unlike the KOH attacking silicon, this HF acid etch removes the SiO_2

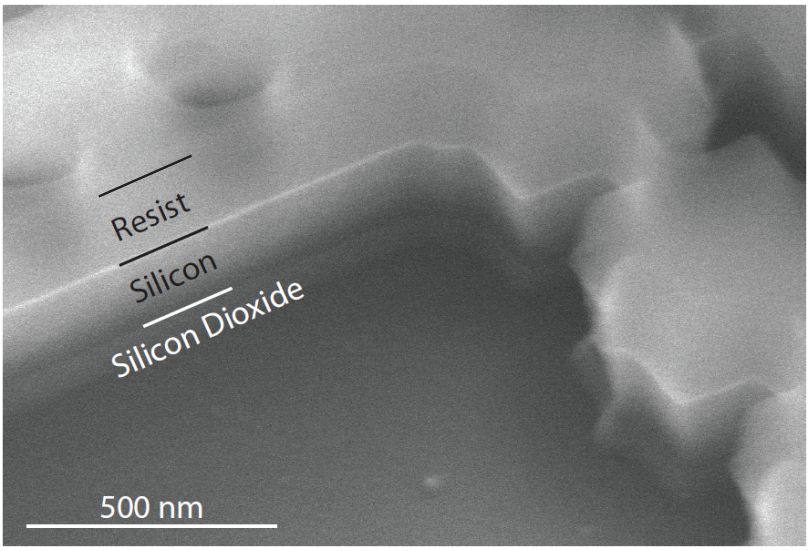

Figure 2.19: **Etched Silicon.** SEM image of a silicon device after etching showing a thick resist layer remaining.

layer in an isotropic fashion and so one must be careful not to leave the chip in too long, or else the released structure will be weakly supported and may start to sag or buckle. A SEM image of a completed device is shown in Fig. 2.20, where the lighter regions indicate where the HF acid has etched away the underlying glass layer.

Note: HF is an extremely dangerous acid and should never be handled without the proper safety precautions. Whereas a typical acid burns the skin on contact (alerting the user to a problem), HF does no immediate damage to the user. Instead, it painlessly absorbs through the skin until reaching the bones where the it begins to leach them of calcium. At this point, extreme pain begins, but this can often be too late for useful medical intervention. Possible exposure should be reported and treated immediately regardless of symptoms.

2.4.4 Surface Passivation

In principle, the device processing is finished after the previous stage and the sample could be safely dried at this point. In practice, we find that stopping at this stage leads to devices with significantly worse optical and mechanical properties [35, 62]. So, the group has developed a series of quick cleans/etches that remove dangling (lossy) OH bonds at the surface of the material and also smooths out small imperfections in the Si surface left by the ion etching step. This process consists of performing a piranha clean (10 min) followed by a dip in dilute 20:1 HF:H_2O acid for 60 s. This clean/etch combination is repeated 3 times, always ending with the dilute acid step. If a chip is accidentally dirtied during use, this 3× process is effective at cleaning the sample and often returns the chip to previous levels of performance. However, each application strips a small bit of Si

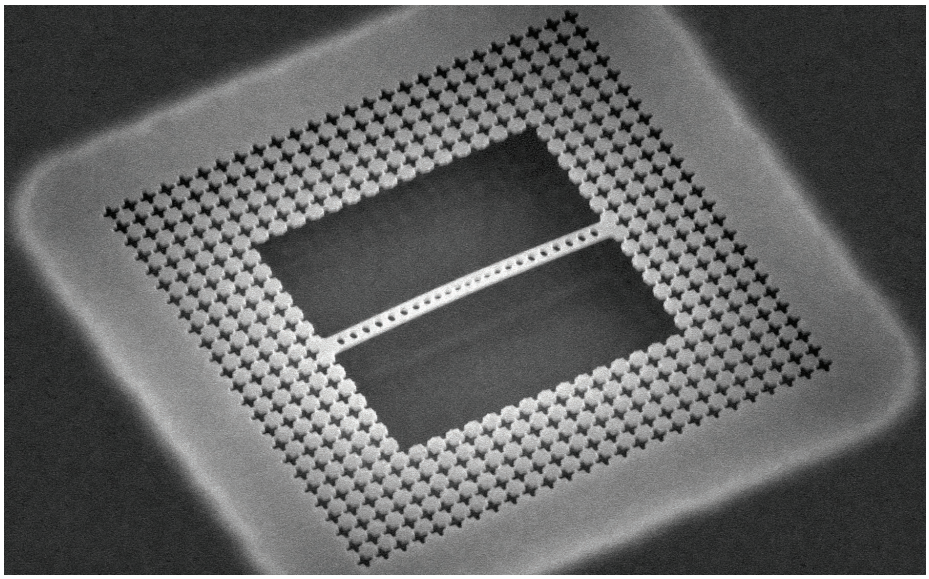

Figure 2.20: **Undercut Silicon Device.** SEM image of a silicon device after the HF undercut. Lighter region surrounding the device indicates area where the SiO_2 layer has been removed.

material from the edges, so this 'magic cleaning' cycle can only be performed 3-4 times (i.e., 10-12 piranha/HF dips) before the optical and mechanical properties shift too much for the device to be useful.

2.4.5 Non-Critical Drying

The best part of making these 1D silicon optomechanical crystals is that they usually do not require the use of a CPD. In this single-beam design there is no small gap that could be collapsed by forces in the drying stage. Thus, after appropriate rinses in DI water (at least 2× 30 s), the sample can simply be blow-dried using clean nitrogen (Fig. 2.18i). If the silicon chip does have small gaps or flexible components it may still require a CPD step.

Finally, the chip is ready to be tested and characterized, as in the experiment in Chapter 5.

Chapter 3

Demonstration of an Optomechanical Accelerometer [58]

3.1 Introduction

The monitoring of accelerations is essential for a variety of applications ranging from inertial navigation to consumer electronics [63] (see Fig. 3.1). The basic operation principle of an accelerometer is to measure the displacement of a flexibly mounted test mass; sensitive displacement measurement can be realised using capacitive [64, 65], piezo-electric [66], tunnel-current [67], or optical [68–71] methods (see Fig. 3.2). While optical readout provides superior displacement resolution and resilience to electromagnetic interference, current optical accelerometers either do not allow for chip-scale integration [68] or require bulky test masses [69, 70]. Here we demonstrate an optomechanical accelerometer that employs ultra-sensitive all-optical displacement read-out using a planar photonic crystal cavity [72] monolithically integrated with a nano-tethered test mass of high mechanical Q-factor [31]. This device architecture allows for full on-chip integration and achieves a broadband acceleration resolution of 10 $\mu g/\sqrt{\text{Hz}}$, a bandwidth greater than 20 kHz, and a dynamic range of 50 dB with sub-milliwatt optical power requirements. Moreover, the nano-gram test masses used here allow for optomechanical back-action [73] in the form of cooling [74] or the optical spring effect [75, 76], setting the stage for a new class of motional sensors.

Due to the rapid development of silicon micro machining technology, MEMS accelerometers have become exceedingly popular over the last two decades [63]. Evolving from airbag deployment sensors in automobiles to tilt-sensors in cameras and consumer electronics products, they can now be found in a large variety of technological applications with very diverse requirements of their performance metrics. While sensors for inertial navigation systems require low noise levels and superior bias stability [77], large bandwidth is crucial for sensors in acoustics and vibrometry applications. However, there is a fundamental tradeoff between noise performance and bandwidth which can be understood from the basic operation principle of an accelerometer, illustrated in Fig. 3.3a. When subjected

to an acceleration $a(\omega)$ at frequency ω, a mechanically compliant test mass experiences a displacement $x(\omega) = \chi(\omega)a(\omega)$ proportional to the mechanical susceptibility $\chi^{-1}(\omega) = \omega_{\rm m}^2 - \omega^2 + i\frac{\omega\omega_{\rm m}}{Q_{\rm m}}$. Here, $\omega_{\rm m} = 2\pi f_{\rm m} = \sqrt{k/m_{\rm eff}}$ is the (angular) resonance frequency of the oscillator and $Q_{\rm m}$ is its mechanical Q-factor (see the plot of $|\chi(\omega)|$ in Fig. 3.3b for $Q_{\rm m} = 10$). Usually, accelerometers are operated below their fundamental resonance frequency $\omega_{\rm m}$, where $\chi(\omega) \approx 1/\omega_{\rm m}^2$ exhibits an almost flat frequency response. This naturally leads to a tradeoff between resolution and bandwidth, since the large resonance frequency required for high-speed operation results in vanishingly small displacements. As a result, the performance of the displacement sensor constitutes a central figure of merit of an accelerometer. For example, resolving an acceleration of 1 μg (where g = 9.81 m/s^2) with an oscillator at $f_{\rm m} = 10$ kHz requires a displacement resolution of 2.5 fm/$\sqrt{\rm Hz}$.

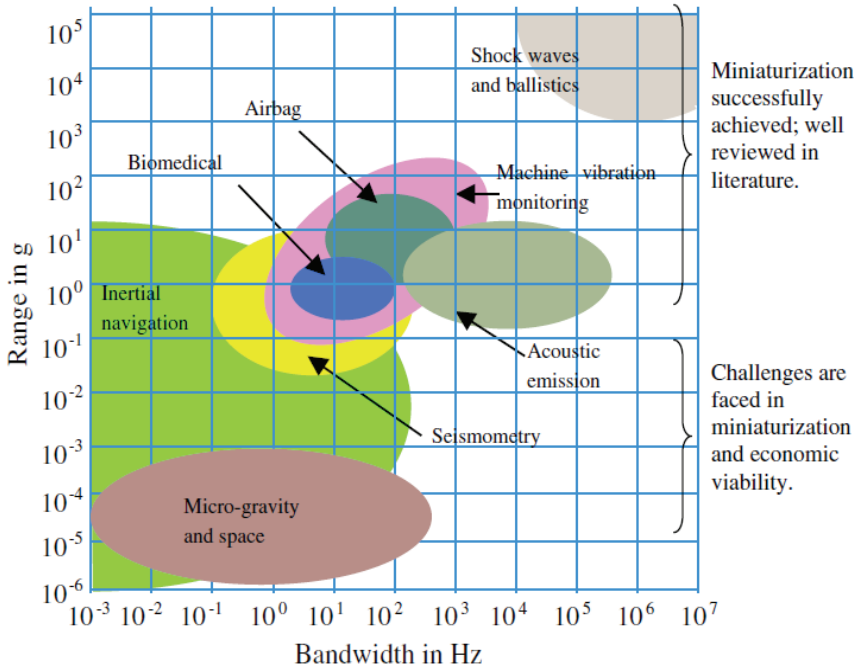

Figure 3.1: **Accelerometer Application Ranges.** Re-printed from Ref. [68].

In a cavity optomechanical system, a mechanically compliant electromagnetic cavity is used to resonantly-enhance read-out of mechanical motion [79]. Such systems have enabled motion detection measurements with an imprecision at or below the standard quantum limit (SQL) [80–82], corresponding to the position uncertainty in the quantum ground-state of the mechanical object. Clever quantum back-action evading techniques [83] aside, only for an ideal cavity system (no parasitic losses) can the actual displacement sensitivity reach the SQL due to fluctuating radiation pressure forces arising from shot noise of the probe light [6]. The average radiation pressure force, on the otherhand, can be quite large in micro- and nano-scale optomechanical devices, and offers the unique capability to control the sensor bandwidth via the optical spring effect [75, 76] and the sensor's

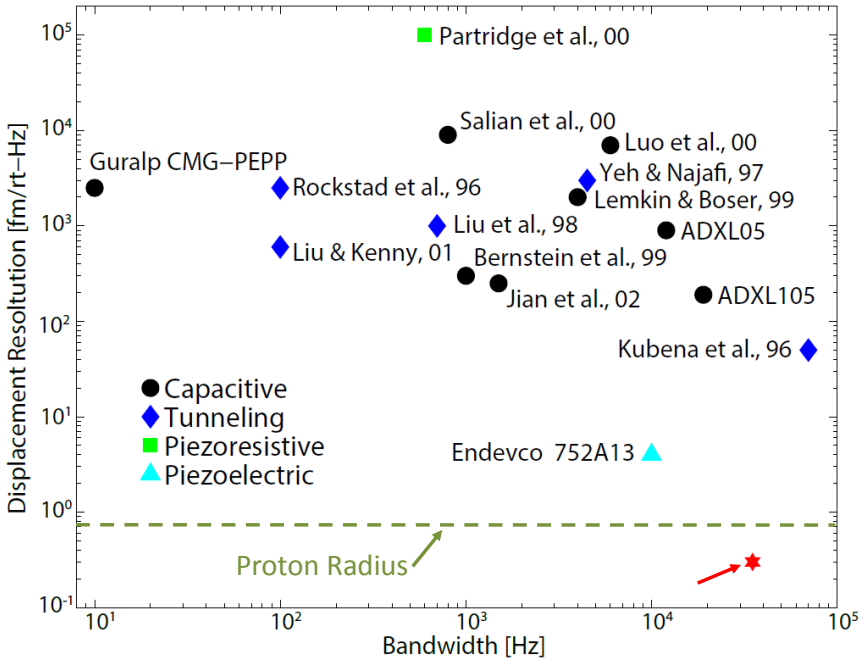

Figure 3.2: **Common Sensor Resolutions.** Plot of several accelerometer's displacement resolution density versus operation bandwidth, adapted from Ref. [78]. The red-star point corresponds to the resolution demonstrated with one of our optomechanical accelerometers, similar to that presented in this chapter. For a scale reference we have indicated the charge radius of a proton ≈ 0.8 fm.

effective temperature via passive damping [73] or feedback cold-damping [74, 84].

In this work, we utilize an integrated silicon-nitride (SiN) zipper photonic crystal optomechanical cavity [72] (see Section 2.1.1) to provide shot-noise-limited read-out of mechanical motion with imprecision near the SQL, enabling high-bandwidth and high-resolution acceleration sensing. The resolution of an accelerometer can be quantified by a noise-equivalent acceleration, NEA $= \sqrt{a_{\rm th}^2 + a_{\rm det}^2 + a_{\rm add}^2}$, in units of g/$\sqrt{\rm Hz}$. The first term in the NEA is due to thermal Brownian motion of the test mass [85]($a_{\rm th}$, Section 3.1.1) while the remaining two terms arise from the aforementioned displacement readout noise ($a_{\rm det}$, Section 3.1.2) and added noise (back-action) onto the test mass due to the act of measurement ($a_{\rm add}$, Section 3.1.3).

3.1.1 Noise from thermal Brownian motion ($a_{\rm th}$)

In contact with a heat-bath at room temperature, the test-mass oscillator is subjected to thermal Brownian motion. From the equipartition theorem, the root-mean-square displacement of a harmonic oscillator is given by

$$x_{\rm rms} = \sqrt{\frac{k_{\rm B}T}{k}}. \tag{3.1}$$

If we assume the acceleration-noise exerted by the bath to be white, i.e., frequency-independent, its power-spectral density S_{aa}^{th} has to obey

$$x_{\mathrm{rms}}^2 = \int_0^\infty |\chi(\omega)|^2 \, S_{aa}^{th}, \tag{3.2}$$

such that thermal test-mass motion corresponds to an NEA of

$$a_{\mathrm{th}} = \sqrt{S_{aa}^{th}} = \sqrt{\frac{4k_B T \omega_{\mathrm{m}}}{m_{\mathrm{eff}} Q_{\mathrm{m}}}} = \sqrt{\frac{4k_B T \gamma}{m_{\mathrm{eff}}}}. \tag{3.3}$$

In the device presented in this work, we have $\omega_{\mathrm{m}} = 2\pi \times 27.5$ kHz, $m_{\mathrm{eff}} = 10^{-11}$ kg, $Q_{\mathrm{m}} = 1.4 \times 10^6$, $T = 295$ K, and therefore $a_{\mathrm{th}} = 1.4$ $\mu\mathrm{g}/\sqrt{\mathrm{Hz}}$.

Driving the harmonic oscillator with susceptibility $\chi(\omega)$, this NEA translates into frequency-dependent displacement noise according to

$$S_{xx}^{th}(\omega) = \frac{4k_B T \omega_{\mathrm{m}}}{m_{\mathrm{eff}} Q_{\mathrm{m}}} \frac{1}{\left(\omega^2 - \omega_m^2\right)^2 + \left(\frac{\omega \omega_m}{Q_m}\right)^2}. \tag{3.4}$$

Thus we see that fundamental to minimizing the NEA is a reduction in the intrinsic thermal noise, a_{th}, which according to equation (3.3) requires one to maximize the mass-Q product at a given ω_{m}. In most commercial accelerometers, the Q-factor is relatively low, which demands large test masses for high resolution. In contrast, in the zipper cavity devices presented here, we use nano-tether suspension of a nano-gram test mass to yield high intrinsic mechanical Q-factors ($1-2\times10^6$), and strong thermo-optomechanical back-action to damp and cool the thermal motion of the test mass (Section 3.3.2.1).

3.1.2 Detector noise (a_{det})

The electronic detector noise is usually quantified by its noise-equivalent-power (NEP), which for the Newport 2117 detector and the transimpedance gain setting we use is on the order of 2.8 $\mathrm{pW}/\sqrt{\mathrm{Hz}}$. The optical noise power-spectral-density is then

$$S_{PP}^{NEP}(\omega) = \mathrm{NEP}^2. \tag{3.5}$$

Employing Eq. 3.13, the NEA corresponding to electronic detector noise can be derived as

$$a_{\mathrm{NEP}} = \frac{\omega_o}{(1-\mathrm{T_d}) Q_o g_{\mathrm{OM}} \eta_{\mathrm{in}} P_{\mathrm{in}}} \frac{1}{|\chi(\omega)|} \mathrm{NEP}. \tag{3.6}$$

Here, this is found to be $a_{\mathrm{NEP}} = 4.1$ $\mu\mathrm{g}/\sqrt{\mathrm{Hz}}$ for our system parameters.

3.1.3 Backaction noise (a_{add})

The extra noise, a_{add}, added by the optical field arises from optical noise that exerts a random force on the mechanical oscillator via radiation pressure. The optical noise arises from classical amplitude noise and from intrinsic shot noise. In the following, we consider only quantum back-action noise, a_{BA}, arising from optical shot noise. With $\hbar g_{\mathrm{OM}}$ being the force exerted per photon and for n_{cav} photons in the cavity, the random acceleration created by optomechanical back-action has a power spectral density of [86]

$$S_{aa}^{BA} = 2\frac{(\hbar g_{\mathrm{OM}})^2}{m_{\mathrm{eff}}^2} n_{\mathrm{cav}} \frac{4}{\kappa}, \tag{3.7}$$

resulting in a noise-equivalent acceleration of $a_{\mathrm{BA}} = \sqrt{S_{aa}^{BA}} = 5.6$ ng/$\sqrt{\mathrm{Hz}}$. Here, owing to the low quality factor of the optical cavity and the low mechanical frequency, the shot noise radiation pressure force is approximately white noise for frequencies of relevance near the mechanical frequency. Note also that we are using single-sided PSDs, hence double the value of the (approximately) symmetric double-sided PSD. This value is much smaller than the acceleration noise created by the other sources discussed previously. The frequency-dependent displacement noise created by quantum back-action is

$$S_{xx}^{BA}(\omega) = 2\left(\frac{2\hbar g_{\mathrm{OM}}}{m_{\mathrm{eff}}}\right)^2 \frac{n_{\mathrm{cav}}}{\kappa} |\chi(\omega)|^2. \tag{3.8}$$

On the peak of the mechanical resonance, this yields

$$S_{xx}^{BA}(\omega_m) = 2\left(\frac{2\hbar g_{\mathrm{OM}} Q_m}{m\omega_m^2}\right)^2 \frac{1-\sqrt{\mathrm{T_d}}}{\kappa^2} \frac{P_{\mathrm{in}}}{\hbar\omega_c}, \tag{3.9}$$

resulting in $\sqrt{S_{xx}^{BA}(\omega_m)} = 23$ fm/$\sqrt{\mathrm{Hz}}$ for the device and experimental conditions described in Figs. 3.4 and 3.8 ($P_{\mathrm{in}} = 116$ μW). This should be compared to the fundamental standard quantum limited displacement noise given by

$$S_{xx}^{SQL}(\omega) = S_{aa}^{SQL}|\chi(\omega)|^2 \tag{3.10}$$

$$= \frac{2\hbar\omega_m\gamma_m}{m}|\chi(\omega)|^2, \tag{3.11}$$

which on resonance has the simple form

$$S_{xx}^{SQL}(\omega_m) = x_{\mathrm{zp}}^2 \frac{4}{\gamma_m}. \tag{3.12}$$

For the device and experimental conditions described in Figs. 3.4 and 3.8, this yields an on-resonance SQL of $\sqrt{S_{xx}^{SQL}} = 2.8$ fm/$\sqrt{\mathrm{Hz}}$.

Note that although our back-action noise is above the SQL, our shot-noise imprecision is not below the SQL due to optical losses and the additional shot noise contribution from our balanced

detection scheme. Only if single-sided coupling is employed and no photons are lost in the optical path can detection at the standard quantum limit be achieved. Here, optical losses arise both from taper losses and the inherent two-sided nature of our coupling scheme via the fiber taper (see Section 1.2.3.1).

3.2 Device Design

Figure 3.3c shows a scanning-electron microscope image of the device studied here, with the test mass structure and nano-tethers highlighted in green. The fundamental in-plane mechanical mode of this structure is depicted in Fig. 3.3e and is measured to have a frequency of $f_{\rm m} = 27.5$ kHz, in good agreement with finite-element-method simulations from which we also extract an effective motional mass of $m_{\rm eff} = 10 \times 10^{-12}$ kg. The measured mechanical Q-factor is $Q_{\rm m} = 1.4 \times 10^6$ in vacuum (see Section 3.3.2). The region highlighted in pink corresponds to the zipper optical cavity used for monitoring test mass motion, a zoom-in of which can be seen in Figure 3.3d. The cavity consists of two patterned photonic crystal nanobeams, one attached to the test mass (bottom) and one anchored to the bulk (top). The device in Fig. 3.3c is designed to operate in the telecom band, with a measured optical mode resonance at $\lambda_{\rm o} = 1537$ nm and an optical Q-factor of $Q_{\rm o} = 9,500$. With the optical cavity field being largely confined to the slot between the nanobeams, the optical resonance frequency is sensitively coupled to relative motion of the nanobeams in the plane of the device (the $\hat{x}$-direction in Fig. 3.3c). A displacement of the test mass caused by an in-plane acceleration of the supporting microchip can then be read-out optically using the setup shown in Fig. 3.4a, where the optical transmission through the photonic crystal cavity is monitored via an evanescently-coupled fibre taper waveguide [87] resting on the rigid side of the cavity.

3.3 Characterization

Utilizing a narrow bandwidth (< 300 kHz) laser source, with laser frequency detuned to the red side of the cavity resonance, fluctuations of the resonance frequency due to motion of the test mass are translated linearly into amplitude-fluctuations of the transmitted laser light field (see inset in Fig. 3.4a, Section 1.2.3.2). A balanced detection scheme allows for efficient rejection of laser amplitude noise, yielding shot-noise limited detection for frequencies above ~ 1 kHz.

Figure 3.4b shows the electronic power spectral density (PSD) of the optically transduced signal obtained from the device in Fig. 3.3c. The cavity was driven with an incident laser power of $P_{\rm in} = 116$ μW, yielding an intracavity photon-number of ≈ 430. The two peaks around 27.5 kHz arise from thermal Brownian motion of the fundamental in- and out-of-plane mechanical eigenmodes of the suspended test mass. The transduced signal level of the fundamental in-plane resonance,

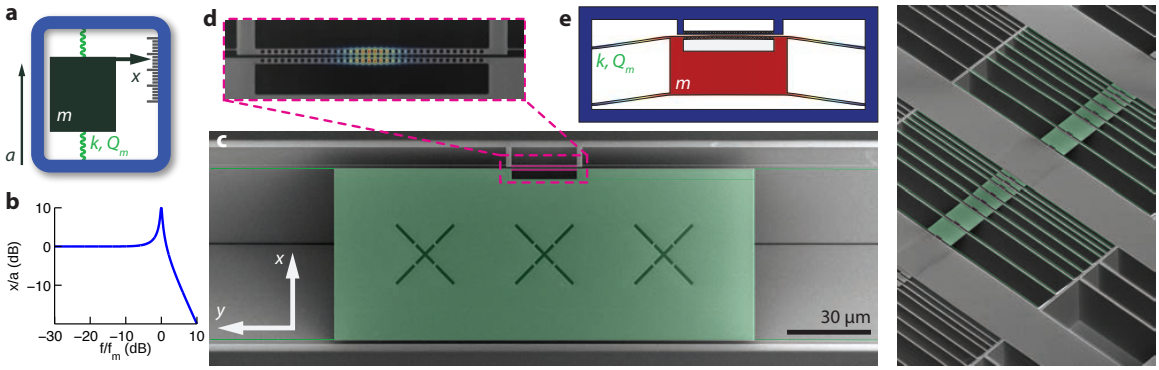

Figure 3.3: **Overview of accelerometer design.** (a) Canonical example of an accelerometer. When the device (blue frame) experiences a constant acceleration a, a test mass m undergoes a displacement of $x = ma/k$. (b) Frequency response $|\chi(\omega)|$ of an accelerometer on a log-log plot featuring a resonance at $f_{\mathrm{m}} = \sqrt{k/m}/2\pi$ with $Q_{\mathrm{m}} = 10$ and showing a mainly flat response for low frequencies. (c) False-coloured SEM-image of a typical optomechanical accelerometer. A test mass of size 150 μm $\times$ 60 μm $\times$ 400 nm (green) is suspended on highly stressed 150 nm wide and 560 μm long SiN nano-tethers, which allow for high oscillator frequencies ($>$ 27 kHz) and high mechanical Q-factors ($> 10^6$). On the upper edge of the test mass, we implement a zipper photonic crystal nanocavity (pink). The cross-shaped cuts on the test mass facilitate undercutting the device. (d) Zoom-in of the optical cavity region showing the magnitude of the electric field $|\mathbf{E}(\mathbf{r})|$ for the fundamental bonded mode of the zipper cavity. The top beam is mechanically anchored to the bulk SiN and the bottom beam is attached to the test mass. Relative motion of the beams changes the gap size and thereby shifts the cavity resonance frequency. (e) Schematic displacement profile (not to scale) of the fundamental in-plane mechanical mode used for acceleration sensing. The structure can be well described as a mass-on-a-spring system. (f) SEM-image of an array of devices with different test mass sizes.

the mode used for acceleration sensing, is consistent with an optomechanical coupling constant of $g_{\mathrm{OM}}/2\pi = 5.5$ GHz/nm. The dotted green line depicts the theoretical thermal noise background of this mode. The series of sharp features between zero frequency (DC) and 15 kHz are due to mechanical resonances of the anchored fibre-taper. The noise background level of Fig. 3.4b is dominated by photon shot-noise, an estimate of which is indicated by the red dotted line. The cyan dotted line in Fig. 3.4b corresponds to the electronic photodetector noise, and the purple dashed line represents the sum of all noise terms. The broad noise at lower frequencies arises from fibre taper motion and acoustic pick-up from the environment. The right-hand axis in Fig. 3.4b quantifies the optically transduced PSD in units of an equivalent transduced displacement amplitude of the fundamental in-plane mode of the test mass, showing a measured shot-noise-dominated displacement imprecision of 4 fm/$\sqrt{\mathrm{Hz}}$ (the estimated on-resonance quantum-back-action displacement noise is 23 fm/$\sqrt{\mathrm{Hz}}$, and the corresponding on-resonance SQL is 2.8 fm/$\sqrt{\mathrm{Hz}}$; see Section 3.1.3).

At this optical power the observed linewidth of the mechanical mode is $\approx$ 2 Hz, roughly 100 times larger than the low power linewidth. As modeled in Section 3.3.2.1, the measured mechanical damping is a result of radiation pressure dynamical back-action, enhanced by slow thermo-optical

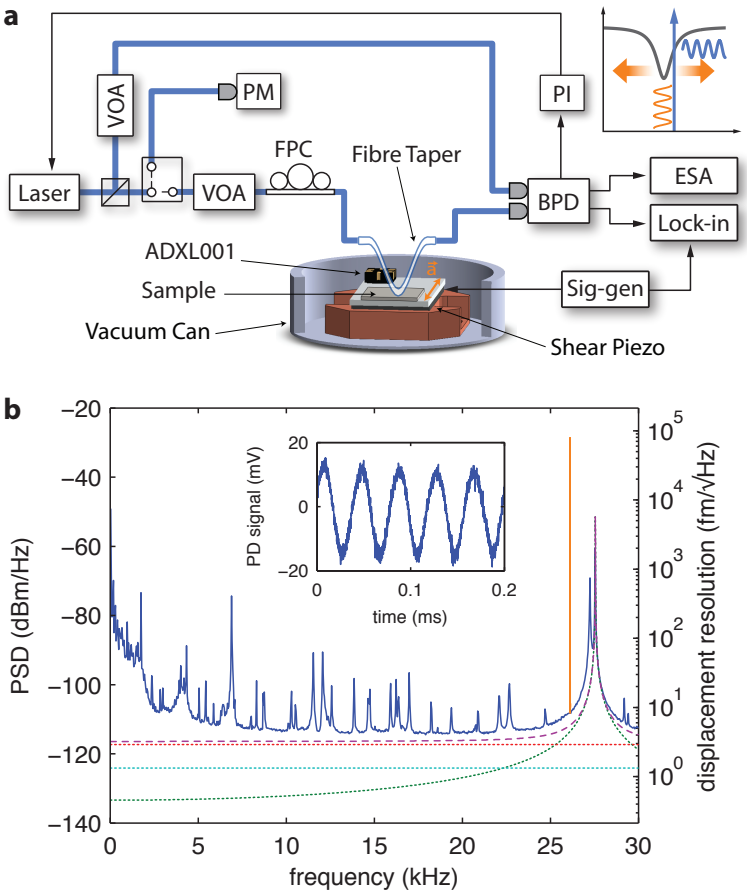

Figure 3.4: **Balanced Detection Experimental Setup.** (a) Laser light is split with a fibre beamsplitter, the signal arm is sent through a fibre polarization controller (FPC) and a fibre taper, which is coupled to the optical cavity, while the other arm is sent directly to a balanced photodetector (BPD). We use variable optical attenuators (VOA) in each arm to balance the powers, and a power meter (PM) for calibrations. The BPD signal is sent to a proportional-integral controller (PI) – locking the laser to the side of the optical resonance. The sample is mounted on a shake table comprised of a shear piezo which can be driven by a function generator. We monitor transduced accelerations using either an electronic spectrum analyzer (ESA) or a lock-in amplifier. (b), The left axes show an optical power spectral density (PSD) plot of the BPD signal showing mechanical modes at 27.5kHz (green). The right axis shows the equivalent displacement noise. The tone at 26 kHz (orange) is transduction of a tone applied to the shear piezo corresponding to an acceleration of 38.9 mg. The series of sharp features for lower frequencies arises from motion of the fibre taper. The dashed and dotted lines are theoretical noise levels for shot noise (red), detector noise (cyan), thermal noise (green), and the total of all noise contributions (purple). The inset is a time trace of the transduction of an applied acceleration of 35.6 mg at 25 kHz.

tuning of the cavity, which provides the necessary phase-lag for efficient velocity damping. Damping of the mechanical resonance is typically used to reduce the ringing transient response of the sensor when subjected to a shock input [88]. In contrast to conventional gas-damping employed in MEMS sensors [89], optomechanical back-action damping also cools the mechanical resonator [74]. The measured effective temperature of the fundamental in-plane mode of the test mass, as determined

from the area under the 27 kHz resonance line in Fig. 3.4b, is $T_{\rm eff} \approx 1$ K. This combination of damping and cooling keeps the ratio of $T_{\rm eff}/Q_{\rm m}$ fixed, and does not degrade the thermally-limited acceleration resolution of the sensor.

3.3.1 Optical Spectroscopy

The sample is optically coupled via a near-field probe consisting of a tapered optical fibre. The tapered fibre is brought in optical contact with the device using attocube nanopositioners. Aligned in parallel to the zipper nano-beams, the fibre taper is mechanically anchored on the struts attached to the rigid side of the zipper cavity. Launching light from a NewFocus Velocity tunable external-cavity diode laser into the fibre taper and monitoring the taper transmission then allows us to do resonant coherent spectroscopy of the cavity mode. Technical amplitude noise of the laser (~ 10 dB above the shot-noise level) is suppressed by a balanced detection scheme using a Newport 2117 balanced photodetector that features ~ 20 dB common-mode noise rejection.

Using Eqs. 1.31 and 1.25 it can be shown that the power in the mechanical sideband is

$$P_{\rm m}(\Delta = \kappa/2) = (1 - {\rm T_d})\,\frac{Q_{\rm o}}{\omega_{\rm o}} g_{\rm OM}\,\eta_{\rm in} P_{\rm in}\,x, \tag{3.13}$$

where $\omega_{\rm o}$ is the optical resonance frequency, the optical Q-factor is given by $Q_{\rm o} = \omega_{\rm o}/\kappa$, ${\rm T_d}$ is the relative cavity transmission dip on resonance, $\eta_{\rm in}$ accounts for the system detection efficiency, and the laser is half a linewidth detuned $\Delta = \kappa/2$.

This optical power is measured on a Newport 2117 balanced photo-detector with switchable transimpedance gain (in these experiments we use $g_{\rm ti} = 49{,}600$ V/W), generating a voltage output of $V_{\rm m} = g_{\rm ti} P_{\rm m}$. An electronic spectrum analyzer (ESA) calculates the electrical power spectral density of this optical sideband in units of $V_{\rm m}^2/Z$ with $Z = 50\ \Omega$ and expresses it in dBm/Hz. The conversion follows the relation

$${\rm PSD_{ESA}}(\omega) = 10 \cdot \log\left[\frac{\left(g_{\rm ti} P_{\rm m}(\omega)\right)^2}{Z} \cdot 1{,}000\right]. \tag{3.14}$$

Careful calibration of the parameters in Eq. (3.13) and Eq. (3.14), as well as the optical input power, allows one to calculate the optomechanical coupling $g_{\rm OM}$ from the magnitude of the (known) thermal Brownian motion noise of the mechanical oscillator. In the device presented here, we have ${\rm T_d} = 0.87$, $Q_{\rm o} = 9{,}500$, $\omega_o = 2\pi \times 195$ THz, and $\eta_{\rm in} = 0.57$. At low optical input power, where negligible back-action cooling is being performed on the fundamental in-plane mechanical mode of the suspended test mass and the mode's effective temperature is the temperature of the room temperature bath ($T \sim 300K$), the optomechanical coupling constant is estimated to be $g_{\rm OM}/2\pi = 5.5$ GHz/nm from the area under the Lorentzian centered at 27 kHz of the opti-

cally transduced displacement noise PSD. This corresponds to an optical displacement sensitivity of $P_{\rm m}/x = 3.7$ nW/pm for the fundamental in-plane mechanical mode of the suspended test mass. From electromagnetic finite-elements simulations we calculate $g_{\rm OM}/2\pi = 13.5$ GHz/nm for dimensions of the zipper cavity as measured with a scanning electron microscope, in good agreement with the measured value.

3.3.2 Determining Mechanical Quality

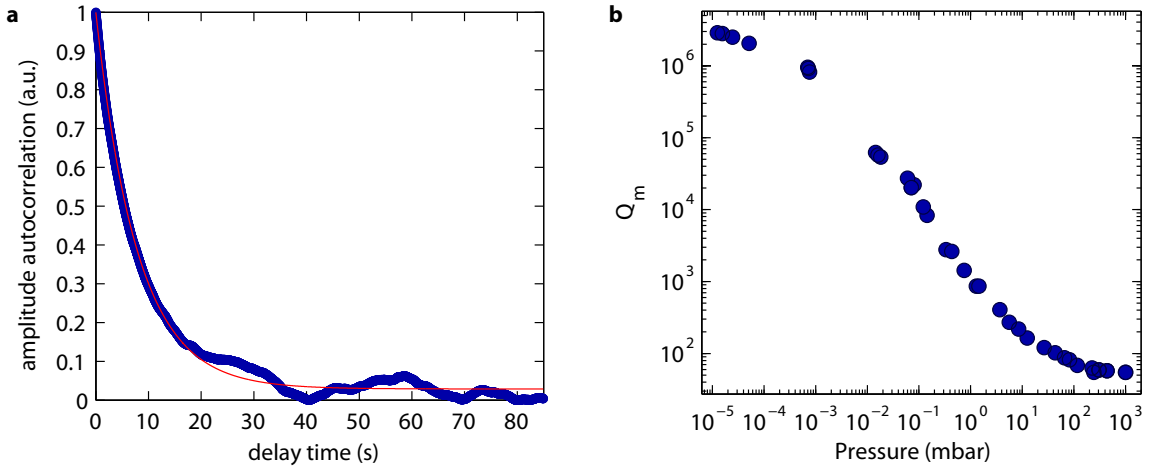

Figure 3.5: **Investigation of Mechanical Q-factors.** (a), Autocorrelation trace of the thermal noise driven mechanical amplitude. The signal was obtained from computing the autocorrelation of the slowly varying magnitude of the mechanical motion returned from a lock-in amplifier, using the experimental set up of Fig. 3.4. Fitting the trace with an exponential decay yields the time constant and thereby the mechanical Q-factor of the mode ($Q_{\rm m} = 1.4 \times 10^6$). (b), Pressure-dependence of the mechanical Q-factor of a control device with $m_{\rm eff} = 10^{-11}$ kg and 70 nano-tethers showing an increase from $Q_{\rm m} \approx 53$ at ambient pressure to $Q_{\rm m} \approx 2.5 \times 10^6$ in high vacuum.

The sub-Hz linewidths of our mechanical modes make establishing the quality factor from a measurement of the power spectral density on a spectrum analyzer infeasible because it requires a fractional stability of the frequency to greater than the quality factor, $\gg 1/Q_{\rm m} \approx 5 \times 10^{-7}$, over a period much longer than the decay time, $Q_{\rm m}/\omega_{\rm m} > 10$ s. However, since the system is driven by a Gaussian thermal noise process, the autocorrelation of the amplitude $\langle X(t)X(t+\tau)\rangle$ can be shown to decay as $\mathrm{e}^{-t/\tau}$ from which the quality factor can be obtained as $Q_{\rm m} = \tau\omega_{\rm m}$ (see Ref. [90]). The slowly-varying envelope of $\langle X(t)\rangle$ is obtained from the magnitude channel of a lock-in amplifier tuned to the mechanical resonance frequency with a bandwidth (≈ 100 Hz) much larger than the linewidth which ensures that small frequency diffusion does not affect the measurement of the envelope. To obtain the bare mechanical Q-factors the measurement is made at an optical power low enough to ensure there is no backaction. The autocorrelation is numerically computed and the decay is fit to an exponential curve with a constant (noise) offset. In Fig. 3.5a we show an autocorrelation trace

of the device calculated from ≈ 3000 s of data sampled at 100 Hz and fit it to find $\tau = 7.85$ s and for $\omega_{\rm m} = 2\pi \times 27.5$ kHz that $Q_{\rm m} = 1.4 \times 10^6$. For lower-$Q$ structures, it was confirmed that this technique agrees with a direct measurement of the linewidth from a spectrum analyzer.

Since gas damping severely limits the mechanical Q-factor of our oscillator, measurements were carried out in vacuum. Figure 3.5b shows pressure-dependent mechanical Q-factors using a device of equal mass as that presented in Fig. 3.5a, but with 70 tethers, resulting in an eigenfrequency of $\omega_{\rm m} = 2\pi \times 110$ kHz. We find that the device exhibits a Q-factor of 53 at ambient pressure, which strongly increases when reducing the pressure in the vacuum chamber. In particular, for pressures below 10^{-3} mbar – the regime in which we carried out the accelerometry measurements – we observe Q-factors above 10^6. These pressures are within range of modern packaging techniques for MEMS structures [91].

3.3.2.1 Thermo-Opto-Mechanical Cooling

The relatively small test mass makes the device studied in this work highly susceptible to optomechanical and thermo-optical back-action effects. Such dispersive couplings are well known to renormalize the frequency and damping rate of the mechanical oscillator. In particular, thermo-optical coupling that arises from a refractive index change of the material upon the absorption of cavity photons plays a significant role in these devices due to the efficient thermal isolation of our nano-tethered test-masses in vacuum.

In the parameter regime of our devices, purely optomechanical back-action is a relatively weak effect due to the low optical Q-factor. For the parameters given above and for a pump laser with an incident power of $P_{\rm in} = 116$ μW half a linewidth red-detuned from the cavity resonance, optomechanical back-action alone predicts a frequency shift of merely $\omega_{\rm m}' - \omega_{\rm m} = -2\pi \times 35.9$ Hz and a damping factor of $\gamma'/\gamma = 1.01$.

The Supplementary Information of Ref. [72] gives a detailed derivation of the renormalized oscillator frequency and damping rate under the influence of optomechanical and thermo-optical coupling. The system of differential equations that describes the time evolution of the intra-cavity field a, the oscillator position x, and the cavity temperature shift ΔT is given by

$$\dot{a} = -\left[i\Delta - (g_{\rm OM}x + g_{\rm th}\Delta T)\right] a - \frac{\kappa}{2}a + \sqrt{\frac{\kappa_e}{2}}a_{\rm in} \tag{3.15}$$

$$\ddot{x} = -\gamma\dot{x} - \omega_{\rm m}^2 x - \frac{\hbar g_{\rm OM}}{m_{\rm eff}}\left|a\right|^2 \tag{3.16}$$

$$\dot{\Delta T} = -\gamma_{\rm th}\Delta T + \kappa_{\rm abs}c_{\rm th}\hbar\omega_c\left|a\right|^2, \tag{3.17}$$

where $g_{\rm th} = -({\rm d}n/{\rm d}T)(\omega_c/n)$ is the thermo-optical tuning coefficient, ${\rm d}n/{\rm d}T$ is the thermo-optic coefficient of the material, $\kappa_{\rm abs}$ is the optical loss rate due to material absorption, $c_{\rm th}$ is the thermal

heat capacity, and $\gamma_{\rm th}$ is the decay rate of the temperature. Linearizing these equations yields the static solutions

$$a_0 = \sqrt{\frac{\kappa_e}{2}}\frac{1}{i\Delta' + \kappa/2}, \quad x_0 = \frac{\hbar g_{\rm OM}}{m_{\rm eff}\omega_{\rm m}^2}\left|a_0\right|^2, \quad \Delta T_0 = \frac{\kappa_{\rm abs}}{\gamma_{\rm th}} c_{\rm th}\hbar\omega_c\left|a_0\right|^2, \tag{3.18}$$

with the renormalized detuning $\Delta' = \Delta - g_{\rm OM}x_0 - g_{\rm th}\Delta T_0$ arising from the static optomechanical and thermo-optical shift. Using a perturbation ansatz $x(t) = x_0 + \epsilon\cos(\omega_{\rm m}t)$, one arrives after some algebraic manipulation at a modified harmonic oscillator equation for x with a renormalized frequency $\omega'_{\rm m}$ and damping rate γ' given by

$$\omega'^2_{\rm m} = \omega_{\rm m}^2 \quad - \quad \frac{\hbar\omega_c n_{\rm c} g_{\rm OM}^2}{\omega_c m_{\rm eff}}\,{\rm Im}\left[g(\omega_{\rm m})\right], \tag{3.19}$$

$$\gamma' = \gamma \quad + \quad \frac{\hbar\omega_c n_{\rm c} g_{\rm OM}^2}{\omega_{\rm m}\omega_c m_{\rm eff}}\,{\rm Re}\left[g(\omega_{\rm m})\right], \tag{3.20}$$

where the transfer function $g(\omega)$ is defined as

$$g(\omega) = f\frac{1 + f'^* f^*}{|1 + f'f|^2} \tag{3.21}$$

with

$$f(\omega) = \frac{1}{i(\omega + \Delta') + \kappa/2} - \frac{1}{i(\omega - \Delta') + \kappa/2} \tag{3.22}$$

and

$$f'(\omega) = -i\frac{\Delta_{\rm th}\gamma_{\rm th}}{i\omega + \gamma_{\rm th}}, \tag{3.23}$$

and $\Delta_{\rm th} = g_{\rm th}\Delta T_0$ is the static thermo-optical shift of the cavity resonance frequency. In the sideband unresolved regime where $\omega_{\rm m} \ll \kappa$ and for thermal decay rates $\gamma_{\rm th}$ smaller than the mechanical frequency, an approximation of $g(\omega)$ yields

$$\omega'^2 = \omega^2 \quad + \quad \frac{2\hbar n_{\rm c} g_{\rm OM}^2}{m_{\rm eff}}\frac{\Delta'}{\Delta'^2 + \kappa^2/4}\left[\frac{1+W}{1+s}\right], \tag{3.24}$$

$$\gamma' = \gamma \quad + \quad \frac{2\hbar n_{\rm c} g_{\rm OM}^2}{m_{\rm eff}}\frac{\kappa\Delta'}{(\Delta'^2 + \kappa^2/4)^2}\left[\frac{1+V}{1+s}\right], \tag{3.25}$$

with the correction factors

$$W \quad = \quad -\left(\frac{2\Delta_{\rm th}}{\kappa}\right)\left(\frac{\gamma_{\rm th}}{\omega_{\rm m}}\right)^2\left(\frac{\kappa\Delta'}{\Delta'^2 + \kappa^2/4}\right), \tag{3.26}$$

$$V \quad = \quad \left(\frac{2\Delta_{\rm th}}{\kappa}\right)\left(\frac{\gamma_{\rm th}}{\omega_{\rm m}}\right)^2\left(\frac{\Delta'}{\gamma_{\rm th}}\right) \tag{3.27}$$

$$\tag{3.28}$$

and the saturation parameter

$$s = \left(\frac{2\gamma_{\rm th}\Delta_{\rm th}\hbar\omega_c n_{\rm c}}{\omega_{\rm m}} \frac{\Delta'}{\Delta'^2 + \kappa^2/4} \right)^2 \left(1 + \frac{1}{\Delta_{\rm th}} \left(\frac{\Delta'^2 + \kappa^2/4}{\Delta'^2} - \frac{\omega_{\rm m}^2 \kappa}{\Delta' \gamma_{\rm th}} \right) \right). \tag{3.29}$$

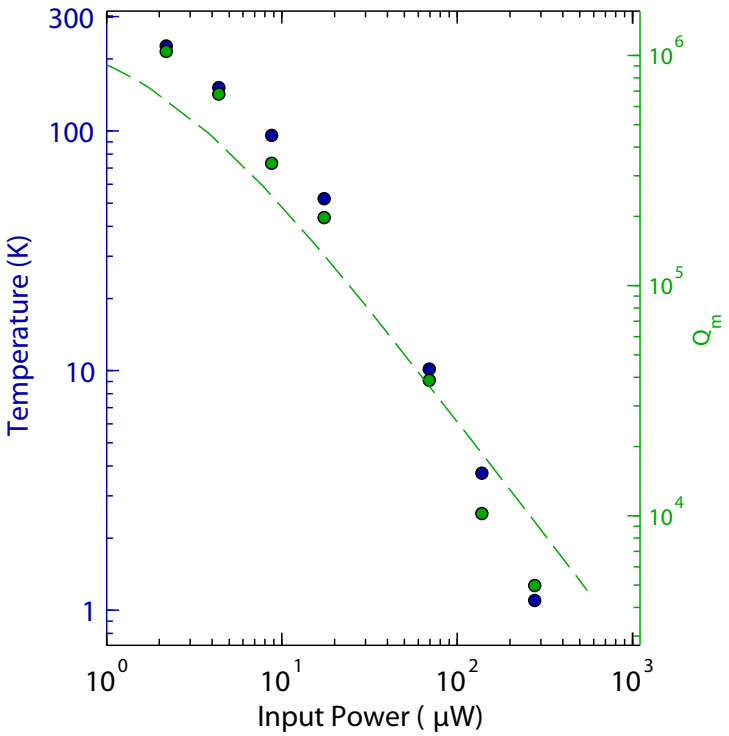

Figure 3.6: **Demonstration of Thermo-Optomechanical Damping and Cooling.** The green bullets show measured Q-factors of the mechanical mode as a function of the optical power, yielding thermo-optomechanical damping by a factor of ≈ 280. The blue bullets show the corresponding optical power in the sideband generated by mechanical motion, proportional to the effective mode temperature. We observe cooling to $T_{\rm eff} \approx 1$ K. The dashed green curve corresponds to a theoretical model that includes optomechanical and thermo-optical back-action.

In order to study the influence of thermo-optical back-action, we measured the Q-factor of the mechanical mode as a function of the optical power launched into the cavity, shown as the green bullets in Fig. 3.6. When increasing the optical power to $P_{\rm in} \approx 300$ μW, which corresponds to an intracavity photon number of $n_{\rm c} \approx 1,100$, the Q-factor shows strong damping and is reduced by a factor of ≈ 200. Similarly, we measure the area of the mechanical resonance peak from the optically transduced thermal noise PSD for a series of optical powers, and plot the inferred effective mode temperature as blue bullets in Fig. 3.6. Clear in Fig. 3.6 is that the effective mode temperature drops along with the measured mechanical Q-factor.

The observed mechanical damping is much larger than the value predicted by pure optomechanical back-action and can be explained when including thermo-optical tuning. The green line

in Fig. 3.6 was obtained by calculating the modified Q-factor $Q'_{\rm m} = \omega_{\rm m}/\gamma'$ using eq. (3.20) with $\Delta_{\rm th} = -0.05\kappa$ and $\gamma_{\rm th} = 2\pi \times 9.2$ kHz. The latter value is in good agreement with the one from Ref. [72] ($\gamma_{\rm th} = 2\pi \times 10$ kHz), which suggests that the time constant of thermo-optical tuning is dominated by heat-flow from the zipper cavity region to the reservoir formed by the test-mass (or the bulk in the case of Ref. [72], respectively).

The obtained values for $\Delta_{\rm th}$ and $\gamma_{\rm th}$ result in correction factors of $V = 12{,}400$, $W = -0.011$, and a saturation parameter of $s \approx 3 \times 10^{-36}$. Accordingly, we expect a significant thermo-optical correction to damping, as observed, but only a minor modification of the optomechanical spring: $\omega' - \omega = 2\pi \times 36.2$ Hz for the pump power used in the experiment. Indeed, we observed a frequency shift of 101 Hz, in reasonable agreement with the theoretical value.

3.3.3 Calibration

In order to carefully calibrate the accelerometric performance of the device, the sample is mounted onto a shake table driven by a shear piezo actuator. Applying a sinusoidal voltage to the piezo results in a harmonic acceleration $a(\omega)$, and thereby a modulation of the transmitted optical power.

The narrow tone at 26 kHz in Fig. 3.4b (orange) arises from an applied rms-acceleration of $a_{\rm rms} = 38.9$ mg, calibrated using two commercial accelerometers mounted on the shake table. From the signal-to-noise-ratio of this calibration tone we estimate $a_{\rm th} = 2.0\ \mu{\rm g}/\sqrt{\rm Hz}$, comparable to the theoretical value of $a_{\rm th} = 1.4\ \mu{\rm g}/\sqrt{\rm Hz}$. For a driving tone at 10 kHz, we measure $a_{\rm min} \approx 10\ \mu{\rm g}/\sqrt{\rm Hz}$, limited in this case by photon shot noise.

3.3.4 Linear Dynamic Range

A key requirement for any inertial sensor is linear response over a reasonable range. To check the linearity of the response of the accelerometer presented in Fig. 3.4b, we varied the amplitude of a sinusoidal signal sent to the shear piezo at 9.92 kHz and recorded the voltage corresponding to the peak height of the transduced modulation tone — shown in blue bullets in Fig. 3.7. The sensor behaves linearly over a dynamic range of 41 dB, with the tone vanishing into the shot noise floor for an applied acceleration of $\approx 10\ \mu$g at a resolution bandwidth of 1 Hz. The green bullets in Fig. 3.7 show data from a different device with similar geometry but lower mechanical Q-factor (with relevant parameters $g_{\rm OM}/2\pi = 6.36$ GHz/nm, $\omega_{\rm m}/2\pi = 27.5$ kHz, $\lambda_o = 1539$ nm, $Q_{\rm o} = 3000$, and $Q_{\rm m} = 13{,}000$), which exhibits a linear response over 49 dB. This particular measurement was limited by the maximum output voltage of the function generator. Ultimately, however, the linear dynamic range ends when motion of the test mass shifts the optical resonance by a magnitude comparable to the optical cavity linewidth. For drive frequencies substantially below the resonance frequency, an acceleration of ~ 30 g moves the cavity resonance over one linewidth, κ. Thus we predict that the

full linear range of the sensor presented in Fig. 3.4b should be ≈ 60 dB if we had shaken it to higher accelerations. For this device, we stopped at 0.1 g for fear of breaking/harming the device. A fear that was, in retrospect, unfounded.

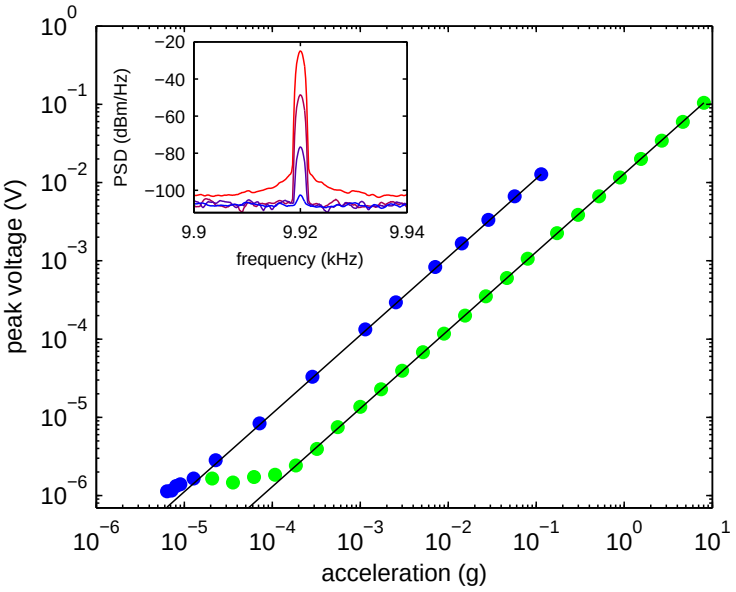

Figure 3.7: **Demonstration of Linear Dynamic Range.** While varying the amplitude of the acceleration applied with the calibrated shake table at 9.92 kHz, we measure the optical signal transduced via the mechanical mode. The blue bullets show the transduced signal of the device presented in the text using the voltage corresponding to the peak height of the modulation tone on the ESA spectrum, which exhibits linear response over 40 dB. The inset shows the corresponding PSD spectra from the ESA for modulation tones between 0.1 g and 12.8 μg, taken at a resolution bandwidth of 1 Hz. The green bullets show data obtained from a different device (with relevant parameters $g_{\rm OM}/2\pi$ = 6.36 GHz/nm, $\omega_{\rm m}/2\pi$ = 27.5 kHz, λ_o = 1539 nm, $Q_{\rm o}$ = 3000, and $Q_{\rm m}$ = 13,000) with a larger thermal noise background but very similar optomechanical coupling using the lock-in scheme depicted in Fig. 3.4, which exhibits linear response over 49 dB, limited by the maximum voltage output of our function generator, which corresponds to an acceleration of 8 g. The black lines are linear fits to the data.

3.3.4.1 Acceleration Sensitivity Measurement

For applying AC accelerations to our device, we constructed a shake table comprising a sample holder plate glued on a shear piezo actuator. Applying a sinusoidal AC-voltage to the piezo creates a displacement, $x_0 \sin(\omega_d t)$, which results in an applied acceleration of $-x_0\omega_d^2 \sin(\omega_d t)$. For calibration of the shake table assembly, we use commercial accelerometers from Analog Devices of 5.5 kHz (ADXL103) and 22 kHz (ADXL001) bandwidth. In order to measure the frequency response of our optomechanical accelerometer, we apply a constant-voltage drive to the piezo and tune its frequency, while measuring the photodetector output on a lock-in amplifier. After normalizing for the ω_d-dependence of the applied acceleration, this yields the frequency-dependent sensitivity of

the device. Normalizing an optical noise PSD then allows us to calibrate the noise-floor of the accelerometer in terms of a noise-equivalent acceleration.

3.3.5 Resolution

Figure 3.8a shows the demodulated photodiode signal normalized to the applied acceleration as a function of drive frequency, corresponding to the frequency dependent acceleration sensitivity of the zipper cavity (the inset of Fig. 3.8a shows data from the commercial accelerometers used to calibrate the applied acceleration). The dashed red line is the theoretical calculation of the sensitivity without fit parameters and shows excellent agreement. The sharp Fano-shaped features near the lower frequencies can again be attributed to mechanical resonances of the fibre-taper waveguide. The broad region of apparent higher-sensitivity around 15 kHz is due to an underestimate of the applied acceleration arising from an acoustic resonance of the shake table.

The calibrated frequency-dependent NEA, shown in Fig. 3.8b, is obtained by normalizing the ESA noise spectrum (Fig. 3.4b) by the sensitivity curve (Fig. 3.8a). Between 25–30 kHz the resolution is limited by the thermal noise of the oscillator, while from 5–25 kHz shot-noise limits the resolution to $\approx 10\ \mu\mathrm{g}/\sqrt{\mathrm{Hz}}$. For frequencies lower than 5 kHz, motion of the fibre-taper waveguide and the environment contribute extra noise. The sharp Fano-shaped feature at 27 kHz arises from interference with the fundamental out-of-plane mode of the test mass. The dashed red curve corresponds to a theoretical estimate of the NEA which shows good agreement. The dashed green line is the fundamental thermal sensing limit (a_{th}).

3.4 Breaking $1\mu g$

The device platform demonstrated here straightforwardly allows for further reduction of the NEA. For instance, a_{th} can be reduced further by increasing the test mass m. In a preliminary study, we have fabricated a series of devices with test masses ranging from 100×10^{-15} kg to 35×10^{-12} kg and recorded their mechanical frequency and Q-factor. Figure 3.9a depicts the calculated a_{th} versus the mechanical frequency of the studied devices, which roughly scales with $a_{\mathrm{th}} \propto \omega_{\mathrm{m}}^{3/2}$ (green line). Adding mass alone also results in a reduction of the sensor bandwidth; however, by scaling the number of nano-tether suspensions with the test mass size (see Figures 3.9b and c) the bandwidth can be kept constant. Moreover, as shown in the inset of Fig. 3.9a, we have found that adding nano-tethers does not result in a degradation of the mechanical Q-factor. Simultaneously scaling the width of the test mass and the number of nano-tethers by a factor of 100 from the device shown in Fig. 3.3c to a mass of $m_{\mathrm{eff}} = 10^{-9}$ kg should reduce the thermal NEA to $\sim 150\ \mathrm{ng}/\sqrt{\mathrm{Hz}}$ while maintaining a sensor bandwidth of 25 kHz. Critically, for $g_{\mathrm{OM}}/2\pi = 100$ GHz/nm as measured in previous zipper cavity structures [72], the optical input power required to reach this resolution across

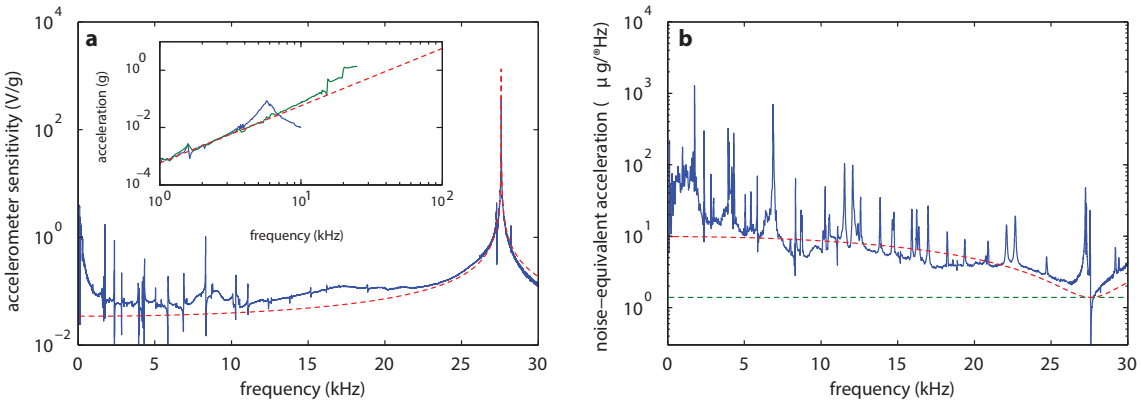

Figure 3.8: **Frequency-Dependence of Sensitivity and Resolution.** (a) Sensitivity curve as function of frequency. This curve is obtained by driving the shear piezo with a sinusoidal voltage and measuring the amplitude of the resulting voltage modulation of the BPD signal using a lock-in amplifier. The sensitivity curve is obtained by sweeping the frequency and normalising the lock-in output by the applied acceleration. The dashed red line corresponds to the theoretical expectation for the sensitivity without fit parameters. The inset shows data from commercial accelerometers also attached to the shake table (blue and green curves), which are used for calibrating the applied acceleration. The dashed line is an ω^2 fit and extrapolation to frequencies beyond the mechanical resonances of the commercial accelerometers. (b) Frequency-dependent noise-equivalent acceleration (NEA) of the device quantifying its broadband-resolution. The plot is obtained by taking the PSD in Fig. 3.4b and normalising it by the sensitivity curve in (a). The dashed red line depicts the theoretical expectation for the NEA. The green dashed curve corresponds to the thermal noise $a_{\rm th}$, which sets the fundamental sensing limit of the device.

the entire sensor bandwidth is still sub-milliwatt ($\sim 850\ \mu$W).

3.5 Summary

With a demonstrated acceleration resolution on the order of a few $\mu g/\sqrt{\rm Hz}$ and a bandwidth above 25 kHz, the zipper cavity device presented here shows performance metrics orders of magnitude better than other optical accelerometers [68, 69] and comparable to the best commercial sensors [92]. These devices, formed from a silicon chip, also allow for the integration of electrostatic tuning-capacitors [93], fibre-coupled on-chip waveguides [70], and on-chip electronics, all of which enables convenient, small form-factor packaging, and eliminates the need for expensive tunable lasers. In addition, nanoscale optomechanical cavities such as the zipper cavity studied here offer the unique resource of strong radiation-pressure back-action. The optical spring effect, for example, allows for dynamic tuning of the mechanical resonance frequency, which can increase the low-frequency displacement response (inverse quadratically with frequency) and decrease thermal noise (with the square root of frequency). Similar zipper cavity devices have shown low power (sub-mW) optical tuning of the mechanical resonance frequency over 10's of MHz ($> 200\%$ of $\omega_{\rm m}$) into a regime where the mechanical structure is almost entirely suspended by the optical field [72]. Also, as

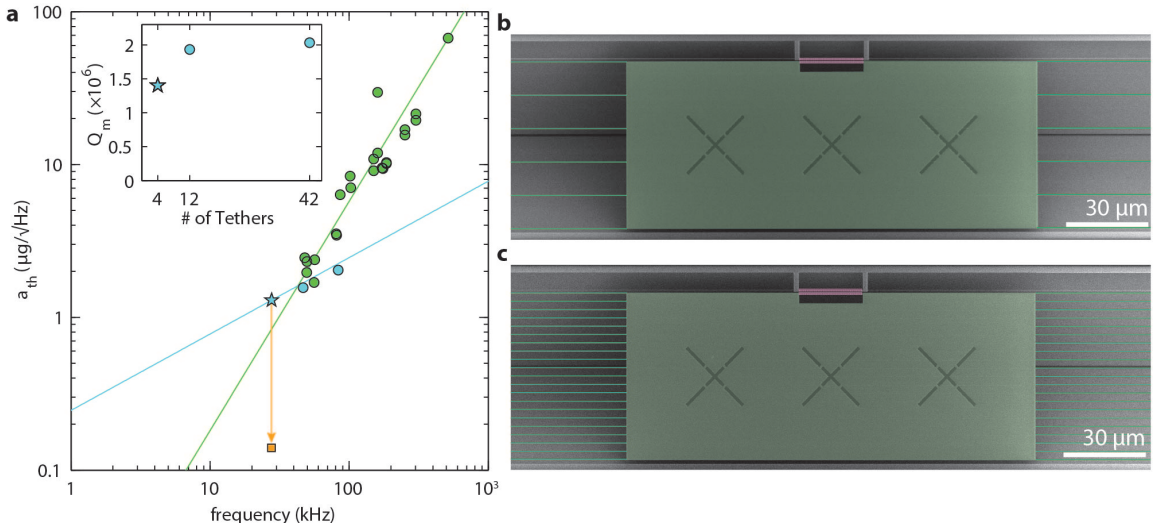

Figure 3.9: **Independent Tuning of Bandwidth and Resolution.** (a) Calculated thermal acceleration noise density of measured devices (green and cyan data points). The starred device is presented in the text. The green line is that traversed for adding mass with fixed $Q_{\rm m}$ and k, while the cyan line is obtained for varying k while keeping $Q_{\rm m}$ and $m_{\rm eff}$ fixed. Varying both m and k allows for independent control of bandwidth and resolution, for example along the orange line, where k/m is constant. The orange square represents theoretical device performance for 100 times increased test mass as compared to that in the text. The inset shows $Q_{\rm m}$ for the devices corresponding to the cyan circles in **a** versus number of nano-tethers attached to the test mass. Changing the number of nano-tethers from $4 \rightarrow 42$ does not degrade $Q_{\rm m}$, and allows for a three-fold increase in bandwidth with only slight increase in thermal acceleration noise. (b–c) False-colour SEM images of devices with 12 (42) nano-tethers and $f_{\rm m} = 46$ kHz (83 kHz), while maintaining high quality factors, $Q_{\rm m}$, of 1.9×10^6 (2×10^6).

demonstrated here, back-action cooling provides a resource to damp the response of the oscillator without compromising the resolution. Combining all of these attributes should allow not only for a new class of chip-scale accelerometers, but other precision displacement-based sensors of, for example, mass, force, and rotation.

Chapter 4

Room-Temperature Feedback Cooling of a Mechanical Oscillator [94]

Optical measurement of the motion of a 940 kHz resonant mode of a silicon nitride nanobeam optomechanical resonator is demonstrated with a read-out noise (imprecision) reaching 37 dB below that of the zero-point fluctuation noise of the resonator (the standard quantum limit). Via intensity modulation of the optical probe laser, radiation pressure feedback is used to cool and damp the mechanical mode from an initial room temperature occupancy of $\bar{n}_{\rm b} = 6.5 \times 10^6$ ($T_{\rm b} = 295K$) down to a phonon occupation of $\langle n \rangle = 66$ representing a mode temperature of $T_{\rm m} = 3$ mK. The five decades of cooling is enabled by the system's large single-photon cooperativity ($C_1 = 4$) and high quantum efficiency of optical detection of motion ($\eta_t = 0.27$).

4.1 Introduction

Cavity-optomechanical systems utilize multi-pass scattering of light within a cavity to perform sensitive measurement of mechanical motion, with applications ranging from inertial microsensors [95, 96] to transducers for interfacing disparate quantum systems [97, 98]. In this work, we integrate a silicon nitride nanostring mechanical resonator of motional mass $m_{\rm eff} = 90 \times 10^{-15}$ kg and frequency $\omega_{\rm m}/2\pi = 940$ kHz, with a 1.5 μm wavelength photonic crystal nanocavity. The strength of the optomechanical coupling in this structure is characterized by a per photon measurement rate of the nanostring motion, which is four times that of its intrinsic damping rate. Combined with an overall optical detection efficiency of $\eta_t = 0.27$, this enables a measurement imprecision which reaches 37 dB below that of the zero-point fluctuation noise of the bare mechanical resonator. Active cancellation of the mechanical thermal motion through feedback on the read-out laser's intensity realizes cooling from room temperature down to a phonon occupancy of $\langle n \rangle = 66 \pm 10$. This chip-scale microresonator, operating in a room temperature environment yet close to its quantum ground-state

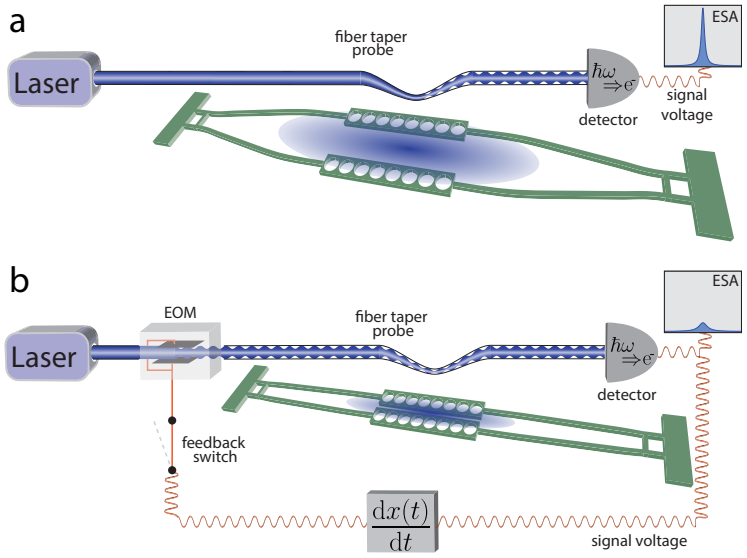

Figure 4.1: **Pictorial Description of Feedback Experiment.** (a) Laser emits into an optical fiber which narrows into a fiber taper, where it evanescently couples into the photonic crystal of an optomechanical device (green). This laser light light is modulated by the motion of the mechanical resonator and converted to a signal voltage (orange) at the detector. This mechanical signal appears as a lorentzian peak on an electronic spectrum analyzer (ESA). (b) Same setup as (a) with the addition of a feedback loop where the detected signal is sent through a derivative circuit and then drives an electro-optic-modulator (EOM), which modulates the amplitude of the incident laser light. If the feedback is sufficiently fast, the incoming modulated laser light provides velocity-damping of the mechanical motion via the radiation pressure force. This is observed as a smaller detected signal on the ESA.

of motion, has a thermal-noise-limited force sensitivity of 125 aN/Hz$^{1/2}$, a bandwidth of 200 kHz around resonance, and a linear dynamic range at one second integration time of greater than 60 dB.

Resolved-sideband radiation pressure cooling has been recently demonstrated [11, 13] as an effective means to cool a targeted mechanical mode close to its quantum mechanical ground-state of motion. This technique, sharing similar physics to the resolved-sideband cooling of trapped ions [99], requires spectral filtering of the upper (anti-Stokes) motional sideband from the lower (Stokes) motional sideband by a high-Q cavity in which the cavity linewidth (κ) is narrower than the mechanical resonances frequency ($\omega_{\rm m}$). Demonstrations to date of resolved-sideband cooling of micro- and nanomechanical resonators into their quantum ground-state have all required cryogenic pre-cooling. In the microwave regime [13], bath temperatures $T_{\rm b} \lesssim 100$ mK have been utilized to enable high-Q superconducting cavities, whereas in the optical domain [11] more modest bath temperatures of 1-20 K in a helium cryostat have been employed to, among other things, reduce intrinsic mechanical damping and thermorefractive noise of the optical cavity.

An alternative method of radiation pressure cooling, one which is less restrictive and more amenable to lower frequency mechanical resonators, relies on low noise optical read-out of mechan-

ical displacement combined with active feedback of the optical probe intensity [74, 100]. Previous optomechanical feedback cooling experiments [101–105] have demonstrated the ability to cool a wide range of mechanical resonators, from suspended large scale kilogram mass mirrors [105] to optically leviated microspheres [102, 103]. In Fig. 4.1 we sketch the basic elements of a radiation pressure feedback cooling experiment as performed in this work.

The method of cooling by derivative feedback can be understood by considering the harmonic oscillator equation of motion with an additional feedback force term:

$$\ddot{x} + \gamma_i \dot{x} + \omega_{\rm m}^2 x = \frac{F_{\rm th}}{m_{\rm eff}} - g\gamma_i \dot{x}_{\rm m} e^{i\theta_{\rm fb}}, \tag{4.1}$$

where $x(t)$ is the amplitude of motion of the mechanical resonator, $m_{\rm eff}$ is the motional mass of the mechanical resonator, $\omega_{\rm m}$ is the mechanical resonance frequency, γ_i the intrinsic mechanical energy decay rate of the resonator, and $F_{\rm th}$ is the classical thermal noise force. The final term on the right-hand side of Eq. (4.1) is the feedback forcing term, where g is the unitless gain of the feedback loop, $\theta_{\rm fb}$ the phase of the feedback, $x_{\rm m}(t) = x(t) + x_{\rm n}(t)$ is the estimated resonator's amplitude from measurement, and $x_{\rm n}(t)$ is the noise of the amplitude measurement of the resonator. As detailed in Section 4.2, for $\theta_{\rm fb} = 0$ and when $x_{\rm n}(t)$ is negligible, this term leads to viscous damping and cooling of the mechanical resonance, with the mechanical Q-factor and phonon occupancy scaling as $Q_{\rm m} = Q_{\rm m,i}/(1+g)$ and $\langle n \rangle = \bar{n}_{\rm b}/(1+g)$, respectively. Here, $Q_{\rm m,i}$ is the intrinsic mechanical quality factor due to the coupling rate γ_i to the resonator's thermal environment, $\bar{n}_{\rm b}$ is the thermal bath occupancy at $\omega_{\rm m}$, and $\langle n \rangle$ is the resulting average phonon occupancy of the mechanical mode. For the room temperature measurements of this work, $\bar{n}_{\rm b} \approx k_{\rm B} T_{\rm b}/\hbar\omega_{\rm m} \approx 6.5 \times 10^6$, where $T_{\rm b} \approx 295$ K is the bath temperature, $k_{\rm B}$ is Boltzmann's constant, and $\hbar$ is Planck's constant over 2π.

4.2 General Feedback Cooling

We start with the equation of motion for a simple harmonic oscillator, with a general forcing term on the right-hand-side determined by $\mathcal{F}(t)$. Later in the derivation we'll consider the specifc case of ideal derivative feedback ($\mathcal{F}(t) * x = \dot{x}(t)$):

$$m_{\rm eff}\ddot{x} + m_{\rm eff}\gamma_{\rm i}\dot{x} + m_{\rm eff}\omega_{\rm m}^2 x = F_{\rm th} - g m_{\rm eff}\gamma_{\rm i}\omega_{\rm m} \left(\mathcal{F}(t) * \left(x\left(t\right) + x_{\rm n}\left(t\right)\right)\right) e^{i\theta_{\rm fb}}, \tag{4.2}$$

$$\ddot{x} + \gamma_{\rm i}\dot{x} + \omega_{\rm m}^2 x = F_{\rm th}/m_{\rm eff} - g\gamma_{\rm i}\omega_{\rm m} \left(\mathcal{F}(t) * \left(x(t) + x_{\rm n}(t)\right)\right) e^{i\theta_{\rm fb}}. \tag{4.3}$$

Here x is the actual position coordinate of the resonator, $x_{\rm n}$ is the measurement noise of the position coordinate of the resonator, $m_{\rm eff}$ is the motional mass, $\gamma_{\rm i}$ is the intrinsic mechanical angular damping rate, $\omega_{\rm m}$ is the intrinsic mechanical angular frequency, $F_{\rm th}$ is the stochastic thermal force, and $\theta_{\rm fb}$

is an overall phase of the feedback force. Because our experimental results are not limited by our measurement noise floor, we will drop the discussion of $x_{\mathrm{n}}(t)$; its effects can be seen when the cooled mechanical motion approaches the noise floor [104]. We can Fourier transform Eq. (4.3) into

$$-\omega^2 x(\omega) + i\gamma_{\mathrm{i}}\omega x(\omega) + \omega_{\mathrm{m}}^2 x(\omega) = F_{\mathrm{th}}(\omega)/m_{\mathrm{eff}} - g\gamma_{\mathrm{i}}\omega_{\mathrm{m}}\left(\mathcal{F}(\omega)x(\omega)\right)e^{i\theta_{\mathrm{fb}}}. \tag{4.4}$$

Solving Eq. 4.4 for $x(\omega)$ leads to

$$x(\omega) = \frac{F_{\mathrm{th}}(\omega)/m_{\mathrm{eff}}}{(\omega_{\mathrm{m}}^2 - \omega^2) + i\gamma_{\mathrm{i}}\omega + g\gamma_{\mathrm{i}}\omega_{\mathrm{m}}\mathcal{F}(\omega)e^{i\theta_{\mathrm{fb}}}}. \tag{4.5}$$

In general, the feedback function $\mathcal{F}(\omega)$ is a complex value (magnitude and phase) and we also include an overall phase term in the $e^{i\theta_{\mathrm{fb}}}$. We can separate this into its two components to see how this feedback modifies the dynamics:

$$x(\omega) = \frac{F_{\mathrm{th}}(\omega)/m_{\mathrm{eff}}}{(\omega_{\mathrm{m}}^2 - \omega^2) + g\gamma_{\mathrm{i}}\omega_{\mathrm{m}}\mathrm{Re}\left[\mathcal{F}(\omega)e^{i\theta_{\mathrm{fb}}}\right] + i\left(\gamma_{\mathrm{i}}\omega + g\gamma_{\mathrm{i}}\omega_{\mathrm{m}}\mathrm{Im}\left[\mathcal{F}(\omega)e^{i\theta_{\mathrm{fb}}}\right]\right)}. \tag{4.6}$$

And we can now write the modifications to the frequency and damping factor:

$$\begin{aligned}
\omega_{\mathrm{m}} &= \sqrt{\omega_{\mathrm{m}}^2 + g\gamma_{\mathrm{i}}\omega_{\mathrm{m}}\mathrm{Re}\left[\mathcal{F}\left(\omega\right)e^{i\theta_{\mathrm{fb}}}\right]}, \\
&\approx \omega_{\mathrm{m}} + g\frac{1}{2}\gamma_{\mathrm{i}}\mathrm{Re}\left[\mathcal{F}\left(\omega\right)e^{i\theta_{\mathrm{fb}}}\right], \qquad (4.7) \\
\gamma &= \gamma_{\mathrm{i}} + g\frac{\omega_{\mathrm{m}}}{\omega}\gamma_{\mathrm{i}}\mathrm{Im}\left[\mathcal{F}(\omega)e^{i\theta_{\mathrm{fb}}}\right], \\
&= \gamma_{\mathrm{i}}\left(1 + g\frac{\omega_{\mathrm{m}}}{\omega}\mathrm{Im}\left[\mathcal{F}(\omega)e^{i\theta_{\mathrm{fb}}}\right]\right). \qquad (4.8)
\end{aligned}$$

Since under Fourier Transform $\dot{x}(t) \rightarrow i\omega x(\omega)$, pure derivative feedback corresponds to $\mathcal{F}(\omega) = i\omega/\omega_{\mathrm{m}}$ and $\theta_{\mathrm{fb}} = 0$. Plugging this in, we obtain a feedback force that only modifies the damping:

$$\omega_{\mathrm{m}} = \omega_{\mathrm{m}}, \tag{4.9}$$

$$\gamma = \gamma_{\mathrm{i}}\left(1 + g\right). \tag{4.10}$$

Using these simplifications obtained for pure derivative feedback, we can rewrite Eq. 4.5 as follows:

$$x(\omega) = \frac{F_{\rm th}(\omega)/m_{\rm eff}}{(\omega_{\rm m}^2 - \omega^2) + i\gamma\omega}, \tag{4.11}$$

$$S_{\rm xx} = \int_0^\infty {\rm d}\omega' \langle x^*(\omega)\, x(\omega')\rangle = \frac{S_{ff}/m_{\rm eff}^2}{(\omega_{\rm m}^2 - \omega^2)^2 + (\gamma\omega)^2}, \tag{4.12}$$

where $S_{\rm xx}$ is the power spectral density of the oscillator's displacement $x(\omega)$ with units of meters^2/Hz. Here, the thermal noise force density that drives the oscillator is given by the fluctuation-dissipation theorem as $S_{ff} = 4\gamma_{\rm i} k_{\rm B} T_{\rm b}$, where $T_{\rm b}$ is the temperature of the thermal bath and $k_{\rm B}$ is Boltzmann's constant. Eq. 4.12 is the form of the mechanical displacement spectral density, S_{xx}, as measured on a spectrum analyzer and shown in Fig. 4.9. This can be understood by looking back at Eq. (1.32) and the surrounding discussion.

We can then see that this modification of γ leads to effective cooling of the mechanical mode's temperature, $T_{\rm m}$, through a relation from the equipartition theorem:

$$\frac{1}{2} k_{\rm B} T_{\rm m} = \frac{1}{2} m_{\rm eff} \omega_{\rm m}^2 \langle x^2 \rangle, \tag{4.13}$$

$$T_{\rm m} = \frac{m_{\rm eff}\omega_{\rm m}^2 \langle x^2\rangle}{k_{\rm B}}. \tag{4.14}$$

The expectation value of the squared displacement is given as follows, again assuming pure derivative feedback:

$$\langle x^2 \rangle = \frac{1}{2\pi}\int_0^\infty S_{\rm xx} d\omega = \int_0^\infty \frac{S_{ff}/m_{\rm eff}^2}{(\omega_{\rm m}^2 - \omega^2)^2 + (\gamma\omega)^2} d\omega. \tag{4.15}$$

Performing the integral in Eq. 4.15 and plugging in for S_{ff}, we find

$$\langle x^2 \rangle = \frac{4\gamma_{\rm i} k_{\rm B} T_{\rm b}}{m_{\rm eff}} \int_0^\infty \frac{1}{(\omega_{\rm m}^2 - \omega^2)^2 + (\gamma\omega)^2} d\omega = \frac{4\gamma_{\rm i} k_{\rm B} T_{\rm b}}{m_{\rm eff}} \frac{1}{4\gamma\omega_{\rm m}^2} = \frac{\gamma_{\rm i} k_{\rm B} T_{\rm b}}{m_{\rm eff}\gamma\omega_{\rm m}^2}. \tag{4.16}$$

If we now insert this into our relation for the mode temperature, Eq. 4.14, and use Eq. 4.10 for the effective mechanical damping rate, we find that this damping cools the mode as well:

$$T_{\rm m} = \frac{m_{\rm eff}\omega_{\rm m}^2}{k_{\rm B}} \frac{\gamma_{\rm i} k_{\rm B} T_{\rm b}}{m_{\rm eff}\gamma\omega_{\rm m}^2} = \frac{\gamma_{\rm i} T_{\rm b}}{\gamma} = \frac{\gamma_{\rm i} T_{\rm b}}{\gamma_{\rm i}(1+g)} = \frac{T_{\rm b}}{1+g}. \tag{4.17}$$

This reduced temperature leads naturally to a reduction in the phonon occupation of the mode,

$\langle n \rangle = \langle \hat{b}^\dagger \hat{b} \rangle$, where $\hat{b}$ is the annihilation operator for the mechanical harmonic oscillator. The key result is the reduction of this occupation because $\langle n \rangle \leq 1$ is considered the quantum regime. The reduction in occupation follows the temperature, since for a thermal sate the phonon occupation is given by

$$\langle n \rangle = \frac{1}{e^{\frac{\hbar\omega_{\mathrm{m}}}{k_{\mathrm{B}}T_{\mathrm{m}}}} - 1} \approx \frac{k_{\mathrm{B}}T_{\mathrm{m}}}{\hbar\omega_{\mathrm{m}}}. \tag{4.18}$$

where we have used an approximation in the final expression that holds when $\langle n \rangle \gg 1$, which is true in this work. Finally, this linear relationship between $\langle n \rangle$ and T_{m} yields the following relation:

$$\langle n \rangle = \frac{\bar{n}_{\mathrm{b}}}{1+g}, \tag{4.19}$$

where $\bar{n}_{\mathrm{b}}$ is the uncooled thermal occupation at the bath temperature, which, again, for $\omega_m/2\pi =$ 940 kHz and $T_{\mathrm{b}} = 295$, is $\bar{n}_{\mathrm{b}} = 6.5 \times 10^6$.

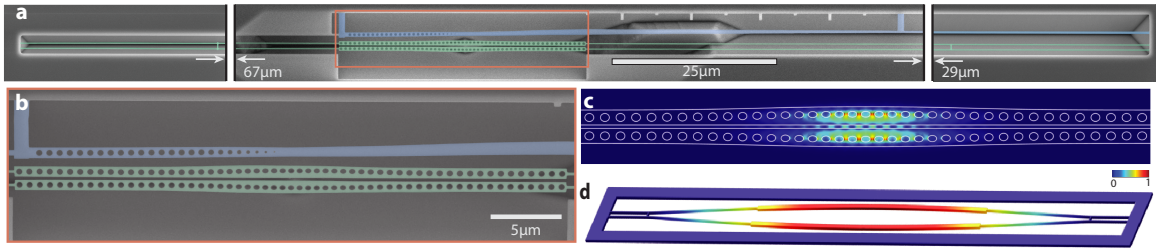

Figure 4.2: **Silicon Nitride Device.** (a) False colour SEM image of a device as used in the experiment, made from highly stressed, 415nm thick, stoichiometric silicon nitride released from a silicon wafer. The device consists of an optical cavity suspended on either side by high aspect ratio tethers (115 μm$\times$130 nm) tethers. The green and blue overlay regions indicate the optomechanical cavity and optical coupling waveguide, respectively. (b) Zoomed-in SEM image of the photonic crystal section (green) and the adiabatically tapered on-chip coupling waveguide (blue). (c) FEM-simulated electromagnetic energy density of the fundamental optical mode used in the experiment, with the outline of the SiN beam shown in white. (d) FEM-simulated first-order differential mechanical mode profile (displacement exaggerated) of a beam similar to that used in the experiment, but with much shorter tethers for clarity. In (c) the colorscale bar indicates large (red) and small (blue) energy density, whereas in (d) the scale bare indicates large (red) and small (blue) displacement amplitude.

This derivation is sufficient to understand the basic physics of the feedback cooling. However, as discussed more fully in Section 4.11, a more rigorous derivation of radiation pressure feedback cooling including quantum noise [74] shows that in the limit of large feedback gain ($g \gg 1$) the cooled phonon occupancy is approximately given by

$$\left(\langle n\rangle + \frac{1}{2}\right) \approx \left(\frac{\bar{n}_{\rm b}}{g}\right) + \left(g n_{\rm imp} + \frac{n_{\rm BA}}{g}\right). \tag{4.20}$$

Here $n_{\rm imp}$ is the open-loop optical vacuum-noise-limited imprecision in units of phonon number for the undamped oscillator, and $n_{\rm BA}$ is the open-loop quantum back-action noise of the optical position measurement. The first term on the right hand side of Eq. (4.20)) represents the damped thermal noise from the bath, and is limited by the achievable feedback gain. The quantum fluctuations of the probe laser light manifest as shot noise, imposing a relation between the imprecision and back-action noise sources, $n_{\rm BA} = 1/(16\eta_{\rm t} n_{\rm imp})$, where $\eta_{\rm t}$ is the quantum efficiency of detection of light that enters into the optomechanical cavity and is scattered by the mechanical resonator. The last two terms on the right hand side of Eq. (4.20)) thus represent a measurement limit to the attainable cooling. The optimal feedback gain is $g_{\rm opt} = \sqrt{(\bar{n}_{\rm b} + n_{\rm BA})/n_{\rm imp}}$, which yields the minimum attainable resonator occupancy, $(\langle n\rangle_{\rm min} + 1/2) = 2\sqrt{n_{\rm imp}\bar{n}_{\rm b} + 1/16\eta_{\rm t}}$. Thus, we find that two fundamental requirements for achieving $\langle n\rangle < 1$ are $n_{\rm imp} < 1/2\bar{n}_{\rm b}$ and $\eta_{\rm t} > 1/9$. As discussed further later, broadening of the mechanical linewidth due to the feedback damping ($\gamma \approx g\gamma_i$) also plays a role, and additional fundamental [74] and technical constraints may limit the maximum attainable feedback gain and cooling.

4.3 Feedback Cooling with Photons

In this section, we more fully explore the origin and magnitude of the damping factor 'g' in our experiment. We do this by considering the feedback force imparted by the feedback-modulated photons in the cavity ($n_{\rm mod}$) given by $F_{\rm fb} = n_{\rm mod}\hbar g_{\rm OM}$, and comparing it to the applied force term on the right-hand side of Eq. 4.4:

$$F_{\rm fb} = n_{\rm mod}\hbar g_{\rm OM} = g m_{\rm eff}\gamma_{\rm i}\omega_{\rm m}\mathcal{F}(\omega)x(\omega)e^{i\theta}. \tag{4.21}$$

To get an intuitive understanding, we now assume ideal derivative feedback and consider only the magnitude of the feedback ($|\mathcal{F}(\omega)e^{i\theta}| = \omega/\omega_{\rm m}$), which for frequencies near the mechanical frequency ($\omega \approx \omega_{\rm m}$) is simply ≈ 1. Solving Eq. 4.21 for g, we get

$$g = \frac{n_{\rm mod}\hbar g_{\rm OM}}{m_{\rm eff}\gamma_{\rm i}\omega_{\rm m} x\,(\omega)}. \tag{4.22}$$

And finally, we plug in our expression for $n_{\rm mod}$ in our setup, obtained after a lengthy derivation,

which has been moved to Appendix B for readability. For simplicity, we leave out the overall gain pre-factor terms of our full expression for n_{mod} (Eq. (B.20)), which depend on the specifics of the detection and electronic feedback circuit. This yields the following form for our gain parameter:

$$g \propto \frac{g_{\mathrm{OM}}^2}{m_{\mathrm{eff}}\gamma_{\mathrm{i}}\omega_{\mathrm{m}}} n_{\mathrm{c}}^{3/2}. \tag{4.23}$$

This shows that in our balanced homodyne setup, we expect the gain to increase as $n_{\mathrm{c}}^{3/2}$, and thus the phonon occupation to decrease as $n_{\mathrm{c}}^{-3/2}$. Fitting the data shown later in this chapter (Fig. 4.9b), we find the phonon occupation indeed follows n_{c}^{p}, where $p = -1.48 \pm 0.02$ with $R^2 = 0.9991$. This simple relation should hold until g reaches the limits of cooling for the system, set by the finite bandwidth of the mechanical mode, measurement imprecision, and the system detection efficiency as discussed fully in Section 4.11.

4.4 Optomechanical Device

Having thoroughly explored the physics of this feedback, we now consider our particular implementation of the feedback. The optomechanical device used in this work, shown in Fig. 4.2(a), consists of a zipper photonic crystal optical cavity [72] supported by nanoscale tethers (see Section 2.1.3). The structure is fabricated using standard electron beam lithography and plasma etching techniques, and formed out of a 400 nm thick layer of stoichiometric silicon nitride (Si_3N_4) deposited on a silicon (Si) handle wafer. The zipper optical cavity (green shaded region of Fig. 4.2(b)) consists of two micron-wide beams with linear hole patterning, separated by a small gap of $s = 150$ nm, and attached to the bulk by 115 μm long nanotethers of width $w = 130$ nm. The optical cavity design was simulated and algorithmically optimized [61] using the COMSOL finite-element-method (FEM) mode solver. The optical cavity mode of interest is the fundamental even mode with electric field polarization predominantly in the plane of the thin film Si_3N_4. The central modification of the hole shape and location strongly confines the electromagnetic energy in the gap between the beams of the optical cavity (see Fig. 4.2(c)), which results in a large shift in the optical mode frequency (ω_{c}) with relative in-plane displacement of the beams. Therefore, the mechanical mode of interest is the fundamental in-plane differential motion of the beams, depicted in Fig. 4.2(d). For the geometry considered here, the optical mode wavelength is in the 1500 nm band ($\omega_{\mathrm{c}} \sim 190$ THz), and the mechanical mode frequency is $\omega_{\mathrm{m}}/2\pi = 940$ kHz due to the large tensile stress in the Si_3N_4 film. The simulated motional mass and zero-point motion amplitude of the mechanical mode are $m_{\mathrm{eff}} = 90\times10^{-15}$ kg and $x_{\mathrm{zp}} = 9.7$ fm, respectively. The linear optomechanical coupling between the optical and mechanical modes is quantified by $g_{\mathrm{OM}} \equiv \partial\omega_{\mathrm{c}}/\partial x$, where the generalized coordinate of

mechanical motion, $x(t)$, is chosen to be the point of maximum in-plane displacement of the beams. This coupling causes mechanical motion to imprint itself linearly on the phase of light reflected from the cavity (see Appendix B).

The system dynamics are governed by the interaction Hamiltonian, $H_{\rm int} = \hbar n_{\rm c} g_{\rm OM} \hat{x}$, where $n_{\rm c}$ is the number of photons in the cavity. This leads to a radiation pressure force given by $F_{\rm rp} = -\partial H_{\rm int}/\partial x = \hbar g_{\rm OM} n_{\rm c}$. By modulating the laser intensity input to the optical cavity proportional to the oscillator's velocity, $-\dot{x}$, we can create a feedback cooling force as in Eq. (4.1). Thus the $g_{\rm OM}$ is a critical parameter that determines the system's ability to both detect and damp the mechanical mode. In principle, small $g_{\rm OM}$ can be overcome with higher photon number, but laser power is typically limited by a host of other issues such as heating, laser noise, and optical cavity stability. For the optical mode of Fig. 4.2(c) and the mechanical motion shown in Fig. 4.2(b) this coupling is simulated to be as large as $g_{\rm OM} = 41$ GHz/nm. Normalized by the zero-point motion amplitude, this corresponds to a vacuum coupling rate of $g_0 = g_{\rm OM} x_{\rm zp} = 358$ kHz.

4.5 Experimental Setup

The experimental setup used to characterize the optical and mechanical properties of the zipper cavity is shown in Fig. 4.3(a). The device is mounted inside a vacuum chamber that reaches a pressure of 2.5×10^{-5} Pa, sufficient to eliminate the effects of gas-damping of the mechanics. A tunable external cavity semiconductor diode laser (New Focus Velocity series) is used to provide both the signal beam on-resonance with the zipper cavity and the local oscillator beam (LO) for homodyne detection. Laser light is efficiently coupled into and out of the zipper cavity using an optical fiber taper [87] in combination with an on-chip tapered waveguide (blue shaded region of Fig. 4.2a,b). Tapering the width of the on-chip waveguide allows for adiabatic mode-conversion between the waveguide and the tapered fiber placed upon it, as in Ref. [106]. The reflected signal beam from the zipper cavity, containing $x(t)$, is separated using an optical circulator and sent to a balanced homodyne detector (BHD). A low-pass filtered (LPF, < 200 kHz) version of the detected signal is sent to a control circuit (PID), which drives a fiber stretcher (FS) to lock the relative phase between LO and signal beam, $\theta_{\rm h}$, and sets the phase quadrature of the homodyne detected signal. A band-pass filtered (BPF, 0.2-1.9 MHz) version of the detected signal is sent to an electronic spectrum analyzer (ESA) to measure the mechanical noise spectrum. In the case of optical feedback, the band-pass filtered signal is also sent to an analog differentiator circuit (Toptica mFALC), whose output is sent through a variable phase shifter, $\Delta\phi$, and finally onto an electro-optic intensity modulator (IM), which closes the feedback loop and modulates the signal beam intensity.

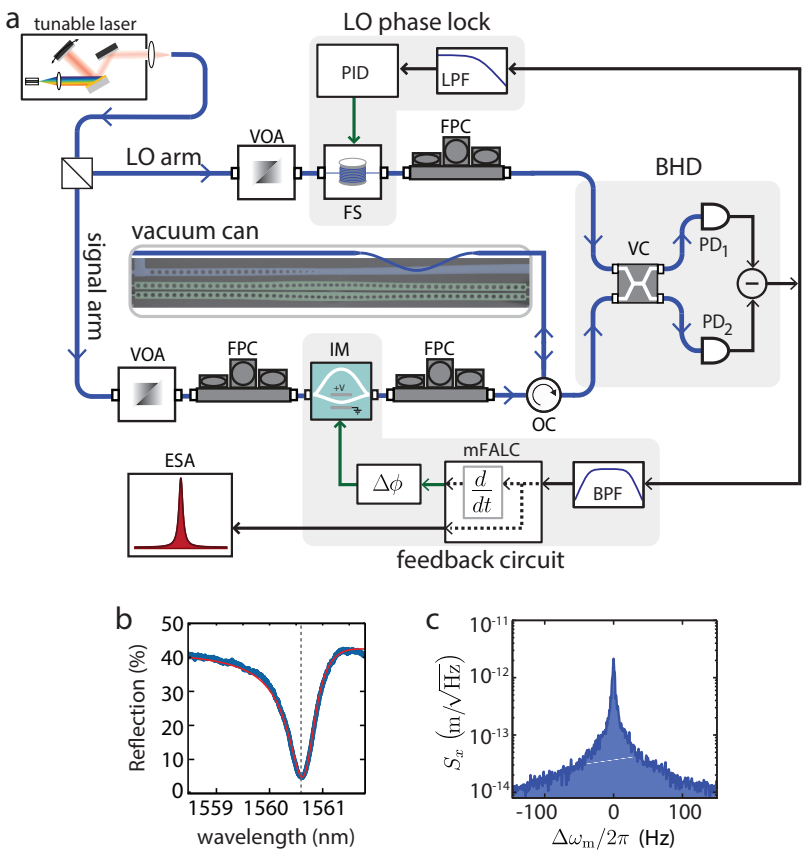

Figure 4.3: **Device Characterization and Experimental Setup.** (a) Schematic of the optical and electrical set-up used to characterize and feedback-cool the mechanical resonator. Additional acronym: fiber polarization controller (FPC). (b) Plot of the laser reflection spectrum when scanned across the optical mode used in the experiment (blue) and fit (red). Dashed grey line indicates on-resonance laser position during measurements. The measured loaded optical Q-factor is $Q_\mathrm{o} = 2.5\times10^3$, with a waveguide loading to total cavity loss rate ratio of $\kappa_\mathrm{e}/\kappa = 0.63$. (c) Power spectral density (PSD) of the mechanical resonator's thermal noise near 940kHz, transduced using the setup in (a) with the laser on resonance, $\Delta_\ell = 0$, and at low power $n_\mathrm{c} \lesssim 1$.

4.6 Optical Characterization

This section describes the optical spectrum of our device and its theoretical fit. Fig. 4.4 shows the full reflection spectrum of our device with three optical modes of our structure in the 1550 nm telecom band. Of the these modes, the one of highest quality factor at 1561 nm is the one used for feedback cooling. Considering the fano-lineshapes of the resonances, we fit the wide optical scan (blue data, Fig. 4.4) to a model consisting of three optical modes and a background, including a relative phase between each, and find good agreement (red curve). The fit to the mode of interest at 1561 nm results in $\omega_\mathrm{c}/2\pi = 192$ THz, $Q_\mathrm{o} = 2500$, $\kappa/2\pi = 77$ GHz, and $\kappa_\mathrm{e}/\kappa = 0.63$, where ω_c is the angular frequency of the optical cavity, Q_o is the quality factor, κ is the total angular loss rate, and κ_e is the angular coupling rate to the waveguide.

The photonic crystal used in this work exhibits a series of optical resonances of different symmetries and orders. A detailed description of a photonic crystal with a similar structure can be found in [107]. The main symmetry of interest is that about a plane which runs parallel to the length of the beams and is situated in the center of the gap between them. The optical field can be either even (E) or odd (0) about this symmetry plane, where E modes have their fields concentrated in the gap and the field of O modes experience a node at the center of the gap. Due to their higher field concentrations in the gap, the resonance frequencies of E modes are more sensitive to the relative motion of the two beams, x, than the O modes are - i.e., E modes tend to have larger optomechanical couplings, $g_{\mathrm{OM}} \equiv d\omega_{\mathrm{c}}/dx$, than O modes. Thus, by measuring how well an optical mode transduces mechanical motion, we can determine its symmetry. Accordingly, we determined that the modes at 1551 nm and 1568 nm were of odd symmetry and the mode of interest at 1561 nm was of even symmetry.

Additionally, there is a symmetry about a plane that runs perpendicular to the length of the beams and centered at the middle of the two beams. The order of this symmetry was determined for each mode by comparing the measured optical frequency to that found from COMSOL Multiphysics simulation [108]. While absolute mode frequency agreement is difficult to obtain due to fabrication imperfections, relative mode spacings agreed very well between experiment and simulation. The order of this symmetry is designated by a 1, 2, or 3 next to the symmetry indication (E,O) in Fig. 4.4. Below the recorded reflection spectra are plots of the simulated energy densities for each identified optical mode.

From the depth and Fano-like shape of the resonance dip, the coupling rate of the cavity to the on-chip waveguide is estimated to be $\kappa_{\mathrm{e}}/2\pi = 49$ GHz. This low Q_{o} was engineered to reduce thermo-refractive noise, thermal bistabilities, and optomechanical nonlinearities. Importantly, $\kappa \gg \omega_{\mathrm{m}}$, which means the cavity field reacts relatively instantaneously to mechanical motion and enables feedback using cavity photons. Measurement of the mechanical motion, $x(t)$, is performed by setting the laser frequency (ω_{ℓ}) to the resonance frequency (ω_{c}) of the optical mode (dashed grey line in Fig. 4.3(c)), and monitoring the phase quadrature ($\theta_{\mathrm{h}} = \pi/2$) on the balanced homodyne detector (see Appendix B). The measured noise power spectral density (NPSD) of the mechanical motion, $S_x(\omega)$, is plotted in Fig. 4.3(c), showing the optically transduced thermal Brownian motion of the mechanical resonance.

4.6.1 Determination and Locking of Homodyne Phase

As shown in Appendix B our ability to detect mechanical motion is proportional to $\sin\theta_{\mathrm{h}}$, so any deviation from an angle of, $\theta_{\mathrm{h}} = \pi/2$, between the signal and local oscillator arms is effectively a loss. This sections describes the experimental details behind stabilizing this relative homodyne phase. This phase angle is set by the relative path lengths of the two arms, and slow thermal drifts

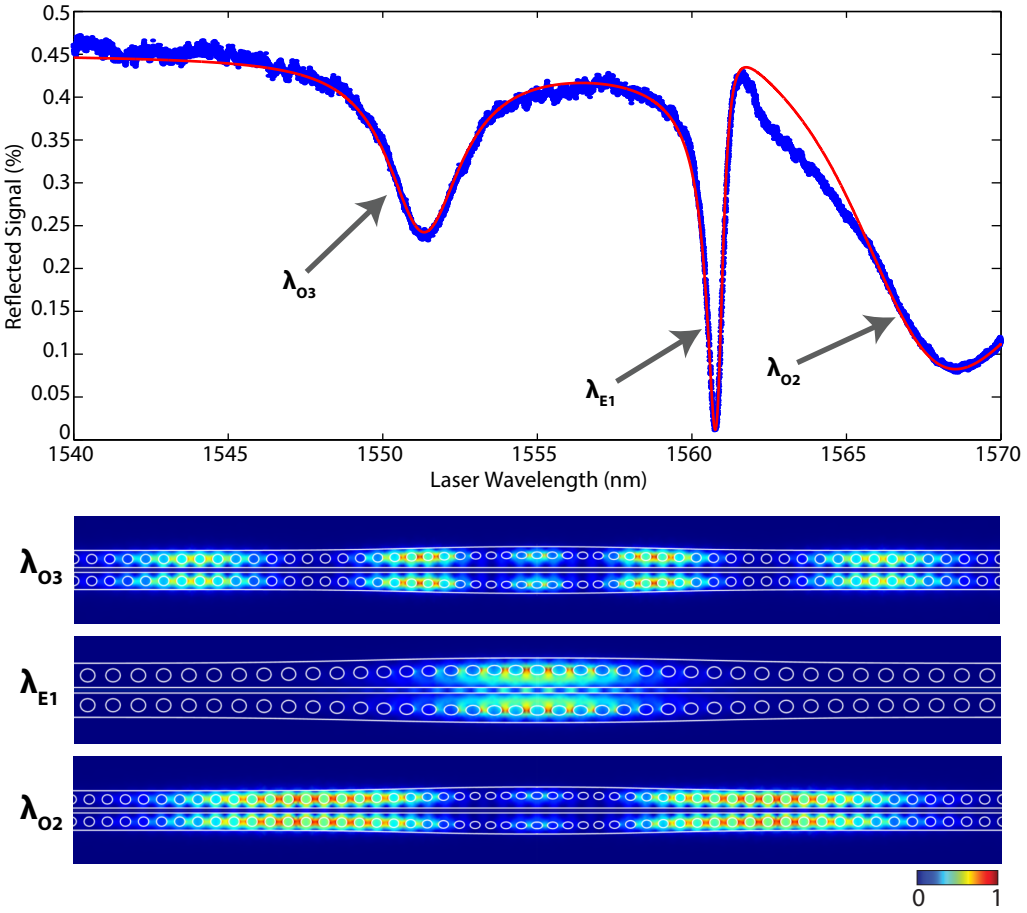

Figure 4.4: **Device Optical Spectrum.** Full calibrated reflected device spectrum (blue) with the fit overlaid (red). The signal level is the ratio of the measured reflected power to the optical power incident at the optical cavity. Figures below are simulations of the energy density of the identified optical modes. We use subscripts underneath each λ to indicate the symmetry and order of the optical mode. Note the difference in optical mode symmetry across the center of the gap between the beams for the even (E) and odd (O) modes.

or acoustic noise can cause changes in the relative length, thus changing the phase. As shown in Fig. 4.3a, the low-frequency components of the detected signal ($f < 200$ kHz) are fed to a digital feedback system (Toptica DigiLock) that has a high-voltage output panel ($V_{\text{out}} \leq 150$ V) which drives a voltage-controlled fiber stretcher (Optiphase PZ1). This fiber stretcher (FS) consists of a long distance of optical fiber (~ 10 m) wrapped around a bulk piezo element. When a voltage is applied, the piezo stretches and lengthens the fiber, thereby changing the path length of one arm of the interferometer and thus changing θ_{h}.

Shown in Fig. 4.5, we set the proper lock-point of this feedback loop by monitoring the homodyne output while linearly driving the FS. This voltage sweep (green) modulates the phase, which we detect as a sinusoidally modulated voltage output proportional to $\cos\theta_{\text{h}}$. The mechanical modulation at $f_{\text{m}} = 940$ kHz is evident in the blue curve as increased noise on the signal, which decreases

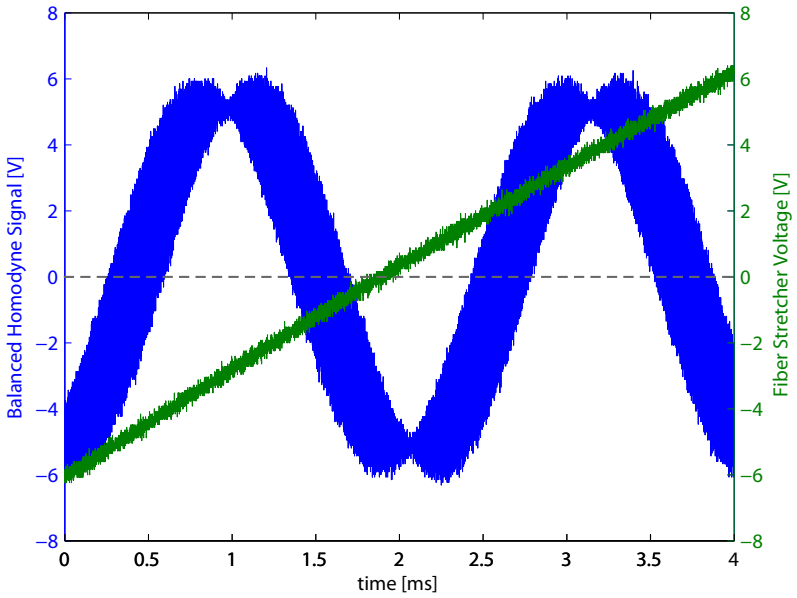

Figure 4.5: **Locking the Homodyne.** Plot of a balanced homodyne signal (blue) as the fiber stretcher voltage is swept (green), with the laser on-resonance with the optical cavity.

rapidly at the maximum/minimum of the curves, where the homodyne setup is insensitive to phase fluctuations (see Appendix B). By observing this curve, we can measure the voltage that corresponds to ($\theta_{\rm h} = \pi/2$) as the average voltage between the peak and trough and set this as the lock point (grey dashed line).

4.7 Measurement of Mechanical Quality

The approximately 1 Hz linewidths of our mechanical modes combined with the minimum resolution bandwidth of our spectrum analyzer (1 Hz) makes measuring mechanical quality factors from their spectral density difficult. However, the amplitude of a thermally-driven resonator will be correlated with itself over a time-scale dictated by the mechanical damping rate corresponding to the coupling of the resonator to the thermal bath. Formally, it can be shown that the autocorrelation of the amplitude, $\langle |x(t)||x(t+\tau)|\rangle$, will decay as $\mathrm{e}^{-t/\tau_{\rm m}}$, where $\tau_{\rm m} = Q_{\rm m,i}/\omega_{\rm m}$, and where $\omega_{\rm m}$ is the intrinsic mechanical angular frequency [90]. The measurements of $x(t)$ are made with the laser on-resonance with the optical cavity and the feedback off. The slowly-varying envelope of $\langle |x(t)|\rangle$ is obtained from the magnitude channel of a lock-in amplifier tuned to the mechanical resonance frequency. We use a bandwidth of $\approx$ 100 Hz, much larger than the mechanical linewidth, which ensures that frequency diffusion does not affect the measurement. In Fig. 4.6, we have numerically computed the autocorrelation and fit the decay to an exponential curve with a constant (noise) offset and we find $\tau_{\rm m} = 90$ ms or equivalently, $\gamma_i/2\pi = 1.76$ Hz, which for $\omega_{\rm m}/2\pi = 940$ kHz yields

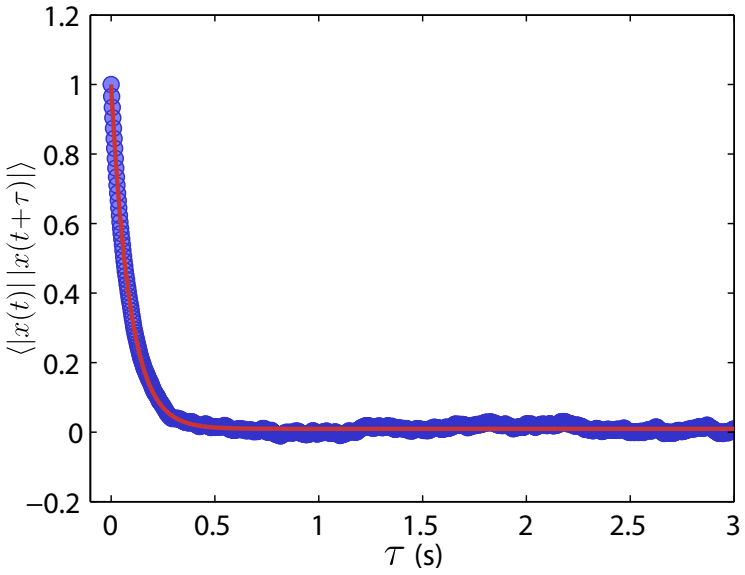

Figure 4.6: **Mechanical Autocorrelation.** Measurement of the intrinsic mechanical quality factor at low optical power and low pressures using temporal amplitude autocorrelation of the mechanical resonator's thermal noise, $\langle |x(t)||x(t+\tau)| \rangle$, (blue data). An exponential fit (red curve) yields an intrinsic mechanical damping rate $\gamma_i/2\pi = 1.76$ Hz and quality factor $Q_{\mathrm{m,i}} = 5.3 \times 10^5$.

$Q_{\mathrm{m,i}} = 5.3 \times 10^5$. Furthermore, to be sure that we are not doing significant dynamic back-action (and thus that we have obtained the *intrinsic* quality factor, $Q_{\mathrm{m,i}}$) we measured the $Q_{\mathrm{m,i}}$ with the laser on-resonance with the cavity and at low optical powers where such effects are negligible.

4.8 Calibrating Optomechanical Coupling Strength

We perform the calibration of our optomechanical coupling, g_{OM}, by measuring the optomechanically-induced spring shift for a sweep of laser-cavity detunings ($\Delta = \omega_\ell - \omega_{\mathrm{c}}$), where $\omega_\ell(\omega_{\mathrm{c}})$ is the frequency of the laser (optical cavity). The curves are fit to the standard optomechanical frequency shift equation [72] as derived in Section 1.2.4:

$$\omega_{\mathrm{m}} = \sqrt{\omega_{\mathrm{m}}^2 + \left(\frac{2\hbar g_{\mathrm{OM}}^2 n_{\mathrm{c}}}{m_{\mathrm{eff}}}\right) \frac{\Delta}{\Delta^2 + \left(\frac{\kappa}{2}\right)^2}}, \tag{4.24}$$

where ω_{m} is the bare mechanical frequency, n_{c} is the number of intracavity photons, m_{eff} is the effective motional mass, κ is the total optical cavity angular loss rate. This, again for small mechanical frequency shifts, reduces to:

$$\omega_{\rm m} = \omega_{\rm m}\sqrt{1+\left(\frac{2\hbar g_{\rm OM}^2 n_{\rm c}}{m_{\rm eff}\omega_{\rm m}^2}\right)\frac{\Delta}{\Delta^2+\left(\frac{\kappa}{2}\right)^2}}$$
$$\approx \omega_{\rm m} + \left(\frac{\hbar g_{\rm OM}^2 n_{\rm c}}{m_{\rm eff}\omega_{\rm m}}\right)\frac{\Delta}{\Delta^2+\left(\frac{\kappa}{2}\right)^2}. \quad (4.25)$$

A hallmark of this spring shift is that it is anti-symmetric about the center of the optical cavity ($\Delta = 0$). In Fig. 4.7 we show the measurement of the spring shift (blue data) and the fit curve (red line), from which, using the other known parameters of our system, we find $g_{\rm OM}/2\pi = 36$ GHz/nm. This agrees well with the simulated value from COMSOL [108] of $g_{\rm OM}/2\pi = 41$ GHz/nm.

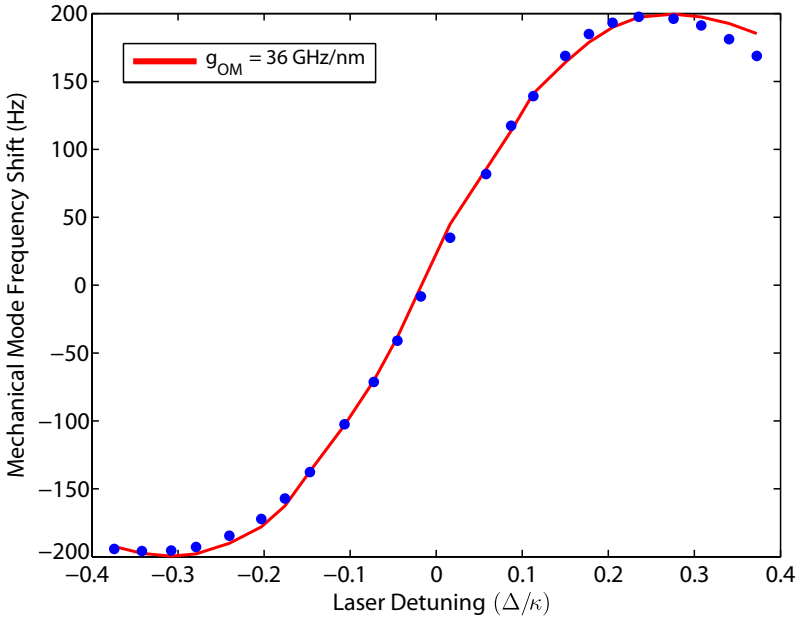

Figure 4.7: **Determination of Optomechanical Coupling.** Measurement of the mechanical spring shift for a range of laser-cavity detunings (blue data) with our theoretical curve (red) corresponding to a coupling of $g_{\rm OM}/2\pi = 36$ GHz/nm or a vacuum coupling rate of $g_0/2\pi = 358$ kHz. This is close to our simulated value of 41 GHZ/nm.

4.9 Verifying Quantum Efficiency

In Fig. 4.3b we plot the reflected optical power normalized by the input power at the device as the laser frequency is scanned across the optical resonance. The background level of this normalized plot, $\eta_{\rm r} = 0.43$, determines the overall detection efficiency of light emitted from the cavity, including collection by the optical fiber, optical loss between the collection fiber and photodetector, and quantum efficiency of the photodetector. This combined with the cavity-coupling ratio ($\kappa_{\rm e}/\kappa$) determines the total detection efficiency of input light that enters the cavity and interacts with the

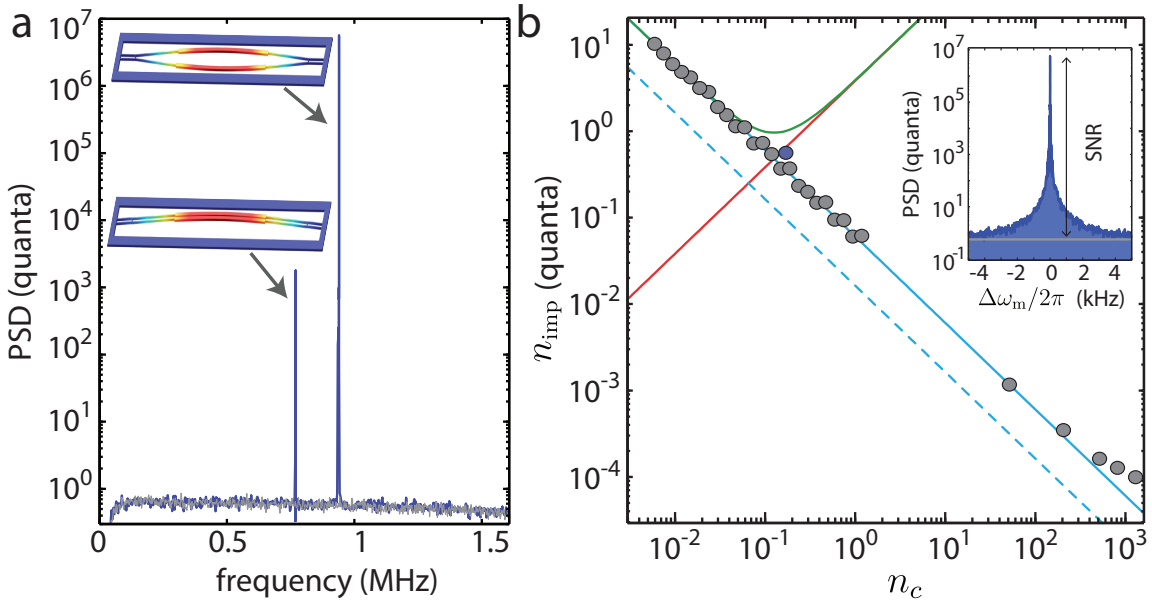

Figure 4.8: **Measurement Imprecision.** (a) Measured wideband power spectral density (PSD) plotted in units of phonon quanta of the dominant mechanical mode at 940 kHz for $n_c = 0.17$ (blue) and with the signal beam blocked ($n_c = 0$; grey curve). The insets of (a) are simulated mechanical mode displacement profiles for the two mechanical resonances visible in the spectrum. The mode at 740 kHz is the poorly transduced in-plane common motion. Frequencies below 200 kHz are attenuated by a high-pass filter and the small slope of the background noise level is a result of the frequency-dependent gain of the balanced photodetectors. (b) Plot of the measured imprecision noise in units of quanta (grey dots), including theoretical prediction (solid cyan curve), theoretical quantum back-action (solid red curve), and their sum (solid green curve) for the measured $\eta_T = 0.27$ with no fit parameters. Corresponding dashed curves are that expected for an ideal continuous position measurement with $\eta_T = 1$. The inset of (b) shows a recorded mechanical spectra at $n_c = 0.17$ and indicates the imprecision measurement procedure, where $n_{\rm imp} = \langle n \rangle / \mathrm{SNR}$.

mechanical resonator, $\eta_t = \eta_r \kappa_e/\kappa = 0.27$. Figure 4.8a shows a wideband spectrum of the measured NPSD ($\theta_h = \pi/2$) at an intracavity photon number of $n_c = 0.17$ (blue curve) and with the signal light off, $n_c = 0$ (grey curve). Measurement of the noise level with the signal light off corresponds to the signal vacuum-noise level; the agreement of the background levels of the blue and grey curves indicates the detection is vacuum-noise-limited at a signal power corresponding to $n_c = 0.17$. In the inset of Fig. 4.8b, we replot the measured NPSD at $n_c = 0.17$ about the thermal noise peak of the in-plane differential mode. Here we have plotted the NPSD in units of phonon quanta using the known room temperature phonon occupation. In these units the thermal mode occupancy ($\bar{n}_b$) and the phonon imprecision level ($n_{\rm imp}$) can be simply read off from the peak height and the background level, respectively [55]. A plot of the measured $n_{\rm imp}$ versus n_c is shown in Fig. 4.8b as grey circles. The expected imprecision due to vacuum noise of the signal beam is given by $n_{\rm imp} = \kappa\gamma_i/(64 n_c g_0^2 \eta_t)$, which is plotted in Fig. 4.8b with no free parameters for the measured $\eta_t = 0.27$ (solid cyan curve). Also plotted are the theoretical quantum back-action due to the shot noise of the signal beam (solid

red curve) and the estimated total added noise (solid green curve). The minimum total added noise occurs at a signal power corresponding to $n_c = 0.12$, and represents the standard quantum limit (SQL) for our measurement set-up, $n_{SQL} = 1/(2\sqrt{\eta_t}) = 0.96$ [55]. The imprecision is vacuum noise limited for all but the highest powers, $n_c \gtrsim 500$, reaching a value 37 dB below the ideal-detection SQL level.

4.10 Feedback Cooling

We now implement feedback cooling of the main 940 kHz mode as shown in Fig. 4.9a. The laser is tuned on resonance with the optical mode, while the BHD signal proportional to $x(t)$, is fed to an electronic feedback circuit, which modulates the intensity of the light incident on the cavity approximately proportional to $-\dot{x}$. At constant electrical gain, optimized for our highest n_c, the number of photons in the cavity is increased, increasing the total loop-gain, and thereby increasing the observed cooling and damping. In Fig. 4.9a, we demonstrate cooled mechanical spectra at chosen n_c with the fit curves (black) used to extract the area and quality factor. The phonon number (plotted as blue circles in Fig. 4.9b) and temperature of the mechanical mode are proportional to the transduced area of the mechanical spectra normalized by n_c (see Section B). Therefore, the relative change in occupation was measured by comparing the normalized transduced mechanical area. In order to get an absolute calibration, the point at lowest n_c in Fig. 4.9b is taken with the feedback off and at a power low enough that dynamic back-action effects are negligible and thus assumed to be at room-temperature (295 K) and occupation ($\langle n \rangle = 6.5 \times 10^6$). Of crucial importance to the interpretation of the data presented in Fig. 4.9 is the fact that the change in the mechanical quality factor (green dots) follows the change in the measured occupation, which, as discussed earlier, is a hallmark of feedback cooling. We quantify the agreement by plotting in the inset of Fig. 4.9b our measured $\langle n \rangle$ against Q_m (blue points) and find that a linear fit line (red) matches the data with R-squared value of 0.9988. We determine that the lowest occupation achieved in this feedback experiment is $\langle n \rangle = 66 \pm 10$, where the linewidth of the resonator has been broadened to 190 kHz. The uncertainty in $\langle n \rangle$ of $\pm 15\%$ is smaller than the data points and is dominated by the 95% confidence interval of the fits to the spectra.

Our current cooling is limited primarily by two sources. An extra time delay of ≈ 1 μs in our feedback loop modifies the broadband phase response of the system away from the ideal value of $\theta_{fb} = 0$, which becomes an issue for $Q_m \approx 1$ (see Section 4.10.2). At our highest experimental power, $n_c = 734$, we were also nearing the power handling capabilities of our device, limited by thermally-induced shifts of the optical cavity that prevent stable locking. However, due to our large initial bath temperature, this heating was not sufficient to cause an observable excess occupation of the mechanical mode. In the following section we go into the limiting imperfections of our feed-back

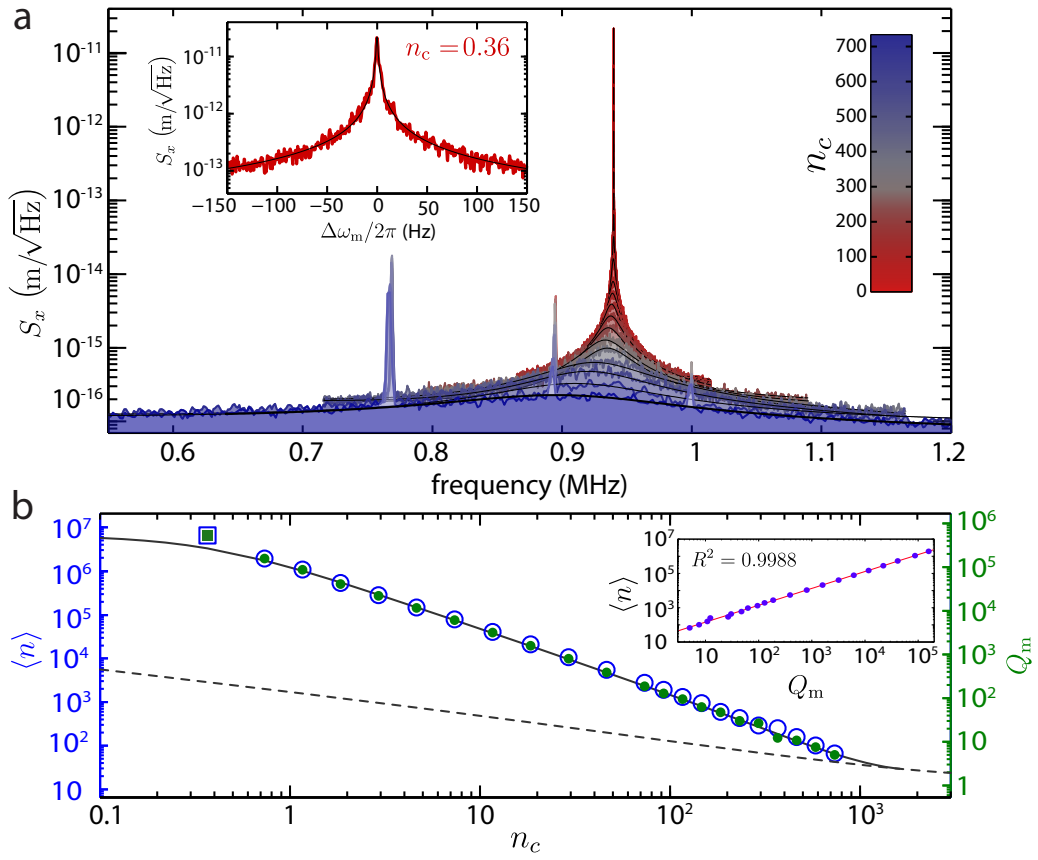

Figure 4.9: **Room Temperature Laser Cooling.** (a) Plots of the transduced mechanical spectra with the optical feedback engaged for increasing n_c, showing the damping and cooling of the dominant mechanical mode. Color scale indicates photon number of each mechanical scan. The black curves are the fits to the measured spectra used to extract the damped mechanial Q-factor (Q_m) and phonon occupation ($\langle n \rangle$). Spectral peaks at 710 kHz and 910 kHz are weakly transduced mechanical modes, while that at 1 MHz is extraneous electronic noise. Inset: room-temperature mechanical spectra taken with the feedback off for calibration. (b) Plot of the inferred $\langle n \rangle$ (blue circles; left axis) and Q_m (green solid circles; right axis) extracted from the fits to spectra shown in (a). The first data point (square), at lowest n_c, is taken from the data in the inset of (a) with the feedback off and is used as a room-temperature calibration. The y-axes scales are normalized such that ideal cold-damping would result in the blue and green data points lying directly on top of each other. Error bars of ±15% are smaller than data points. Solid black curve is theoretical prediction of cooling with no fit parameters and the dashed line is minimum possible cooling for our system if the circuit gain is optimized at each n_c(see Section 4.10.3) for full model). Inset shows the phonon occupation versus mechanical quality factor during cooling run (blue points), and linear best fit curve (red) with $R^2 = 0.9988$, indicating high correlation.

loop.

4.10.1 System Response and Delay Times

In Fig. 4.10 we present the measured amplitude, phase response, and time delay of the analog circuit, mFALC110, used to perform the derivative feedback. The cyan dashed line in Fig. 4.10a indicates the

amplitude response for purely derivative feedback, which is proportional to ω. Over the frequency range used for this experiment (0.7 MHz - 1.2 MHz), the amplitude response deviates from the ideal slope by ≈ 0.5 dB and the phase changes by $\approx 1^{\circ}$. The time delay from the mFALC110 circuit, shown in Fig. 4.10b, is negligible when compared to the mechanical period.

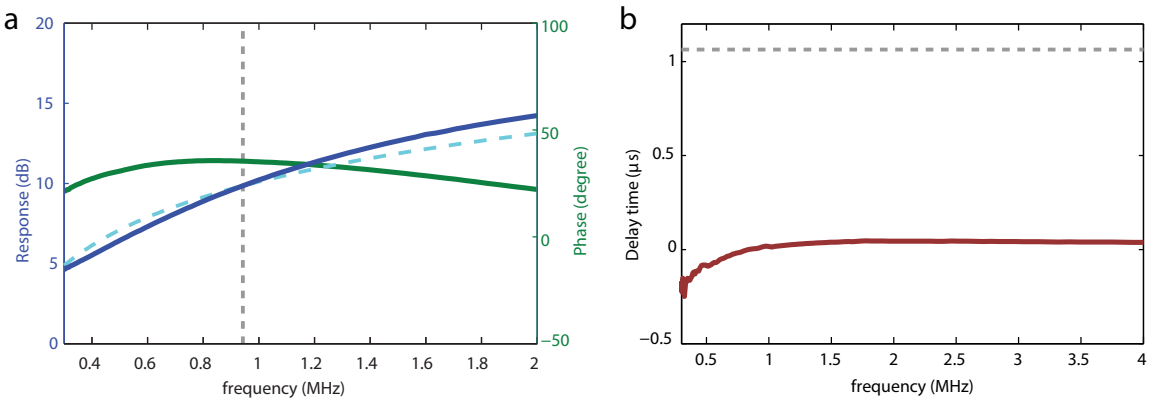

Figure 4.10: **Feedback Circuit Response.** (a) Magnitude (blue) and phase (green) response of the mFALC110 for the settings used in the experiment. Vertical grey dashed line indicates the mechanical frequency and the cyan dashed line indicates the amplitude response for ideal derivative feedback, proportional to ω. (b) Total time delay (red) as measured by the network analyzer. Horizontal grey dashed line indicates one mechanical period.

In Fig. 4.11, we present the amplitude and phase response of the entire feedback loop. It is important to note that this data was taken off-resonance from the optical cavity so that the highly-transduced mechanical motion would not dominate the response. However, we still see a trace of the mechanical response in the jitter of the curve near the mechanical frequency (vertical grey dashed line). Additionally, the homodyne phase was set to be most sensitive to phase fluctuations ($\theta_{\mathrm{h}} = \pi/2$), as in the experiment. Since the Intensity Modulator (IM) changes amplitude, at this homodyne phase the detected amplitude response is attenuated and should be considered in arbitrary units. Nonetheless, in the frequency range of interest, the amplitude response is qualitatively similar to the response of the mFALC110 alone (see Fig. 4.10a). Of notable difference, however, is that the overall delay time is now comparable to the mechanical period (see horizontal grey dashed line in Fig. 4.11b). This delay time was measured to have the following components: ~ 200 ns from the optical detector, ~ 400 ns from the band pass filtering of the feedback circuit, ~ 180 ns from the phase-shifter, and the remainder is dominated by the total signal path length. The non-negligible delay in the rest of the feedback loop requires the inclusion of the phase shifter, which allows us to apply a feedback force that purely damps with little spring shift. A consequence of this nearly constant time delay is that the phase of the feedback signal varies linearly near the mechanical frequency. This becomes important when considering the feedback loop noise in the next section.

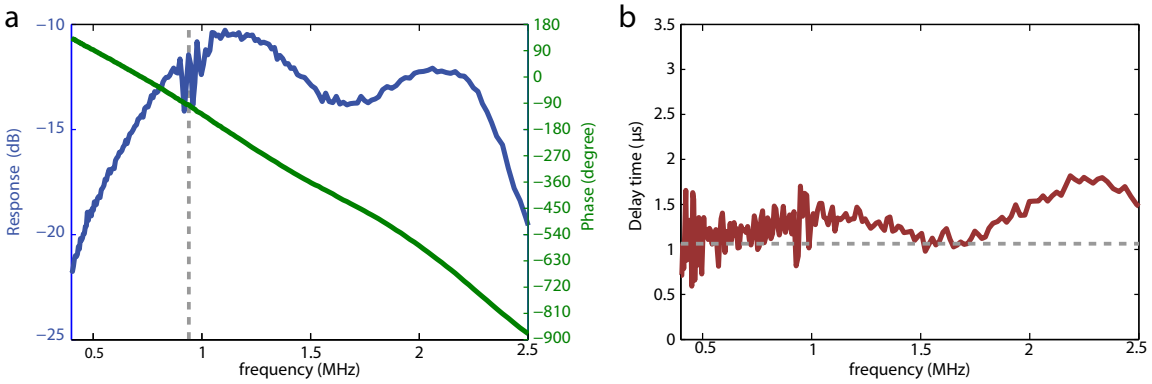

Figure 4.11: **Feedback Loop Response.** (a) Magnitude (blue) and phase (green) response of the entire feedback system including electronics and optical train, with the laser off resonance from the optical cavity. The grey dashed line indicates the mechanical frequency. The jitter centered at the mechanical frequency is simply a result of residual mechanical transduction and is not indicative of a rapidly changing response of the circuit. (b) Total time delay as measured by the Network Analyzer (red). A single mechanical period is indicated by the horizontal grey dashed line.

4.10.2 Wide Span Excess Feedback Loop Noise

This section shows the wide span excess noise (above vacuum noise) observed in our measurement setup at high optical power. It also describes how the excess time delay in the feedback loop from the previous section manifests itself as excess noise in the optical power spectral density at high optical powers. In Fig. 4.12a, we show the wide span NPSD of our device with the lock engaged. At low optical signal power ($n_c \lesssim 100$), the noise floor is set by the vacuum noise of the signal arm (amplified by the large local oscillator power) and the Lorentzian mechanical response dominates the signal. At higher signal powers ($n_c = 734$, green) there is ∼3 dB additional broadband noise above vacuum noise that drops off with increasing frequency, but the mechanical response near 940 kHz still dominates. This broadband noise is also seen with the feedback lock off (Fig. 4.12b). With a separate measurement, we have eliminated laser amplitude noise as a possible source. Additionally, by measuring the same broadband noise off resonance with the optical cavity, we have also eliminated the dispersive nature of the optical cavity and thermorefractive effects as sources of this excess broadband noise. Thus, the noise is likely due to residual phase fluctuations in our homodyne setup. The phase fluctuations likely arise from either the phase noise of the laser, or changes in the relative signal and local oscillator path lengths due to thermal or acoustic noise. In principle, homodyne detection is insensitive to frequency fluctuations of the laser since the laser is interfered with itself. But, in practice, the two arms of the interferometer are never the exact same length, so this relative path length difference causes the laser in the shorter arm to be interfered with light at an earlier time from the longer arm.

It is not this broadband noise which limits our cooling, however. At increased laser power

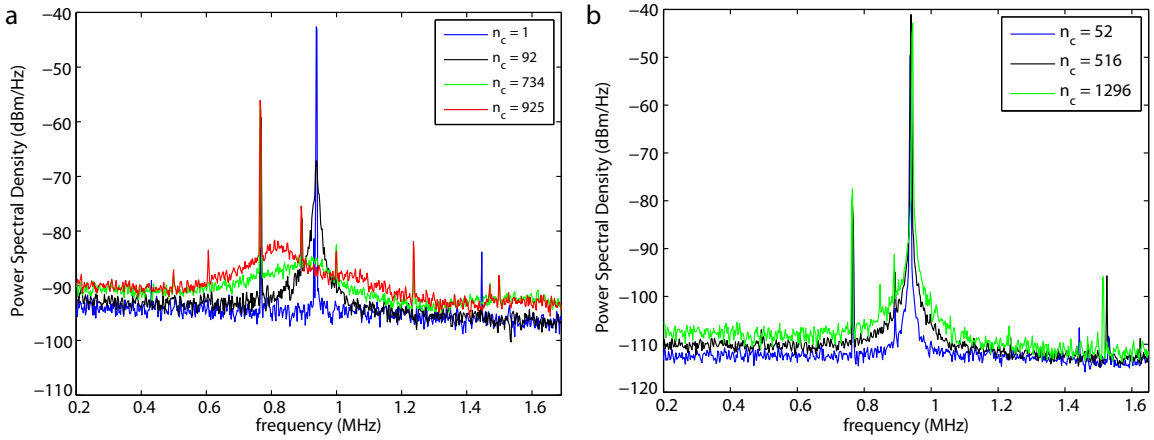

Figure 4.12: **Widespan Noise.** (a) The wide-span noise spectra for a series of experimental powers with the feedback lock engaged and the laser tuned on resonance with the optical cavity. The noise floor at the lowest photon number shown is due to vacuum noise of the signal arm. (b) The wide-span noise spectra for a series of experimental powers with the feedback off and the laser tuned on resonance with the optical cavity. The noise floor at the lowest photon number shown is due to vacuum noise and its slight downward slope is from the detector's response. Please note that the discrepancy between the absolute noise levels between the two plots is because the data were taken at different detector gain and local oscillator powers.

($n_c = 925$, red data in Fig. 4.12) there is a noise hump centered near ~ 800 kHz that dominates our mechanics and prevents further cooling. We measure the NPSD with the laser off-resonance and the feedback engaged in Fig. 4.13. Note that because the data was taken off-resonance, there is very little intracavity power, but for direct comparison we have taken the data at $n_c^{\mathrm{eff}} = 500$, which is the number of photons that would be in the cavity at the same detected optical power with the laser directly on resonance ($\Delta = 0$). The feedback loop has excess noise humps at ≈ 800 kHz, 1.5 MHz, and 2.2 MHz. The semi-periodic peaks in Fig. 4.13 correspond in frequency to where the phase of the entire feedback loop (Fig. 4.11a) is between 0^{o} and 180^{o} modulo 360^{o}, which corresponds to the regions where the feedback loop has positive gain, amplifying fluctuations rather than damping them.

As can be seen in Fig. 4.13, detection of this extra amplitude noise can be suppressed by accurately setting the lock point of the homodyne phase. If the homodyne phase is locked to the phase quadrature ($\theta_{\mathrm{h}} = \pi/2$), the detection system is very insensitive to amplitude fluctuations (see Eq. (B.6)). If we lock to a homodyne phase away from $\theta_{\mathrm{h}} = \pi/2$, we begin to detect the amplitude modulation in the feedback loop, and the noise humps are visible.

However, when we are on resonance with the optical cavity, the mechanical oscillator acts as an element which can convert amplitude modulation of the light into phase modulation. Even at the ideal homodyne phase, the amplitude modulated light exerts a force on the mechanical oscillator, and the resulting displacement of the mechanical oscillator modulates the phase of the light via

its modulation of the optical cavity resonance frequency ($\delta\omega_c = g_{OM}\delta x$). Thus, the extra noise peaks seen in the off-resonance spectra in Fig. 4.13 get colored by the mechanical response function (Eq. (4.5)) in the on-resonance cooling data presented in Fig. 4.12a. This explains why in the red data curve of Fig. 4.12a we see the ~ 800 kHz peak much larger than the ~ 1.5 MHz peak. Thus, the excess delay of ~ 1 mechanical period, can explain these noise 'humps' and why we cannot reliably damp the mode below $Q_m \approx 5$. Past a certain power, the gain due to the non-ideal phase of the circuit becomes too large. As noted in Section 4.11, though, despite this extra time-delay we are close to the expected cooling from an ideal feedback circuit at this optical power.

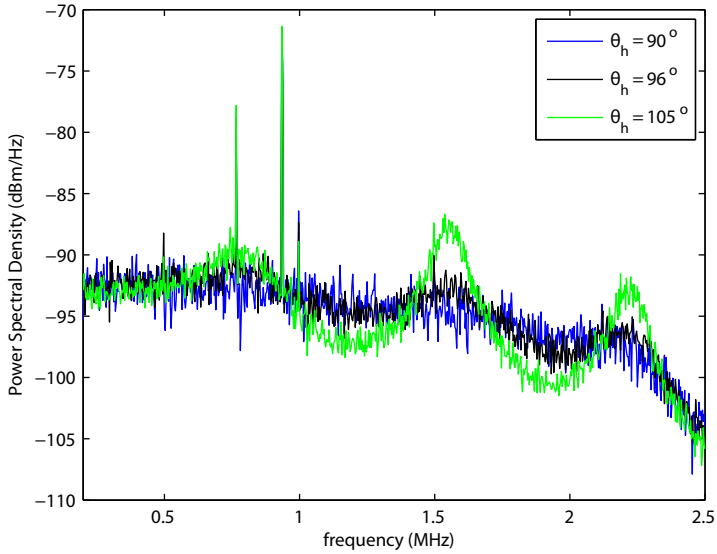

Figure 4.13: **Feedback Loop Noise.** Examples of the wide-span noise spectra for different homodyne phase, θ_h, lock points with the feedback lock engaged and the laser far blue detuned from the optical resonance ($\Delta \gg \kappa$). Measurement taken at $n_c^{\text{eff}} = 500$, which is the number of photons that would need to be in the cavity to yield the same power at the detector if the laser were on resonance $\Delta = 0$. The blue data is taken with the homodyne lock point set to the middle of a fringe, i.e., $\theta_h = \pi/2 = 90^o$, making detection insensitive to the amplitude fluctuations. The other data sets are taken below the mid-fringe point, allowing detection of the amplitude fluctuations.

4.10.3 Theoretical Cooling Results

In this section, we extend the rigorous radiation pressure feedback cooling results from Section 4.11 to our measured feedback response function as seen in Fig. 4.11. The analytical results given in Eq. (4.35) and Eq. (4.36) do not exactly hold at the highest intracavity photon numbers in our experiment because of our non-ideal response function. We can accurately estimate our expected cooling using the spectral response of our system shown in Fig. 4.11 and our calculated magnitude of the gain at the mechanical frequency given by Eq. (4.22) and Eq. (B.20). We do this by calculating the mechanical displacement spectrum $S_{xx}(\omega)$ using, again, a formula from Ref. [74] (Eq. 43):

$$S_{\mathrm{xx}} = |\chi_{\mathrm{eff}}(\omega)|^2 \left[S_{\mathrm{th}}(\omega) + S_{\mathrm{rp}}(\omega) + S_{\mathrm{fb}}(\omega)\right]. \tag{4.26}$$

Here, S_{th} is the thermal noise contribution, S_{rp} is the contribution from bare radiation pressure, S_{fb} is the feedback noise driving the system, and χ_{eff} is the effective mechanical susceptibility, modified by the feedback gain. They are given by

$$S_{\mathrm{th}} = \frac{\gamma\omega}{\omega_{\mathrm{m}}} \coth\left(\frac{\hbar\omega}{2k_{\mathrm{B}}T_{\mathrm{b}}}\right) \approx \gamma\frac{2k_{\mathrm{B}}T_{\mathrm{b}}}{\hbar\omega_{\mathrm{m}}} \approx \gamma\left(2\langle n\rangle + 1\right), \tag{4.27}$$

$$S_{\mathrm{rp}} = \frac{\mathrm{G}^2\kappa\left[\Delta^2 + \kappa^2 + \omega^2\right]}{\left[\kappa^2 + (\omega-\Delta)^2\right]\left[\kappa^2 + (\omega+\Delta)^2\right]}, \tag{4.28}$$

$$S_{\mathrm{fb}} = \frac{|g(\omega)|^2}{4\kappa\eta_{\mathrm{t}}}, \tag{4.29}$$

$$\chi_{\mathrm{eff}} = \omega_{\mathrm{m}}\left[\omega_{\mathrm{m}}^2 - \omega^2 - i\omega\gamma + \frac{g(\omega)\,\mathrm{G}^2\omega_{\mathrm{m}}}{\kappa - i\omega}\right]^{-1}, \tag{4.30}$$

where G is defined in Eq. (4.33). We calculate the effective phonon occupancy of the mode using the relation in Eq. (4.41), and calculating the variances in position and momentum with these integrals over the position spectrum, noting that the spectral density conventions of Ref. [74] requires integration from $-\infty$ to ∞:

$$\langle q^2\rangle = \int_{-\infty}^{\infty}\frac{\mathrm{d}\omega}{2\pi}S_{\mathrm{xx}}(\omega) \tag{4.31}$$

$$\langle p^2\rangle = \int_{-\infty}^{\infty}\frac{\mathrm{d}\omega}{2\pi}\frac{\omega^2}{\omega_{\mathrm{m}}^2}S_{\mathrm{xx}}(\omega). \tag{4.32}$$

Using these formulas and our known gains produces the solid black line in Fig. 4.9, and reproduced here in Fig. 4.14. If we allow the gain to be a free parameter, and find the maximum cooling at each n_{c}, we get the dashed black curve. For comparison, we plot in solid red the theoretical cooling for an ideal derivative circuit using using our total gain at each n_{c}. In the dashed red, we again allow gain to be a free parameter, and find the minimum. We see that except for deviations at the highest powers, these two results are in close agreement. We do not plot the expected phonon occupation for our system past $n_{\mathrm{c}} > 5,000$, because at these large gains/photon numbers the calculated displacement spectrum of the oscillator is highly non-Lorentzian, due to the added phase delay in the system. Thus, we do not feel confident in assigning an effective temperature to the mode since it is no longer well-modeled as a simple mechanical mode.

So, as observed, we calculate that our modified response function helps marginally at the powers

presented in our experiment, but that at higher powers it is a limitation.

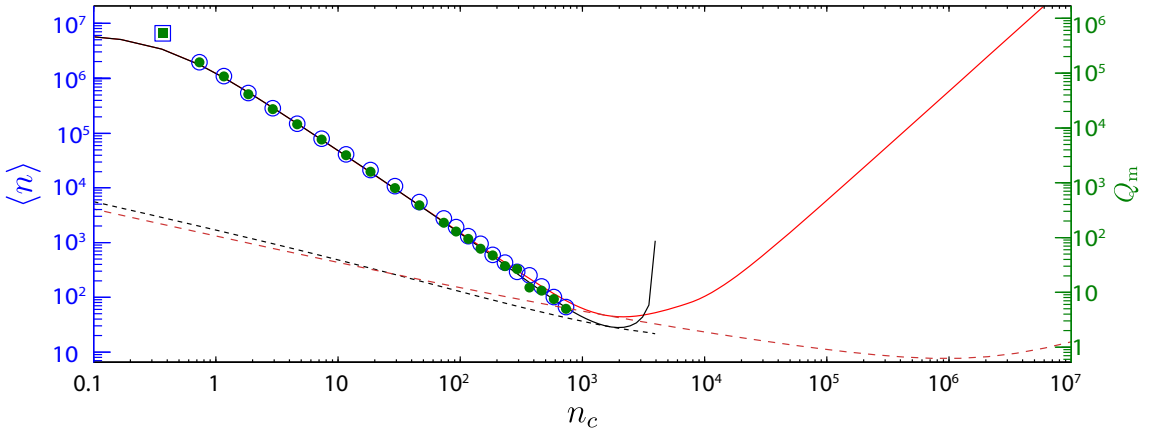

Figure 4.14: **Cooling Compared to Calculations.** Plot of the cooling results as in Fig. 4.9, but with our theoretical curves plotted out to higher powers. The open blue symbols indicate the estimated phonon occupancy, and the green points indicate the measured mechanical Q. Square points indicate initial calibration points taken with the feedback off. The solid lines are our theoretical expectation using our known, fixed, system response function (black) and that expected for ideal derivative feedback circuit with fixed gain (red). The dashed lines are the minimum expected phonon number achievable when the gain is a free parameter for our system (black) and ideal derivative feedback (red).

4.11 Radiation Pressure Feedback Fundamental Cooling Limits

In this section we present, without derivation, the final results from Ref. [74] (Eq. 61-62) for the variances of the position and momentum of a harmonic oscillator in a derivative feedback loop, with an on-resonant quantum noise limited laser and the resultant cooling limits. First, though, we define the terms used:

$$g_0 = g_{\rm OM} x_{\rm zp}, \quad G = g_0\sqrt{n_{\rm c}}, \quad n_{\rm imp} = \frac{\kappa\gamma_{\rm i}}{64G^2\eta_{\rm t}}, \quad n_{\rm BA} = \frac{4G^2}{\kappa\gamma_{\rm i}}, \quad g = \frac{4g_{\rm cd}G\omega_{\rm m}}{\kappa\gamma_{\rm i}}, \tag{4.33}$$

where $x_{\rm zp} = \sqrt{\hbar/2m_{\rm eff}\omega_{\rm m}}$ is the zero-point fluctuation amplitude, G is the coupling rate between the optics and the mechanics, $n_{\rm c}$ is the intracavity photon number as defined in Eq. (1.20), $n_{\rm imp}$ is the shot noise imprecision in phonon number, $n_{\rm BA}$ is the quantum back-action of the shot noise in phonon number, $\eta_{\rm t}$ is the total quantum detection efficiency [55], g is a normalized unitless coupling strength, equivalent to that used in the Section 4.10.3, and $g_{\rm cd}$ is a unitless gain term accounting for the feedback circuit response.

The feedback function is taken to be a standard derivative high-pass filter with cut-off frequency, $\omega_{\rm fb}$:

$$\mathcal{F}(\omega) = \frac{-i\omega g_{\rm cd}}{1 - i\omega/\omega_{\rm fb}} \ . \tag{4.34}$$

Including this, the variances of the two quadratures of the mechanical mode are given by (under certain assumptions valid in this work, see Ref. [74])

$$\langle \delta q^2 \rangle = \left[g^2 n_{\rm imp} + \left(\bar{n}_{\rm b} + \frac{1}{2} + n_{\rm BA} \right) \left(1 + \frac{\omega_{\rm m}^2}{\omega_{\rm fb}^2} \right) \right] \left(1 + g + \frac{\omega_{\rm m}^2}{\omega_{\rm fb}^2} \right)^{-1} \tag{4.35}$$

$$\langle \delta p^2 \rangle = \left[g^2 n_{\rm imp} \left(1 + \frac{g\gamma_{\rm i}\omega_{\rm fb}}{\omega_{\rm m}^2} \right) + \left(\bar{n}_{\rm b} + \frac{1}{2} + n_{\rm BA} \right) \left(1 + \frac{\omega_{\rm m}^2}{\omega_{\rm fb}^2} + \frac{g\gamma_{\rm i}}{\omega_{\rm fb}} \right) \right] \left(1 + g + \frac{\omega_{\rm m}^2}{\omega_{\rm fb}^2} \right)^{-1} . \tag{4.36}$$

To determine the fundamental cooling limits from these equations we take the limit of high-bandwidth $(\omega_{\rm m}/\omega_{\rm fb})^2 \ll 1$ and $g \gg 1$, which allows us to drop some terms, and write a simpler formula for the position fluctuations:

$$\langle \delta q^2 \rangle = g n_{\rm imp} + \frac{n_{\rm BA}}{g} + \frac{\bar{n}_{\rm b}}{g}. \tag{4.37}$$

Taking the same limits for the momentum variance, we find

$$\begin{aligned} \langle \delta p^2 \rangle &= g n_{\rm imp} \left(1 + \frac{g\gamma_{\rm i}\omega_{\rm fb}}{\omega_{\rm m}^2} \right) + \frac{n_{\rm BA}}{g} + \frac{\bar{n}_{\rm b}}{g} + \frac{\gamma_{\rm i}}{\omega_{\rm fb}} \left(\bar{n}_{\rm b} + n_{\rm BA} \right), \\ &= \left[g n_{\rm imp} + \frac{n_{\rm BA}}{g} + \frac{\bar{n}_{\rm b}}{g} \right] + \gamma_{\rm i} \left[\frac{g^2 n_{\rm imp}\omega_{\rm fb}}{\omega_{\rm m}^2} + \frac{1}{\omega_{\rm fb}} \left(\bar{n}_{\rm b} + n_{\rm BA} \right) \right]. \end{aligned} \tag{4.38}$$

Here we note that the first bracketed term on the RHS of the formula for the momentum variance looks the same as that for the position variance in Eq. (4.37). For now we will assume that the second bracketed term on the RHS is small and ignore it. We will revisit this assumption at a later point and determine when this assumption is valid. To be explicit, our working assumption is stated below:

$$\gamma_{\rm i} \left[\frac{g^2 n_{\rm imp}\omega_{\rm fb}}{\omega_{\rm m}^2} + \frac{1}{\omega_{\rm fb}} \left(\bar{n}_{\rm b} + n_{\rm BA} \right) \right] < 1. \tag{4.39}$$

This leaves us with the expected form of the momentum variance,

$$\langle \delta p^2 \rangle = g n_{\mathrm{imp}} + \frac{n_{\mathrm{BA}}}{g} + \frac{\bar{n}_{\mathrm{b}}}{g}.. \tag{4.40}$$

In order to relate these variances to a phonon occupation number, we equate the total energy of the oscillator to the sum of its variances:

$$\mathrm{U} = \frac{\hbar \omega_{\mathrm{m}}}{2} \left[\langle \delta q^2 \rangle + \langle \delta p^2 \rangle \right] = \hbar \omega_{\mathrm{m}} \left(\langle n \rangle + \frac{1}{2} \right), \tag{4.41}$$

where the final term of $1/2$ on the right hand side is due to the ground-state (or zero-point) amplitude. We solve for the occupation as:

$$\langle n \rangle + \frac{1}{2} = \frac{1}{2} \left[\langle \delta q^2 \rangle + \langle \delta p^2 \rangle \right]. \tag{4.42}$$

And plugging in our simplified formulas for the variances (Eq. (4.37) and Eq. (4.40)) yields Eq. (4.20):

$$\langle n \rangle + \frac{1}{2} = g n_{\mathrm{imp}} + \frac{n_{\mathrm{BA}}}{g} + \frac{\bar{n}_{\mathrm{b}}}{g}. \tag{4.43}$$

Solving for the optimal g that minimizes $\langle n \rangle$, we find

$$g_{\mathrm{opt}} = \sqrt{\frac{\bar{n}_{\mathrm{b}} + n_{\mathrm{BA}}}{n_{\mathrm{imp}}}}, \tag{4.44}$$

and plugging back in yields

$$\langle n \rangle + \frac{1}{2} = 2\sqrt{n_{\mathrm{imp}} \left(\bar{n}_{\mathrm{b}} + n_{\mathrm{BA}} \right)} = 2\sqrt{n_{\mathrm{imp}} \bar{n}_{\mathrm{b}} + \frac{1}{16 \eta_{\mathrm{t}}}}. \tag{4.45}$$

Where in the final expression we have used the relation $n_{\mathrm{BA}} = 1/(16 \eta_{\mathrm{t}} n_{\mathrm{imp}})$. From these final results, we can establish two requirements for reaching $\langle n \rangle < 1$:

$$\eta_{\mathrm{t}} > \frac{1}{9} \qquad (\text{at} \;\; n_{\mathrm{imp}} \bar{n}_{\mathrm{b}} = 0), \tag{4.46}$$

$$n_{\mathrm{imp}} < \frac{1}{16 \bar{n}_{\mathrm{b}}} \left(9 - \frac{1}{\eta_{\mathrm{t}}} \right). \tag{4.47}$$

Of course, one needs the technical ability to reach large enough g and low enough n_{imp}, which can

be achieved with strong enough optomechanical coupling, or high enough laser power. Furthermore, we must be in a parameter regime that satisfies the assumption we made in Eq. (4.39). Plugging in g_{opt} into Eq. (4.39) yields the following:

$$Q_{\mathrm{m,i}} > (\bar{n}_{\mathrm{b}} + n_{_{\mathrm{BA}}}) \left(\frac{\omega_{\mathrm{fb}}}{\omega_{\mathrm{m}}}\right), \tag{4.48}$$

where we have again used $\left(\frac{\omega_{\mathrm{m}}}{\omega_{\mathrm{fb}}}\right)^2 \ll 1$. This relation can be further simplified by saturating the inequality in Eq. (4.47) and relating n_{imp} to $n_{_{\mathrm{BA}}}$ to yield the following:

$$Q_{\mathrm{m,i}} > \left(\bar{n}_{\mathrm{b}} + \frac{\bar{n}_{\mathrm{b}}}{9\eta_{\mathrm{t}} - 1}\right) \left(\frac{\omega_{\mathrm{fb}}}{\omega_{\mathrm{m}}}\right). \tag{4.49}$$

We can simplify further by assuming $\eta_{\mathrm{t}} = 1$ and using $\omega_{\mathrm{fb}} \approx 3\omega_{\mathrm{m}}$, which is numerically found to be the optimal feedback bandwidth in most cases [74], and this yields the requirement

$$Q_{\mathrm{m,i}} \gtrsim 3\bar{n}_{\mathrm{b}}. \tag{4.50}$$

This is the approximate intrinsic mechanical quality factor needed to reach the ground state with this ideal radiation pressure feedback control.

We can also use the full formulas, Eq. (4.35) and Eq. (4.36), to predict the maximum cooling for a given set of parameters. The theoretical results are plotted for our system parameters, with the measured detection efficiency ($\eta_{\mathrm{t}} = 0.27$) in Fig. 4.15a and for perfect detection efficiency ($\eta_{\mathrm{t}} = 1$) in Fig. 4.15b. At our detection efficiency, the minimum achievable occupation is $\langle n \rangle \cong 8$, and for perfect detection efficiency $\langle n \rangle_{\mathrm{min}} \cong 6$. However, achieving this level of cooling requires using very high intracavity photon numbers, which would cause thermal instabilities in our system. For our system at a maximum intracavity photon number, $n_{\mathrm{c}} \cong 734$, the best achievable result is $\langle n \rangle_{\mathrm{min}} \cong 64$. With perfect detection efficiency, at this photon number one could obtain $\langle n \rangle_{\mathrm{min}} \cong 38$. Thus, we can see that the cooling result presented, $\langle n \rangle = 66$, is very close to that of a system with ideal quantum noise limits and an ideal derivative feedback circuit at this optical power.

4.12 Conclusion

Cooling to the ground-state ($\langle n \rangle \lesssim 1$) from room temperature remains a possibility, but requires improvement to our device and experimental setup. With an ideal derivative feedback circuit and quantum-limited imprecision, we calculate that we need to modestly increase the detection effi-

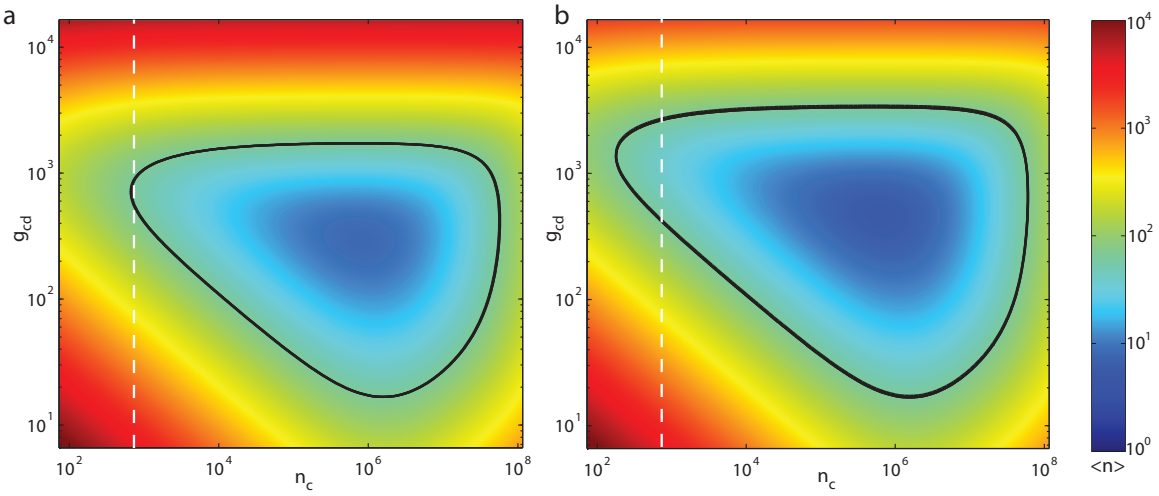

Figure 4.15: **Minimum Feedback Cooling Surfaces.** (a) Color density plot of $\langle n \rangle$ for ideal radiation-pressure derivative feedback cooling using the measured device parameters, versus normalized gain and photon number. Black line is a contour at $\langle n \rangle = 66$, the minimum phonon number achieved in the experiment. The white dashed line denotes $n_c = 734$, which is near the maximum number of photons that can stably occupy the cavity. The minimum occupation is $\langle n \rangle_{\rm min} \cong 64$ for $n_c = 734$. The global minimum at the ideal power and gain is $\langle n \rangle_{\rm min} \cong 8$. (b) Same as (a) except with perfect detection efficiency $\eta_t = 1$. The minimum occupation is $\langle n \rangle_{\rm min} \cong 38$ for $n_c = 734$. The global minimum at the ideal power and gain is $\langle n \rangle_{\rm min} \cong 6$.

ciency ($\eta_t = 0.5$) but primarily require better mechanical quality factor $Q_m = 30 \times 10^6$ [74]. This improved quality factor could be achieved by modifying the structure to minimize losses at the clamp points [42], engineering Silicon Nitride with fewer bulk defects and higher stress [41], or possibly moving to stressed crystalline thin-films [109]. However, reaching the ground-state with our demonstrated coupling strength would still require a prohibitively large intracavity photon number $n_c \approx 46,000$. By increasing the coupling to that previously demonstrated in similar devices ($g_{OM} = 200$ GHz/nm) [107] this can be lowered to a more realistic $n_c \approx 1,400$.

Most interesting quantum applications require that the rate at which measurement information is gained about the mechanics, $\Gamma_{\rm meas} = 4n_c(g_{OM}x_{zp})^2/\kappa$, be greater than the rate at which information is lost to the thermal bath $\Gamma_{\rm th} = \gamma_i \bar{n}_b$, a regime recently approached in optomechanical systems at liquid helium temperatures [110]. Improvements upon the work shown here, by obviating the need for cryogenic equipment, would enable simpler utilization of mechanical systems for quantum measurement protocols [19]. Futhermore, advanced pulsed measurement schemes are a promising alternative method to observe non-gaussian distributions such as squeezing [111] or superpositions [112] at elevated temperatures. But, achieving even modest phonon occupations ($\langle n \rangle = 5 - 10$) may allow observation of the quantum asymmetry in the oscillator's absorption and emission of phonons [17, 45].

These results have direct application to the field of inertial sensors. Feedback control is useful to

change the response, bandwidth, and dynamic range of the mechanical systems commonly employed in sensors of force, mass, acceleration, and rotation [113]. Our results show that a high-quality resonator can be cooled, damped, and stabilized by 50 dB solely with radiation pressure feedback. This improves the bandwidth of the resonator's response from 1.7 Hz to 200 kHz, reducing the system ring-down time from 0.6 s to 5 μs, while preserving the un-damped thermal noise resolution, 125 aN/Hz$^{1/2}$. When applied to the field of atomic force microscopy, these results could improve imaging resolution by reducing thermal noise [114], and the increased sensor bandwidth would allow monitoring of molecular motion with $\sim \mu$s time resolution [115].

Chapter 5

Controlling Nonlinear Dynamics in an Optomechanical Crystal [116]

5.1 Introduction

Utilizing a 1D silicon optomechanical crystal, we investigate the attractor diagram arising from the radiation pressure interaction. We observe highly-nonlinear driving of mechanical self-oscillations. We then introduce time-dependent control of the nonlinear dynamics to steer the system towards an otherwise inaccessible dynamically stable attractor. We find good agreement between our results and an analytical model. This opens up the door to precision metrology via latching measurements, as well as providing an accessible method to understanding optomechanics in the nonlinear regime.

The field of optomechanics, concerned with the interaction of an optical cavity and a mechanical resonator [1], has been of recent interest for its promise for use in sensors [95, 117], nonlinear optics [56, 118], and demonstrations of macroscopic quantum mechanics [19, 119]. Typically, the mechanical displacement linearly modulates the frequency of the optical resonance, but this gives rise to an inherently nonlinear phase modulation, and, through radiation-pressure backaction on the mechanical element, yields complicated system dynamics [120]. Much of the previous work has focused on the linearized regime where the interaction with the optical field still gives rise to a host of interesting phenomena such as a modified spring constant [72], damping or amplification of the mechanics [76], and EIT-like slow-light effects [57, 121]. Recently, several groups have pushed into the quantum regime using optomechanical laser cooling to damp a resonator to near its quantum ground state amplitude [11, 13].

In this work, we instead demonstrate new features and tools in the nonlinear regime of large mechanical oscillation amplitudes. Previous experimental works have shown that a blue-detuned laser drive can lead to stable mechanical self-oscillations [122–125], or even chaotic motion [126]. Theoretical predictions of an intricate multistable attractor diagram [120] have so far eluded experimental observation, except for the elementary demonstration of dynamical bistability in a photothermally

driven system [127]. In the present work, we are able to verify the predicted attractor diagram and further utilize a modulated laser drive to steer the system into an isolated high-amplitude attractor. This introduces pulsed control of nonlinear dynamics in optomechanical systems dominated by radiation pressure backaction, in analogy to what has been shown recently for a system with an intrinsic mechanical nonlinearity [128].

5.2 Device and Setup Exposition

We employ a 1D optomechanical crystal (OMC) designed to have strongly interacting optical and mechanical resonances [61]. We fabricate this nano-scale structure from a free-standing silicon beam by etching into it a periodic array of holes which act as bragg mirrors for both acoustic and optical waves [129]. By perturbing this periodicity, a central defect region is created which co-localizes optical modes designed to fall in the telecommunications band ($\lambda_c \approx 1550$ nm), and acoustic modes in the microwave band ($\omega_m \approx 4$ GHz). A scanning electron micrograph (SEM) of the beam is shown in Fig. 5.1a along with finite element method (FEM) simulations of the optical (Fig. 5.1b) and mechanical (Fig. 5.1c) modes. To reduce radiation of the mechanical energy into the bulk, the OMC is surrounded by a periodic 'cross' structure which has a full acoustic bandgap around the mechanical frequency (Fig. 5.1a, green overlay) [130].

The experimental setup is shown schematically in Fig. 5.1d. The silicon chip containing the device is placed into a helium flow cryostat where it rests on a cold finger at $T \approx 4$ K. Input laser light is sent into the device via a tapered optical fiber, which, when placed in the near-field of the device, evanescently couples to the optical resonance of the OMC [87]. The transmitted light is detected on a high-frequency photodiode (D1) connected to a real-time spectrum analyzer (RSA). We also employ an electro-optic modulator (EOM) in the laser's path to resonantly drive the mechanical resonator. Finally, we can send in a low-power, counter-propagating probe laser whose detected spectrum (D2) is fit to independently measure the mechanical amplitude and the pump-cavity detuning.

Utilizing this setup, we determine that the optical resonance is at $\lambda_c = 1542$ nm with intrinsic damping rate $\kappa_i/2\pi = 580$ MHz, giving $Q_{c,i} = 3.3\times10^5$. However, due to the large coupling to the taper, the total decay rate is $\kappa/2\pi = 1.7$ GHz, with $Q_c = 1.2\times10^5$. The mechanical mode is found to be at $\omega_m/2\pi = 3.72$ GHz damped at rate $\gamma/2\pi = 24$ kHz, with $Q_m = 1.55\times10^5$. For this experiment cryogenic temperatures are needed because the room-temperature mechanical quality-factor is much lower ($Q_m \approx 2\times10^3$), requiring such high optical powers that heating effects would obscure the signatures of the radiation-pressure nonlinearity.

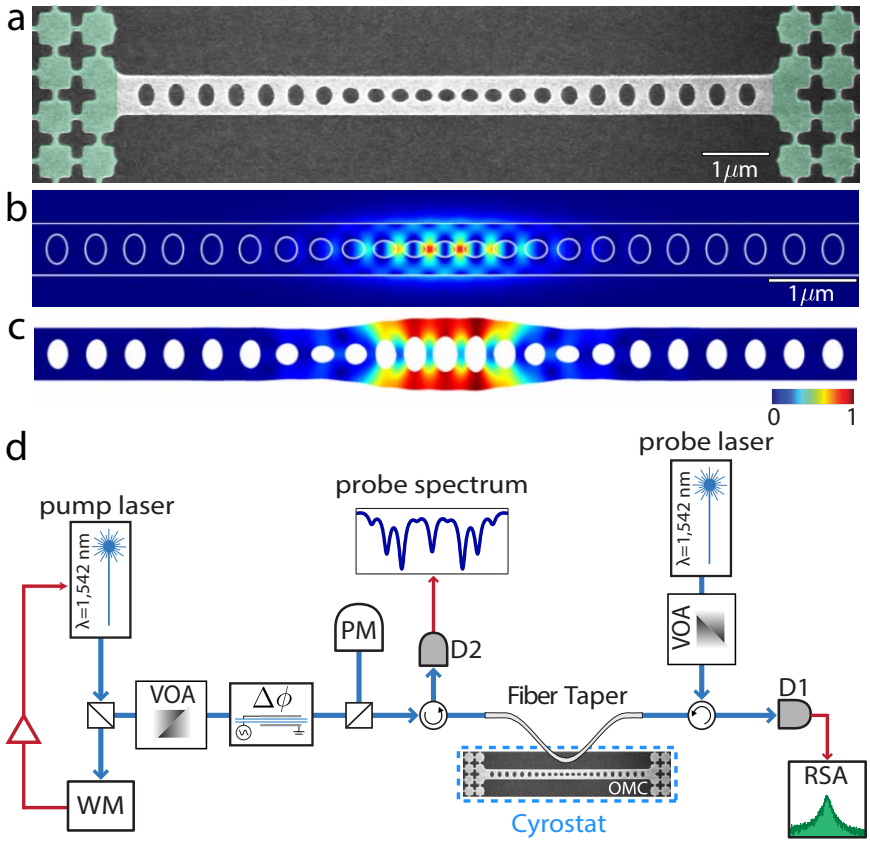

Figure 5.1: **1D OMC and Experimental Setup.** (a) SEM of the optomechanical nanobeam surrounded by phononic shield (green). (b) FEM-simulated electromagnetic energy density of first-order optical mode; white outline denotes edges of photonic crystal. (c) FEM-simulated mechanical mode profile (displacement exaggerated). In (b) the colorscale bar indicates large (red) and small (blue) energy density, whereas in (c) the scale bar indicates large (red) and small (blue) displacement amplitude. (d) Simplified schematic of experimental setup. WM: wavemeter, $\Delta\phi$: electro-optic phase modulator, OMC: optomechanical crystal, D1: pump light detector, D2: probe detector, VOA: variable optical attenuator, PM: power meter.

5.3 Theoretical Treatment

The coupling of the optical resonance frequency to the mechanical displacement yields the interaction Hamiltonian, $H_{\rm int} = \hbar g_0 \hat{a}^\dagger \hat{a} \hat{x}$, where $\hat{a}$ ($\hat{x}$) is the optical (mechanical) field amplitude, g_0 is the bare coupling rate, and $\hbar$ is Planck's constant over 2π. The physical mechanical displacement is related to the field operator by $x = x_{\rm zp}\langle\hat{x}\rangle$, where the zero-point amplitude of the resonator is $x_{\rm zp} = 2.7$ fm, using the effective motional mass as determined through FEM-simulation, $m_{\rm eff} = 311$ fg. Utilizing a calibration of the per-photon cooling power [11] we find that $g_0/2\pi = 941$ kHz. These device parameters put our system well into the sideband resolved regime $\kappa/\omega_{\rm m} \ll 1$, but far from that of single-photon strong-coupling, $g_0/\kappa \gtrsim 1$, which has not yet been achieved in optomechanics but is necessary for many quantum protocols.

The classical nonlinear optomechanical equations of motion for the mechanical displacement, x, and the optical amplitude, $a = \langle \hat{a} \rangle$, read [15]:

$$\ddot{x}(t) = -\gamma \dot{x}(t) - \omega_{\mathrm{m}}^2 x\,(t) + 2\omega_{\mathrm{m}} g_0 x_{\mathrm{zp}} |a(t)|^2 \tag{5.1}$$

$$\dot{a}(t) = \left[-\frac{\kappa}{2} + i\Delta_{\mathrm{L}} + i\frac{g_0}{x_{\mathrm{zp}}} x(t) \right] a(t) + \sqrt{\frac{\kappa_{\mathrm{e}}}{2}} a_{\mathrm{in}}, \tag{5.2}$$

where the strength of the input drive laser at frequency ω_ℓ with total power P_{in} is given by $a_{\mathrm{in}} = \sqrt{P_{\mathrm{in}}/\hbar\omega_\ell}$, which is coupled in at rate $\kappa_{\mathrm{e}}/2$, and detuned relative to the cavity frequency, ω_{c}, by $\Delta_{\mathrm{L}} = \omega_\ell - \omega_{\mathrm{c}}$.

Since we are interested in the regime of self-sustained oscillations, where the oscillator is coherent on time scales much longer than the cavity lifetime, we can take the mechanical motion to be sinusoidal with amplitude A: $x(t) = A \sin \omega_{\mathrm{m}} t$. As shown in detail in Section 1.3, this allows us to solve for the optical field:

$$a\,(t) = \sqrt{\frac{\kappa_{\mathrm{e}}}{2}} a_{\mathrm{in}} e^{i\Phi(t)} \sum_{\mathrm{n}} i^{\mathrm{n}} \alpha_{\mathrm{n}} e^{i\mathrm{n}\omega_{\mathrm{m}} t}, \tag{5.3}$$

in which we have defined the terms

$$\Phi\,(t) = -\beta_{\mathrm{m}} \cos \omega_{\mathrm{m}} t, \tag{5.4}$$

$$\alpha_{\mathrm{n}} = \frac{J_{\mathrm{n}}\,(\beta_{\mathrm{m}})}{\frac{\kappa}{2} + i\,(\mathrm{n}\omega_{\mathrm{m}} - \Delta_{\mathrm{L}})}. \tag{5.5}$$

Here J_{n} is the Bessel function of the first kind, n-th order, and its argument is the unitless modulation strength $\beta_{\mathrm{m}} = A\frac{g_0}{x_{\mathrm{zp}}\omega_{\mathrm{m}}}$. This modulation strength β is equivalent to that commonly used to characterize the strength of phase-modulation in commercial devices such as the EOM used in our setup ($\Delta\phi$ in Fig. 5.1b). For $\beta_{\mathrm{m}} \ll 1$ only the terms oscillating at the mechanical frequency, ω_{m}, are appreciable, so the interaction can be linearized, and only the first-order radiation pressure terms are present. However, for $\beta \geq 1$ the higher harmonic terms at each $\mathrm{n}\omega_{\mathrm{m}}$ have significant amplitude and also exert backaction forces which can dominate the first-order component.

The thermal amplitude is too small to observe these effects ($\beta_{\mathrm{th}} \approx 0.01$), but a laser positively detuned from the cavity, or external laser modulation, can provide amplification to drive the mechanics into the high-β regime. This leads to a rich amplitude and detuning dependent gain spectrum, which can be solved for [120] by calculating the energy lost in one mechanical cycle from friction $P_{\mathrm{fric}} = m_{\mathrm{eff}}\gamma \left\langle \dot{x}^2 \right\rangle$ and comparing it to that gained (or lost) from the optical radiation force $P_{\mathrm{rad}} = \hbar\frac{g_0}{x_{\mathrm{zp}}} \left\langle |\hat{a}|^2 \dot{x} \right\rangle$ across a sweep of amplitude/detuning pairs $(\beta_{\mathrm{m}}, \Delta_{\mathrm{L}})$.

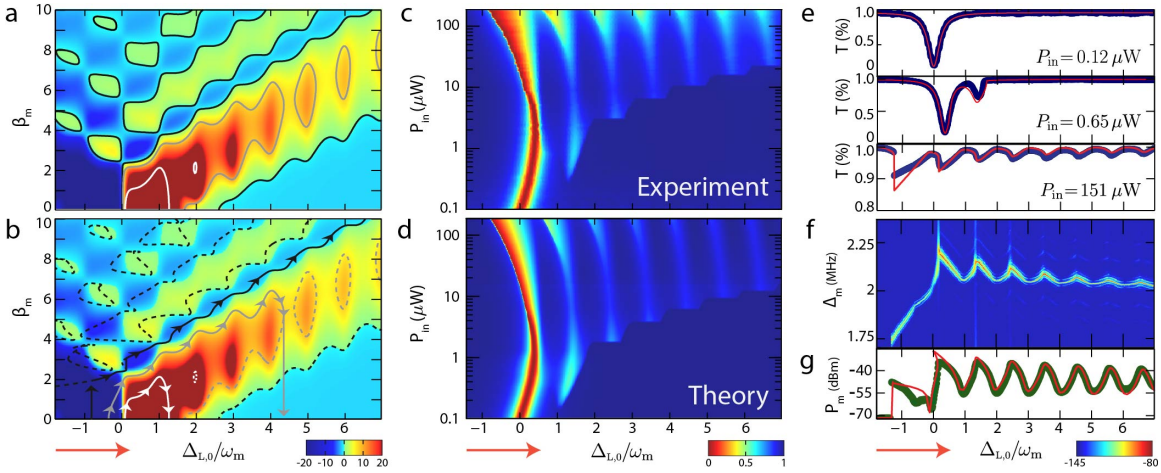

Figure 5.2: **OMC Gain Diagram and Transmission Spectra.** (a) Calculated gain spectrum for the OMC in the amplitude-detuning plane. Color scale indicates ratio of power input to that lost from friction ($P_{\rm rad}/P_{\rm fric}-1$) at $P_{\rm in}=151$ μW. Positive values are regions of mechanical self-oscillation. Curves indicate power-conserving solution contours at selected input powers: 0.65 μW (white), 6.5 μW (grey), 151 μW (black). (b) same as (a), with contours now shifted by estimated thermo-optic effects, where solid lines indicate the path taken by the mechanical oscillator during laser sweep for same powers as in (a). Dashed lines are contours which are either unstable or unreachable by a slow sweep of laser detuning. Red arrows indicate direction of laser scan. (c) Plot of device transmission spectrum for a series of laser powers. Scans are scaled at each power to span the range $0-1$. Stair-step shape indicates onset of self-oscillation due to progressively higher-order sidebands. (d) Theoretical calculation of (c), with the optical cavity shift per-photon, $c_{\rm to}$, as the only free parameter. (e) Plots of normalized transmission scans as in (c) at $P_{\rm in}=0.12$ μW (top), 0.65 μW (center), 151 μW (bottom), (blue data) with theoretical curve overlaid (red). (f) Power spectral density of detected signal near the mechanical frequency for $P_{\rm in}=151$ μW, showing frequency shifts of the mechanical mode, $\Delta_{\rm m}$, from its bare frequency, $\omega_{\rm m}/2\pi=3.72$ GHz. Color scale is detected power density in dBm/Hz. (g) Total integrated power of spectra in (f), green circles, with theoretical model (red curve). An over-all scale-factor is the only free parameter. Due to a small drift in the center frequency of the optical cavity, the highest power scan in (e) and corresponding scans in (f)-(g) are red-shifted relative to the same power in (c)-(d).

This calculation for our system parameters generates the plot shown in Fig. 5.2a, where the color indicates the ratio of these terms (more precisely, $P_{\rm rad}/P_{\rm fric}-1$) at a laser input power of $P_{\rm in}$ =151 μW. Finally, imposing energy conservation, $P_{\rm rad}/P_{\rm fric}=+1$, allows us to solve for the steady-state solution contours as shown in Fig. 5.2a. Although the entire contour is a physical solution, the equilibrium is only stable when the power ratio decreases upon increasing the mechanical amplitude, $\frac{\partial}{\partial\beta}\frac{P_{\rm rad}}{P_{\rm fric}}<0$ (i.e., stability is found at the 'tops' of the contours) [120]. It is seen that at the highest powers (Fig. 5.2a, black curve) for most detunings there are multiple possible mechanical amplitude solutions, $\beta_{\rm m}$.

In our device, there is also a small frequency shift of the optical cavity caused by heating due to material absorption of the intracavity photons. This heating is slow relative to the other time-scales in the system, but fast compared to our laser scan speed, so we can model it as an effective blue-shift

of our detuning proportional to $\Delta_{L,0} = \Delta_L - c_{to}\bar{n}_a$, where the per photon thermo-optic frequency shift of the optical cavity is measured to be $c_{to}/2\pi = -216$ kHz, and $\bar{n}_a$ is the estimated average photon number [11] for each (β_m, Δ_L). Including this effect, the shifted contours are shown in Fig. 5.2b for their respective input powers. The solid lines with arrows indicate the expected path traversed by the mechanical resonator during a slow (adiabatic) laser scan from lower to higher laser frequency (left to right) at each power. The dashed lines are contours that are either unstable, or unreachable by this adiabatic laser sweep.

5.4 Main Results

5.4.1 Traversing the Lowest Contour

We first explore the attractor diagram by measuring the system dynamics as the oscillator traverses this lowest-lying contour for a range of powers. Since we are monitoring the transmission of a double-sided optical cavity, a dip in transmission is seen when scanning through the cavity resonance, indicating that light is entering the cavity and being lost to absorption or scattering. At low powers one sees a single dip ($P_{in} < 0.3$ μW, in Fig. 5.2c and top plot in Fig. 5.2e). Upon increasing the laser power, optomechanical dynamical backaction effects start to drive the system, and beyond threshold there is self-oscillation of the mechanical element. When this occurs, a large fraction of the optical photons are now scattered, which results in a second dip of the transmission near the first mechanical sideband ($\Delta_{L,0}/\omega_m = 1$) in Fig. 5.2c. As the power is increased, the self-oscillation threshold is achieved for detunings at progressively higher mechanical sidebands, $\Delta = n\omega_m$, resulting in the stair-step behavior observed in the transmission. Physically, mechanical oscillations at the n-th sideband detuning are generated by a gain process involving n photon-phonon scattering events. As mentioned, the overall red-shift of the curves at the highest powers is due to the thermo-optic effect. We present our theoretically expected transmission spectra in Fig. 5.2d and find good agreement.

More information about the state of the mechanical oscillator can be gained by recording the spectrum of the signal near the mechanical frequency, as shown in Fig. 5.2f, for the highest power transmission scan of Fig. 5.2e. We note that backaction effects blue-shift the resonator frequency by an appreciable amount of about 2 MHz from its intrinsic value of $\omega_m/2\pi = 3.7$ GHz. This frequency shift (Δ_m) depends on the laser detuning in a more intricate fashion than a linear calculation of the optical spring effect would suggest. A measure of oscillation amplitude can be extracted from the total power in this mechanical sideband, and its dependence on detuning is shown in Fig. 5.2f. Although the mechanical amplitude β_m increases monotonically with detuning, we observe that the total transduced power oscillates due to the nonlinearity of the detection process. All of these observations are nicely captured by our theoretical prediction (Fig. 5.2g, red curve). This has been obtained without fit parameters, except for an over-all scale factor in Fig. 5.2g. This agreement

allows us to conclude that the oscillator is indeed traveling along the predicted paths through the attractor diagram shown in Fig. 5.2b.

5.4.2 Time Domain Switching

We have also investigated the time domain behavior of the system near one of the transition points in the highest power transmission scan of Fig. 5.2e. At this power, due to the thermo-optic shift of the optical cavity, there exist two stable solution amplitudes on the same contour line (black contour, Fig. 5.2b) near $\Delta_{\mathrm{L},0} = 0$. In Fig. 5.3a we show a quick transmission scan across the optical cavity taken at $P_{\mathrm{in}} = 152\ \mu$W (blue curve). Overlaid upon that quick scan we show the DC transmission (red curve) in the region over which we stepped the laser and recorded 2.5 s of time domain data at each point. We use our RSA to record both quadratures (I & Q) of the time-varying voltage coming from the detector. The instrument measures these quadratures by mixing the incoming signal with carrier at $\omega_{\mathrm{car}}/2\pi = 3.727$ GHz and filtering the resulting signal over a bandwidth of $\Delta_{\mathrm{BW}} = 2.56$ MHz. This has the effect of shifting frequencies at ω down to $\omega - \omega_{\mathrm{car}}$. Thus, by setting $\omega_{\mathrm{car}} \approx \omega_{\mathrm{m}}$ we are able to record the time domain transmission amplitude of signal near the mechanical frequency with a sampling frequency significantly less than the mechanical frequency $\Delta_{\mathrm{BW}} \ll \omega_{\mathrm{m}}$. Thus, we represent the amplitude of this mixed down signal as $\mathrm{T}|_{\omega_{\mathrm{m}}}$ in the y-axis of Fig. 5.3b.

In the color plot of Fig. 5.3b we show the amplitude distribution (histogram) of the recorded signal $\mathrm{T}|_{\omega_{\mathrm{m}}}$ at each detuning point over the range shown in red in Fig. 5.3a. The distribution is normalized at each detuning such that the sum of the elements is unity. Of interest is the range $\Delta_{\mathrm{L},0}/\omega_{\mathrm{m}} = 1.15 - 1.21$ where there are two distinct maxima. This indicates that in this region the oscillator is switching between two distinct amplitude states.

We can gain more knowledge of the behavior of the system by considering the amplitude distribution of the two quadratures of the detected signal. This data is shown for a range of detunings in Fig. 5.4. A coherent state is one with a well-defined non-zero amplitude, but a varying phase, and thus would show up in this I.Q. plot as a ring. In contrast, a thermal state would show up on the plot as a 2D gaussian distribution with its maximum centered at the origin. From these plots, then, it is clear that the two states which the amplitude is vacillating between are both coherently driven states and not simply thermal states of different amplitude (i.e., different temperatures). The width of the rings indicates the relative amplitude noise on each state. Interestingly, this amplitude noise does not seem to be significanytly different in the bistable regime as in the single-state regime.

An example of the telegraph-like switching behavior of the mechanical oscillator is shown in the temporal signal in Fig. 5.5a (blue curve). At this detuning, it is seen that the oscillator is spending most of its time in the higher-amplitude state and only dropping into the lower state for brief periods. For reference, we have included in this plot a normalized plot of the state switching

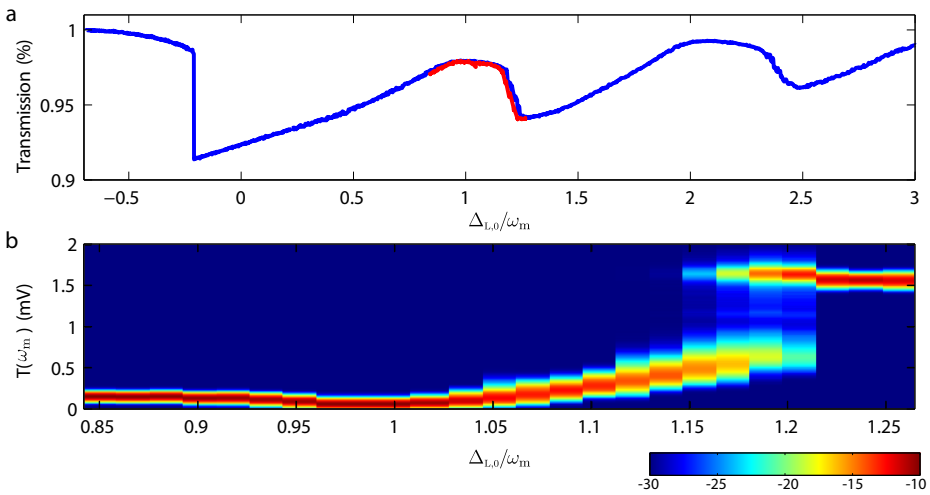

Figure 5.3: **Bistable Hopping.** (a) Normalized transmisison spectrum of the device at $P_{\rm in} = 152\ \mu$W (blue data), with region over which time domain data was recorded shown as red curve. (b) Histogram of total transmitted signal near the mechanical frequency $\mathrm{T}|_{\omega_{\rm m}}$ in mV, versus detuning in the indicated region of (a). Color scale indicates in dB-scale the fractional occupation time during approximately 2.5s of recorded temporal data (i.e., sum of all probabilities is unity). Bistable switching region is indicated by two distinct amplitude peaks (near $\Delta_{\rm L,0}/\omega_{\rm m} = 1.2$).

events, extracted from the blue curve with a thresholding algorithm (red curve). Taking the fourier transform of this signal yields the spectral content as shown in Fig. 5.5b. The dominant peak near 18kHz (and its harmonics) indicates this is the approximate switching frequency of the oscillator. However, there is significant variance on this rate which shows up as sidebands around the main peak. The way the signal harmonics repeat at each n × 18 kHz is characteristic of 'telegraph' switching noise. Although we have not done this analysis, it would in principle be possible to use this switching rate to estimate the noise in the optomechanical system given the known potential well-depth of the two distinct states (see [120]).

5.4.3 Reaching the Lonely Island

It is readily apparent from Fig. 5.2a that at large optical powers (black contour) there are a large number of isolated attractor contours at higher oscillation amplitudes. These attractors cannot be reached by slowly sweeping the detuning of the laser because the contours do not reach down to zero amplitude, nor can they be reached by noise, since the potential barriers are too high for the present parameters. However, external time-dependent driving of the mechanical mode allows us to access and explore the lowest-lying isolated attractor on the red side of the optical cavity ($\Delta_{\rm L} < 0$), where the linearized theory predicts only damping of the mechanical mode.

To access this higher island, we use our EOM to phase-modulate the incoming light field. The resulting oscillating force inside the cavity drives the mechanical resonator towards higher amplitudes

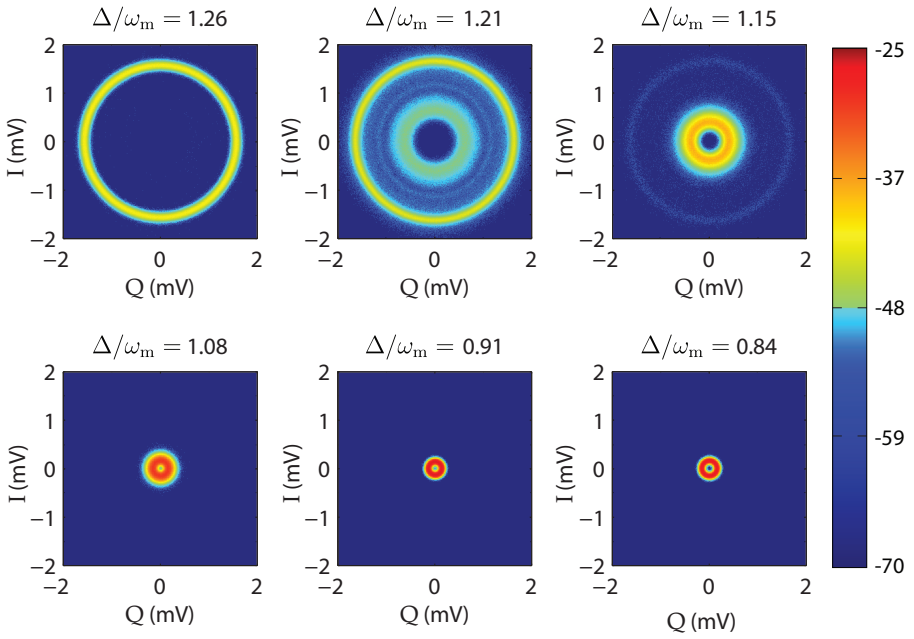

Figure 5.4: **Quadrature Plots.** Phase-space density plots of the $\mathrm{I}(t)\,,\mathrm{Q}(t)$ quadratures of the detected signal near the mechanical frequency, $\mathrm{T}|_{\omega_\mathrm{m}}$, with laser detuning indicated above each plot. Color scale indicates in dB-scale the fractional occupation time during approximately 2.5s of recorded temporal data (i.e., sum of all probabilities is unity), as in Fig. 5.3. The distinct reduction in probability density near $\mathrm{I},\mathrm{Q}=0$ indicates a non-thermal driven state.

($\beta_\mathrm{m} > 1$). In this driven regime, the external forcing induces injection-locking, i.e., the mechanical oscillator becomes synchronized to that of the drive. The resulting increase of oscillation amplitude can be exploited for control of the system dynamics.

The experimental procedure is displayed in Fig. 5.6a and the corresponding gain spectrum with its stable contours at the power used ($P_\mathrm{in} = 43\ \mu\mathrm{W}$) is shown in Fig. 5.6b. We start with the pump laser switched on, but the phase modulation off ($\beta_\mathrm{EOM} = 0$) at a detuning on the red side of the cavity resonance. Here, the laser acts to damp the mechanical resonator into a low-amplitude (cooled) thermal state: $\beta_\mathrm{m} \approx 0$. Then, we switch on the EOM phase modulation, which rings up the mechanical resonator (shown in time domain inset of Fig. 5.6a). We now sweep the detuning to some starting value, Δ_L, completing the initialization sequence. Finally, we switch off the modulation ($\beta_\mathrm{EOM} \to 0$) and record what final stable state the system relaxes into.

To get a measure of the initial/final mechanical oscillation amplitude, β_m, we send in an additional counter-propagating weak probe beam and scan it across the optical cavity to measure the cavity transmission spectrum during each period of the sequence, as shown in the panels of Fig. 5.6d. When the mechanical amplitude is large ($\beta_\mathrm{m} \gtrsim 1$) the standard single-dip optical cavity is modified to a multi-featured spectrum symmetric about the cavity center with dips of varying sizes near each mechanical sideband at $\Delta_\mathrm{p} = \pm\mathrm{n}\omega_\mathrm{m}$. The varying relative amplitudes of these peaks allow us

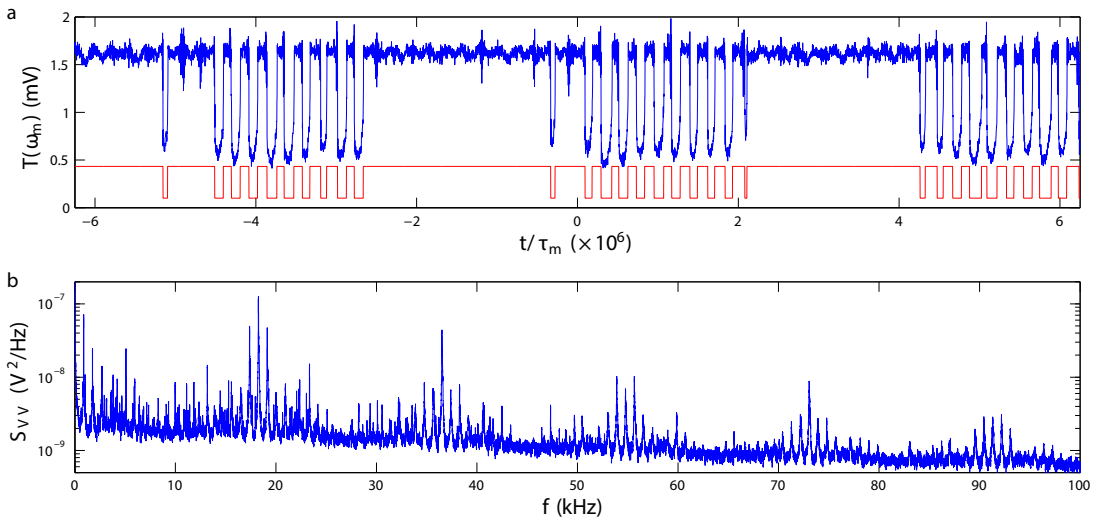

Figure 5.5: **Time Domain Data and Switching.** (a) time domain of signal amplitude detected at the mechanical frequency $T|_{\omega_m}$ (blue curve) showing bi-stable switching behavior at a detuning of $\Delta_{L,0}/\omega_m = 1.21$ (see top center panel of Fig. 5.4). For clarity, red curve shows a reconstructed signal of on/off switching events. Time axis is in units of the mechanical period indicating that these switches are slow relative to the mechanical oscillation frequency. (b) Fourier-transform on all 2.5s of recorded data at this detuning, main signal peak near 18kHz indicates switching rate, however the noise on this rate causes many additional sidebands to be present. Telegraph-signal harmonics of main peak are evident at 18kHz intervals.

to precisely infer β_m without relying on calibration of the total detected power. We thus fit this spectrum to a theoretical curve calculated using Eq. (5.3) with β_m and ω_c as the free parameters (Fig. 5.6d, red curves). With our wavemeter independently establishing ω_ℓ, from this fit we also know the true detuning of the drive laser, Δ_L (as opposed to using $\Delta_{L,0}$ as in Fig. 5.2).

We repeated this experimental procedure several times for different initial (β_m, Δ_L) states and recorded the resulting final states, which reveal the flow in the underlying attractor diagram. We have plotted a representative subset of our results in Fig. 5.6f. We find that after the modulation is switched off, for a narrow range of initial conditions the system remains trapped close to the predicted top of the higher amplitude attractor at $(\beta_m \approx 3.5, \Delta_L/2\pi \approx 0.7)$. For more negative initial detunings or lower initial mechanical amplitudes, the system relaxes into the trivial low-amplitude state, or gets caught on the lowest-lying contour explored in Fig. 5.2. For detunings beyond $\Delta_L/\omega_m > -0.5$, the system could not be stably initialized due to thermo-optic effects.

5.5 Conclusion

An understanding of these effects as presented here paves the way to exploiting them for use in metrology experiments. The dynamics that govern whether the oscillator stably latches into an

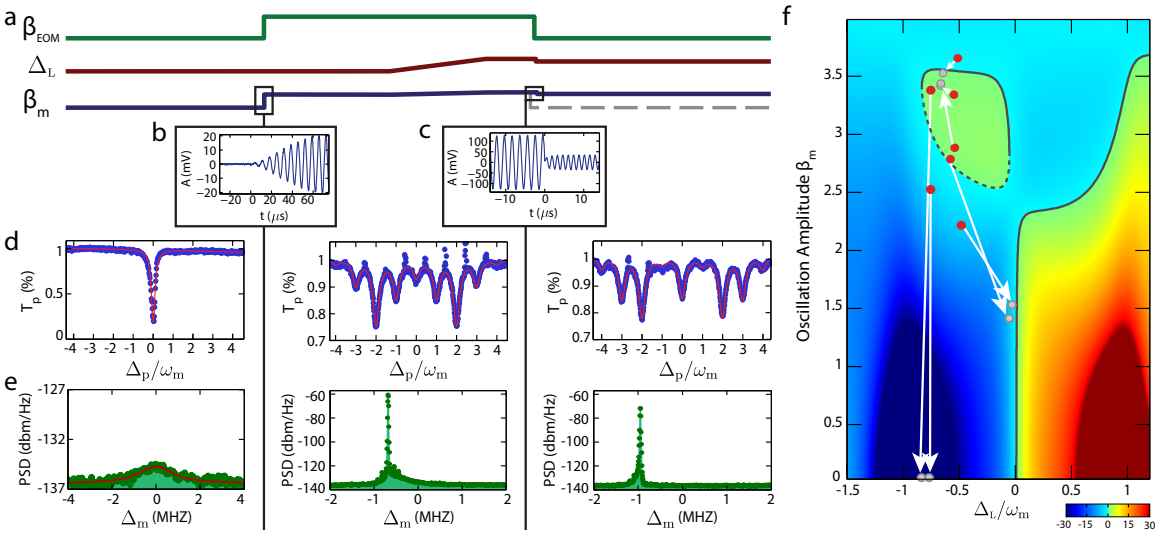

Figure 5.6: **Initializing into Isolated Attractor.** (a) Schematic of state preparation scheme including change in the two control parameters, modulation drive strength ($\beta_{\rm EOM}$), and laser-cavity detuning ($\Delta_{\rm L}$), along with the resulting oscillator amplitude ($\beta_{\rm m}$). (b) Time-signal of one quadrature of detected mechanical amplitude during the turn-on of the EOM drive at $t = 0$, showing amplitude ring-up. For clarity, the signal is mixed down from the mechanical frequency carrier at 3.7 GHz to 150 kHz. (c) same as (b) with modulation turned off at $t = 0$ for a case where the system remained trapped in high-amplitude state; carrier mixed down to 500 kHz. (d) Transmission scans of the low-power probe laser (blue data points) with with the fit curves (red) used to extract $(\beta_{\rm m}, \Delta_{\rm L})$ during each period of sequence, $\Delta_{\rm p} = \omega_{\rm p} - \omega_{\rm c}$ with $\omega_{\rm p}$ the probe frequency. (e) Mechanical power spectrum (green data) near the mechanical frequency during these periods. In the left panel the resonator is in a cooled thermal state and the red-line is a fit used to extract mechanical parameters. (f) Plot of the normalized gain spectrum in the detuning-amplitude plane with overlaid stable solution contour (black solid curve) at $P_{\rm in} = 43$ μW. Color scale is $(P_{\rm rad}/P_{\rm fric} - 1)$. Dashed black curve indicates unstable portion of contour. Red data points indicate initial $(\beta_{\rm m}, \Delta_{\rm L})$ and grey data points indicate the final values, for selected instances of the experimental sequence as shown in (a). White arrows connect initial/final pairs but do not indicate the actual path taken by the system.

attractor can be a very sensitive function of the oscillator's displacement [120], thus yielding a precise measurement of the oscillator's environment or state. This latching also allows for systems with memory due to the hysteretic nature of the nonlinearity, as in Ref. [128]. Such latching behavior has also been predicted [131] and observed in Josephson junctions [132, 133] and arrays of SQUIDs [134].

These results represent the first exploration of the nonlinear attractor diagram observed in an optomechanical system where the dominant nonlinearity is that of the radiation pressure interaction. Here, we used external control to initialize the oscillator into an otherwise isolated stable attractor. We were limited to exploring only this particular red-side attractor by our driving EOM, which could only achieve $\beta_{\rm EOM} \lesssim 3.5$. With the ability to apply larger drives, or to rapidly detune our laser, it should be possible to reach higher-lying islands, and more fully explore the attractor diagram shown in Fig. 5.2a. Since the intracavity photon number is lower in these higher-order attractors, experiments in this regime would be less affected by the unwanted thermo-optic shifts observed here.

In future devices where the optomechanical coupling rate is larger, these same nonlinearities can lead to exciting quantum effects which have been explored theoretically [135].

Appendix A

Mathematical Definitions

A.1 Fourier Transforms and Spectral Densities

$$
\begin{aligned}
\hat{A}(t) &= \frac{1}{\sqrt{2\pi}} \int_{-\infty}^{\infty} d\omega e^{-i\omega t} \hat{A}(\omega) \\
\hat{A}(\omega) &= \frac{1}{\sqrt{2\pi}} \int_{-\infty}^{\infty} dt e^{i\omega t} \hat{A}(t) \\
\hat{A}^{\dagger}(\omega) &= \frac{1}{\sqrt{2\pi}} \int_{-\infty}^{\infty} dt e^{i\omega t} \hat{A}^{\dagger}(t) \\
\left(\hat{A}(\omega)\right)^{\dagger} &= \hat{A}^{\dagger}(-\omega) \\
S_{AA}(\omega) &= \int_{-\infty}^{\infty} d\tau e^{i\omega\tau} \langle \hat{A}^{\dagger}(t+\tau)\hat{A}(t)\rangle \\
S_{AA}(\omega) &= \int_{-\infty}^{\infty} d\omega' \langle \hat{A}^{\dagger}(\omega)\hat{A}(\omega')\rangle
\end{aligned}
\tag{A.1}
$$

Appendix B

Homodyne Reflection Optomechanical Spectroscopy

In this section we derive the relevant equations for balanced homodyne detection [136] and at the end derive the form and magnitude of our feedback modulated photon number. We start by writing down the field quadratures of both our signal (s) and our local oscillator (LO) laser beams:

$$\alpha_{\rm s}(t) = X_{\rm s}(t) + iY_{\rm s}(t) \tag{B.1}$$

$$\alpha_{\rm LO}(t) = \left[|\alpha_{\rm LO}| + \delta X_{\rm LO}(t) + i\delta Y_{\rm LO}(t)\right] e^{i\theta_{\rm h}}, \tag{B.2}$$

where we have written the local oscillator as a large steady state value $|\alpha_{\rm LO}|$ with small modulations in its two quadratures (where $|\alpha_{\rm LO}|^2 = P_{LO}/\hbar\omega_\ell$) and $X_{\rm s}(t), Y_{\rm s}(t), \delta X_{\rm LO}(t), \delta Y_{\rm LO}(t)$ are all real valued. We have also included an overall phase factor $\theta_{\rm h}$ between the LO and signal arms because we will see this is a critical parameter in measuring the mechanical displacements. These two beams are mixed on a beamsplitter and the output is sent to two detectors whose voltage outputs are subtracted. The reflected path of the beamsplitter picks up an extra π phase shift due to the reflection:

$$\alpha_{D1} = \sqrt{\frac{1}{2}}\alpha_{\rm LO}(t) + \sqrt{\frac{1}{2}}\alpha_{\rm s}(t), \tag{B.3}$$

$$\alpha_{D2} = \sqrt{\frac{1}{2}}\alpha_{\rm LO}(t) - \sqrt{\frac{1}{2}}\alpha_{\rm s}(t). \tag{B.4}$$

The detected voltage is proportional to the difference of the measured output currents $I_{1,2} = |\alpha_{D1,2}|^2$, which after multiplying out and subtracting, gives

$$I_- = I_1(t) - I_2(t) = \alpha_{\rm LO}(t)\alpha_{\rm s}^*(t) + \alpha_{\rm LO}^*(t)\alpha_{\rm s}(t). \tag{B.5}$$

Plugging in the quadratures for α_{LO} and α_{s}, using Eqs. B.1 and B.2, and taking $|\alpha_{\mathrm{LO}}|^2 \gg |\alpha_{\mathrm{s}}|^2$, we find

$$\begin{aligned} I_-(t) &= |\alpha_{\mathrm{LO}}| e^{i\theta_{\mathrm{h}}} \left(X_{\mathrm{s}}(t) - iY_{\mathrm{s}}(t)\right) + |\alpha_{\mathrm{LO}}| e^{-i\theta_{\mathrm{h}}} \left(X_{\mathrm{s}}(t) + iY_{\mathrm{s}}(t)\right) \\ &= 2|\alpha_{\mathrm{LO}}| \left[\cos\theta_{\mathrm{h}} X_{\mathrm{s}}(t) + \sin\theta_{\mathrm{h}} Y_{\mathrm{s}}(t)\right]. \end{aligned} \tag{B.6}$$

And now we plug into the signal field our solution of the optical reflected field in steady state $\alpha_{\mathrm{s}} \Rightarrow \hat{a}_{\mathrm{out}}^{\mathrm{ss}}$ from Eq. (1.19):

$$\alpha_{\mathrm{s}} = a_{\mathrm{out}}^{\mathrm{ss}} = a_{\mathrm{in}} \left(1 - \frac{\kappa_{\mathrm{e}}}{\frac{\kappa}{2} - i\Delta}\right) = a_{\mathrm{in}} \left(1 - \frac{\kappa_{\mathrm{e}}\kappa}{2\left(\Delta^2 + \left(\frac{\kappa}{2}\right)^2\right)} + \frac{-i\Delta\kappa_{\mathrm{e}}}{\Delta^2 + \left(\frac{\kappa}{2}\right)^2}\right), \tag{B.7}$$

where we have dropped the hats ($\hat{}$) to indicate this treatment of the optical field is classical. Now, we separate the signal field into its quadratures:

$$X_{\mathrm{s}} = a_{\mathrm{in}} \left(1 - \frac{\kappa_{\mathrm{e}}\kappa}{2\left(\Delta^2 + \left(\frac{\kappa}{2}\right)^2\right)}\right), \tag{B.8}$$

$$Y_{\mathrm{s}} = a_{\mathrm{in}} \frac{-\Delta\kappa_{\mathrm{e}}}{\Delta^2 + \left(\frac{\kappa}{2}\right)^2}. \tag{B.9}$$

These are the phase and amplitude quadratures of the light field, not to be confused with the quadratures of our mechanics. The mechanical resonator modulates the cavity frequency to first order as $\omega_{\mathrm{c},0}(t) = \omega_{\mathrm{c},0} + x(t)g_{\mathrm{OM}}$, which means that we can find the modulation of our light field quadratures by taking derivatives with respect to the detuning, Δ, defined previously,

$$\frac{dX_{\mathrm{s}}}{d\Delta} = a_{\mathrm{in}} \frac{\kappa_{\mathrm{e}}\kappa\Delta}{\left(\Delta^2 + \left(\frac{\kappa}{2}\right)^2\right)^2}, \tag{B.10}$$

$$\frac{dY_{\mathrm{s}}}{d\Delta} = a_{\mathrm{in}} \left[\frac{-\kappa_{\mathrm{e}}}{\left(\Delta^2 + \left(\frac{\kappa}{2}\right)^2\right)} + \frac{2\kappa_{\mathrm{e}}\Delta^2}{\left(\Delta^2 + \left(\frac{\kappa}{2}\right)^2\right)^2}\right]. \tag{B.11}$$

If one sets the laser directly on the center of the optical cavity, $\Delta = 0$, one finds,

$$\frac{dX_{\rm s}}{d\Delta} = 0 \tag{B.12}$$

$$\frac{dY_{\rm s}}{d\Delta} = a_{\rm in}\frac{-4\kappa_{\rm e}}{\kappa^2}. \tag{B.13}$$

So, to first order, only the $Y_{\rm s}$ quadrature contains the mechanical motion, and looking at Eq. (B.6), we see this detection is maximized at $\theta_{\rm h} = \pi/2$. Our detected signal is then,

$$\frac{dI_-}{d\Delta}|_{\Delta=0} = -2\,|\alpha_{\rm LO}|\,a_{\rm in}\frac{4\kappa_{\rm e}}{\kappa^2}. \tag{B.14}$$

Note that maintaining the optimal phase, $\theta_{\rm h} = \pi/2$, between the arms of the homodyne setup is an important experimental concern (see Section 4.6.1 for more details). Also, note that in a direct detection scheme, the detected signal would be proportional to $|a_{\rm in}|^2$, thus we can think of the homodyne detection scheme as providing amplification proportional to $\frac{|\alpha_{\rm LO}|}{|a_{\rm in}|}$. This is an important technique which allows signals to be amplified until the vacuum noise of the signal port dominates the noise floor of the detector as done in this work. From here, we can substitute the number of photons in the optical cavity, $n_{\rm c}$ into Eq. (B.14). The number of photons in the optical cavity is given by

$$n_{\rm c} = \langle \hat{a}^\dagger_{ss}\hat{a}_{ss}\rangle = \frac{\kappa_{\rm e}}{\Delta^2 + \frac{\kappa^2}{4}}|a_{\rm in}|^2. \tag{B.15}$$

Now the magnitude of the signal field can be solved for in terms of $n_{\rm c}$ and plugged into Eq. (B.14):

$$|a_{\rm in}| = \sqrt{n_{\rm c}|_{\Delta=0}}\sqrt{\frac{\kappa^2}{4\kappa_{\rm e}}}, \tag{B.16}$$

$$\left|\frac{dI_-}{d\Delta}\right|_{\Delta=0} = -2\,|\alpha_{\rm LO}|\,\sqrt{n_{\rm c}}\sqrt{\frac{4\kappa_{\rm e}}{\kappa^2}}, \tag{B.17}$$

where we have simplified, $n_{\rm c} \equiv n_{\rm c}|_{\Delta=0}$. The transduced optical power from the mechanical motion is given by

$$P_{\rm m}(\omega) = \hbar\omega_\ell\left|\frac{dI_-}{dx}\right|\sqrt{\eta}x(\omega) = \hbar\omega_\ell\left|\frac{dI_-}{d\Delta}\right|\left|\frac{d\Delta}{dx}\right|\sqrt{\eta}x(\omega) = \hbar\omega_\ell\left|\frac{dI_-}{d\Delta}\right|g_{\rm OM}\sqrt{\eta}\langle x(\omega)\rangle. \tag{B.18}$$

Here, η, is the loss in the signal arm from the cavity to the detector. From this detected mechanical

power with the laser on resonance, ($\Delta = 0$), we can get the magnitude of the voltage output of the derivative feedback circuit, $V_{\rm fb}$, which is proportional to ω and includes some electrical circuit response, $g_{\rm e} = |g_{\rm e}(\omega)|$, in units of V/W:

$$|V_{\rm fb}(\omega)| = g_{\rm e} P_{\rm m}(\omega) = 2 g_{\rm e} \hbar \omega_\ell \, |\alpha_{\rm LO}| \, \sqrt{n_{\rm c}} \sqrt{\frac{4\kappa_{\rm e}}{\kappa^2}} g_{\rm OM} \sqrt{\eta} \langle x(\omega) \rangle. \tag{B.19}$$

This feedback voltage is sent to an intensity modulator which, as long as the applied voltages are not too large, linearly changes the optical power. For a given input voltage, the intensity modulator changes the optical power emitted by the fraction $V_{\rm in}\pi/V_\pi$, where V_π is the voltage needed to go from maximum transmision to total extinction of the outgoing light in the electro-optic modulator. The number of photons in the cavity will change by the same fraction. Therefore, we can write the following expression for $n_{\rm mod}$:

$$|n_{\rm mod}| = n_{\rm c} |V_{\rm fb}(\omega)| \frac{\pi}{V_\pi} = \frac{2 g_e \hbar \omega_\ell \, |\alpha_{\rm LO}| \, \sqrt{\frac{4\kappa_{\rm e}}{\kappa^2}} g_{\rm OM} \sqrt{\eta} \pi}{V_\pi} \langle x(\omega) \rangle n_{\rm c}^{\frac{3}{2}}. \tag{B.20}$$

This expression is employed in (Section 4.3) to show that for fixed loop-gain, we expect our homodyne feedback cooling to increases with $n_c^{\frac{3}{2}}$ (as observed in Fig. 4.9).

Appendix C

Publications

1. A. G. Krause, T. D. Blasius, and O. Painter, "Optical feedback cooling of a photonic crystal optomechanical resonator," *In preparation*.

2. A. G. Krause, J. T. Hill, M. Ludwig, A. Safavi-Naeini, J. Chan, F. Marquardt, and O. Painter, "Controlling nonlinear dynamics in an optomechanical crystal," *In preparation*.

3. A. G. Krause, M. Winger, T. D. Blasius, Q. Lin, and O. Painter, "A high-resolution microchip optomechanical accelerometer," *Nature Photonics* **6**, 768–772 (2012).

4. A. H. Safavi-Naeini, J. Chan, J. T. Hill, T. P. M. Alegre, A. Krause, and O. Painter, "Observation of quantum motion of a nanomechanical resonator," *Phys. Rev. Lett.* **108**, 033602 (2012).

5. J. Chan, T. P. M. Alegre, A. H. Safavi-Naeini, J. T. Hill, A. Krause, S. Gröblacher, M. Aspelmeyer, and O. Painter, "Laser cooling of a nanomechanical oscillator into its quantum ground state," *Nature* **478**, 89–92 (2011).

Bibliography

[1] T. J. Kippenberg and K. J. Vahala, "Cavity Optomechanics: Back-Action at the Mesoscale," *Science* **321**, 1172–1176 (2008).

[2] J. T. Hill, *Nonlinear optics and wavelength translation via cavity-optomechanics*, phd, California Institute of Technology (2013).

[3] J. D. Thompson, B. M. Zwickl, A. M. Jayich, F. Marquardt, S. M. Girvin, and J. G. E. Harris, "Strong dispersive coupling of a high-finesse cavity to a micromechanical membrane," *Nature* **452**, 72–75 (2008).

[4] A. M. Jayich, J. C. Sankey, B. M. Zwickl, C. Yang, J. D. Thompson, S. M. Girvin, A. A. Clerk, F. Marquardt, and J. G. E. Harris, "Dispersive optomechanics: a membrane inside a cavity," *New J. Phys.* **10**, 095008 (2008).

[5] A. Nunnenkamp, K. Brkje, J. G. E. Harris, and S. M. Girvin, "Cooling and squeezing via quadratic optomechanical coupling," *Phys. Rev. A* **82**, 021806 (2010).

[6] A. A. Clerk, F. Marquardt, and J. G. E. Harris, "Quantum Measurement of Phonon Shot Noise," *Phys. Rev. Lett.* **104**, 213603 (2010).

[7] J. T. Hill, Q. Lin, J. Rosenberg, and O. Painter, "Mechanical Trapping in a Quadratically Coupled Optomechanical Double Disk," in *CLEO:2011 - Laser Applications to Photonic Applications* (Optical Society of America, 2011).

[8] M. Vanner, "Selective Linear or Quadratic Optomechanical Coupling via Measurement," *Phys. Rev. X* **1**, 021011 (2011).

[9] A. Xuereb and M. Paternostro, "Selectable linear or quadratic coupling in an optomechanical system," *Phys. Rev. A* **87**, 023830 (2012).

[10] H. Shi and M. Bhattacharya, "Quantum mechanical study of a generic quadratically coupled optomechanical system," *Phys. Rev. A* **87**, 043829 (2013).

[11] J. Chan, T. P. M. Alegre, A. H. Safavi-Naeini, J. T. Hill, A. Krause, S. Gröblacher, M. Aspelmeyer, and O. Painter, "Laser cooling of a nanomechanical oscillator into its quantum ground state," *Nature* **478**, 89–92 (2011).

[12] A. D. O'Connell, M. Hofheinz, M. Ansmann, R. C. Bialczak, M. Lenander, E. Lucero, M. Neeley, D. Sank, H. Wang, M. Weides, J. Wenner, J. M. Martinis, and A. N. Cleland, "Quantum ground state and single-phonon control of a mechanical resonator," *Nature* **464**, 697–703 (2010).

[13] J. D. Teufel, T. Donner, D. Li, J. W. Harlow, M. S. Allman, K. Cicak, A. J. Sirois, J. D. Whittaker, K. W. Lehnert, and R. W. Simmonds, "Sideband cooling of micromechanical motion to the quantum ground state," *Nature* **475**, 359–363 (2011).

[14] K. Srinivasan, *Semiconductor optical microcavities for chip-based cavity QED*, phd, California Institute of Technology (2006).

[15] M. Aspelmeyer, T. J. Kippenberg, and F. Marquardt, "Cavity Optomechanics," *arXiv:1303.0733* (2013).

[16] A. Butsch, C. Conti, F. Biancalana, and P. S. Russell, "Optomechanical Self-Channeling of Light in a Suspended Planar Dual-Nanoweb Waveguide," *Physical Review Letters* **108**, 093903 (2012).

[17] A. H. Safavi-Naeini, J. Chan, J. T. Hill, T. P. M. Alegre, A. Krause, and O. Painter, "Observation of Quantum Motion of a Nanomechanical Resonator," *Physical Review Letters* **108**, 033602 (2012).

[18] A. H. Safavi-Naeini, *Quantum optomechanics with silicon nanostructures*, phd, California Institute of Technology (2013).

[19] Y. Chen, "Macroscopic quantum mechanics: theory and experimental concepts of optomechanics," *Journal of Physics B: Atomic, Molecular and Optical Physics* **46**, 104001 (2013).

[20] F. Marquardt and S. M. Girvin, "Optomechanics," *Physics* **2**, 40 (2009).

[21] M. Eichenfield, J. Chan, R. M. Camacho, K. J. Vahala, and O. Painter, "Optomechanical crystals," *Nature* **462**, 78–82 (2009).

[22] P. Rabl, "Photon Blockade Effect in Optomechanical Systems," *Physical Review Letters* **107**, 063601 (2011).

[23] S. Hampshire, "Silicon nitride ceramicsreview of structure, processing and properties," *Journal of Achievements in Materials and Manufacturing Engineering* **24**, 43–50 (2007).

[24] D. W. Freitag, D. W. Richerson, and United States Advanced Ceramics Association, *Opportunities for advanced ceramics to meet the needs of the industries of the future* (Office of Industrial Technologies, Oak Ridge, Tenn., 1998).

[25] F. L. Riley, "Silicon Nitride and Related Materials," *Journal of the American Ceramic Society* **83**, 245–265 (2000).

[26] J. R. Johnston, R. A. Signorelli, and J. C. Freche, "Performance of Rocket Nozzle Materials with Several Solid Propellants." Tech. rep., Defense Technical Information Center (1966).

[27] J. Olofsson, T. M. Grehk, T. Berlind, C. Persson, S. Jacobson, and H. Engqvist, "Evaluation of silicon nitride as a wear resistant and resorbable alternative for total hip joint replacement," *Biomatter* **2**, 94–102 (2012).

[28] M. C. Anderson and R. Olsen, "Bone ingrowth into porous silicon nitride," *Journal of Biomedical Materials Research Part A* **92A**, 1598–1605 (2010).

[29] B. M. Zwickl, W. E. Shanks, A. M. Jayich, C. Yang, A. C. Bleszynski Jayich, J. D. Thompson, and J. G. E. Harris, "High quality mechanical and optical properties of commercial silicon nitride membranes," *Applied Physics Letters* **92**, 103125 (2008).

[30] D. R. Southworth, R. A. Barton, S. S. Verbridge, B. Ilic, A. D. Fefferman, H. G. Craighead, and J. M. Parpia, "Stress and Silicon Nitride: A Crack in the Universal Dissipation of Glasses," *Physical Review Letters* **102**, 225503 (2009).

[31] S. S. Verbridge, J. M. Parpia, R. B. Reichenbach, L. M. Bellan, and H. G. Craighead, "High quality factor resonance at room temperature with nanostrings under high tensile stress," *Journal of Applied Physics* **99**, 124304 (2006).

[32] J. Laconte, D. Flandre, and J.-P. Raskin, *Micromachined Thin-Film Sensors for SOI-CMOS Co-Integration* (Springer Science & Business Media, 2006).

[33] J. D. Joannopoulos, S. G. Johnson, J. N. Winn, and R. D. Meade, *Photonic Crystals: Molding the Flow of Light* (Princeton University Press, Princeton, 2008), second edition edition.

[34] M. Eichenfield, *Cavity optomechanics in photonic and phononic crystals: engineering the interaction of light and sound at the nanoscale*, phd, California Institute of Technology (2010).

[35] J. Chan, *Laser cooling of an optomechanical crystal resonator to its quantum ground state of motion*, phd, California Institute of Technology (2012).

[36] R. Pohl, X. Liu, and E. Thompson, "Low-temperature thermal conductivity and acoustic attenuation in amorphous solids," *Reviews of Modern Physics* **74**, 991–1013 (2002).

[37] R. Zeller and R. Pohl, "Thermal Conductivity and Specific Heat of Noncrystalline Solids," *Physical Review B* **4**, 2029–2041 (1971).

[38] Q. P. Unterreithmeier, T. Faust, and J. P. Kotthaus, "Damping of Nanomechanical Resonators," *Physical Review Letters* **105**, 027205 (2010).

[39] A. Suhel, B. D. Hauer, T. S. Biswas, K. S. D. Beach, and J. P. Davis, "Dissipation mechanisms in thermomechanically driven silicon nitride nanostrings," *Applied Physics Letters* **100**, 173111 (2012).

[40] I. Wilson-Rae, R. A. Barton, S. S. Verbridge, D. R. Southworth, B. Ilic, H. G. Craighead, and J. M. Parpia, "High-Q Nanomechanics via Destructive Interference of Elastic Waves," *Physical Review Letters* **106**, 047205 (2011).

[41] T. Faust, J. Rieger, M. J. Seitner, J. P. Kotthaus, and E. M. Weig, "Signatures of two-level defects in the temperature-dependent damping of nanomechanical silicon nitride resonators," *Physical Review B* **89**, 100102 (2014).

[42] S. Schmid, K. D. Jensen, K. H. Nielsen, and A. Boisen, "Damping mechanisms in high-Q micro and nanomechanical string resonators," *Physical Review B* **84**, 165307 (2011).

[43] S. Johnson, M. Ibanescu, M. Skorobogatiy, O. Weisberg, J. Joannopoulos, and Y. Fink, "Perturbation theory for Maxwells equations with shifting material boundaries," *Physical Review E* **65**, 066611 (2002).

[44] M. Eichenfield, J. Chan, A. H. Safavi-Naeini, K. J. Vahala, and O. Painter, "Modeling dispersive coupling and losses of localized optical and mechanical modes in optomechanical crystals," *Optics Express* **17**, 20078–20098 (2009).

[45] A. Weinstein, C. Lei, E. Wollman, J. Suh, A. Metelmann, A. Clerk, and K. Schwab, "Observation and Interpretation of Motional Sideband Asymmetry in a Quantum Electromechanical Device," *Physical Review X* **4**, 041003 (2014).

[46] R. A. Norte, *Nanofabrication for On-Chip Optical Levitation, Atom-Trapping, and Superconducting Quantum Circuits*, phd, California Institute of Technology (2015).

[47] ZEON Chemicals, "ZEP520A Datasheet," .

[48] M. D. Henry, *ICP etching of silicon for micro and nanoscale devices*, phd, California Institute of Technology (2010).

[49] A. B. Kaul, *Microelectronics to Nanoelectronics: Materials, Devices & Manufacturability* (CRC Press, 2012).

[50] H. Rhee, H. Kwon, C.-K. Kim, H. Kim, J. Yoo, and Y. W. Kim, "Comparison of deep silicon etching using SF6/C4F8 and SF6/C4F6 plasmas in the Bosch process," *Journal of Vacuum Science Technology B: Microelectronics and Nanometer Structures* **26**, 576–581 (2008).

[51] F. Saffih, C. Con, A. Alshammari, M. Yavuz, and B. Cui, "Fabrication of silicon nanostructures with large taper angle by reactive ion etching," *Journal of Vacuum Science & Technology B* **32**, 06FI04 (2014).

[52] O. Powell and H. B. Harrison, "Anisotropic etching of {100} and {110} planes in (100) silicon," *Journal of Micromechanics and Microengineering* **11**, 217 (2001).

[53] Y. Uenishi, M. Tsugai, and M. Mehregany, "Micro-opto-mechanical devices fabricated by anisotropic etching of (110) silicon," *Journal of Micromechanics and Microengineering* **5**, 305 (1995).

[54] K. Sato, M. Shikida, Y. Matsushima, T. Yamashiro, K. Asaumi, Y. Iriye, and M. Yamamoto, "Characterization of orientation-dependent etching properties of single-crystal silicon: effects of KOH concentration," *Sensors and Actuators A: Physical* **64**, 87–93 (1998).

[55] J. D. Cohen, S. M. Meenehan, and O. Painter, "Optical coupling to nanoscale optomechanical cavities for near quantum-limited motion transduction," *Optics Express* **21**, 11227–11236 (2013).

[56] A. H. Safavi-Naeini, S. Gröblacher, J. T. Hill, J. Chan, M. Aspelmeyer, and O. Painter, "Squeezed light from a silicon micromechanical resonator," *Nature* **500**, 185–189 (2013).

[57] A. H. Safavi-Naeini, T. P. M. Alegre, J. Chan, M. Eichenfield, M. Winger, Q. Lin, J. T. Hill, D. E. Chang, and O. Painter, "Electromagnetically induced transparency and slow light with optomechanics," *Nature* **472**, 69–73 (2011).

[58] A. G. Krause, M. Winger, T. D. Blasius, Q. Lin, and O. Painter, "A high-resolution microchip optomechanical accelerometer," *Nature Photon.* **6**, 768–772 (2012).

[59] A. H. Safavi-Naeini, T. P. M. Alegre, M. Winger, and O. Painter, "Optomechanics in an ultrahigh-Q two-dimensional photonic crystal cavity," *Applied Physics Letters* **97**, 181106 (2010).

[60] Y. Taguchi, Y. Takahashi, Y. Sato, T. Asano, and S. Noda, "Statistical studies of photonic heterostructure nanocavities with an average Q factor of three million," *Optics Express* **19**, 11916–11921 (2011).

[61] J. Chan, A. H. Safavi-Naeini, J. T. Hill, S. Meenehan, and O. Painter, "Optimized optomechanical crystal cavity with acoustic radiation shield," *Applied Physics Letters* **101**, 081115 (2012).

[62] M. Borselli, T. J. Johnson, and O. Painter, "Measuring the role of surface chemistry in silicon microphotonics," *Applied Physics Letters* **88**, 131114 (2006).

[63] G. Krishnan, C. U. Kshirsagar, G. K. Ananthasuresh, and N. Bhat, "REVIEWS Micromachined High-Resolution Accelerometers," *Journal of the Indian Institute of Science* **87**, 333–361 (2007).

[64] C. Acar and A. M. Shkel, "Experimental evaluation and comparative analysis of commercial variable-capacitance MEMS accelerometers," *Journal of Micromechanics and Microengineering* **13**, 634–645 (2003).

[65] H. Kulah, J. Chae, N. Yazdi, and K. Najafi, "Noise analysis and characterization of a sigma-delta capacitive microaccelerometer," *IEEE Journal of Solid-State Circuits* **41**, 352– 361 (2006).

[66] S. Tadigadapa and K. Mateti, "Piezoelectric MEMS sensors: state-of-the-art and perspectives," *Measurement Science and Technology* **20**, 092001 (2009).

[67] C. Liu, A. M. Barzilai, J. K. Reynolds, A. Partridge, T. W. Kenny, J. D. Grade, and H. K. Rockstad, "Characterization of a high-sensitivity micromachined tunneling accelerometer with micro-g resolution," *Journal of Microelectromechanical Systems* **7**, 235–244 (1998).

[68] U. Krishnamoorthy, R. Olsson III, G. Bogart, M. Baker, D. Carr, T. Swiler, and P. Clews, "In-plane MEMS-based nano-g accelerometer with sub-wavelength optical resonant sensor," *Sensors and Actuators A: Physical* **145146**, 283–290 (2008).

[69] K. Zandi, B. Wong, J. Zou, R. V. Kruzelecky, W. Jamroz, and Y. A. Peter, "In-plane silicon-on-insulator optical MEMS accelerometer using waveguide fabry-perot microcavity with silicon/air bragg mirrors," in *2010 IEEE 23rd International Conference on Micro Electro Mechanical Systems (MEMS)* pp. 839–842 (2010).

[70] W. Noell, P. A. Clerc, L. Dellmann, B. Guldimann, H. P. Herzig, O. Manzardo, C. R. Marxer, K. J. Weible, R. Dandliker, and N. de Rooij, "Applications of SOI-based optical MEMS," *IEEE Journal of Selected Topics in Quantum Electronics* **8**, 148–154 (2002).

[71] T. A. Berkoff and A. D. Kersey, "Experimental demonstration of a fiber Bragg grating accelerometer," *IEEE Photonics Technology Letters* **8**, 1677–1679 (1996).

[72] M. Eichenfield, R. Camacho, J. Chan, K. J. Vahala, and O. Painter, "A picogram- and nanometre-scale photonic-crystal optomechanical cavity," *Nature* **459**, 550–555 (2009).

[73] T. J. Kippenberg and K. J. Vahala, "Cavity Opto-Mechanics," *Optics Express* **15**, 17172–17205 (2007).

[74] C. Genes, D. Vitali, P. Tombesi, S. Gigan, and M. Aspelmeyer, "Ground-state cooling of a micromechanical oscillator: Comparing cold damping and cavity-assisted cooling schemes," *Physical Review A* **77**, 033804 (2008).

[75] T. Corbitt, C. Wipf, T. Bodiya, D. Ottaway, D. Sigg, N. Smith, S. Whitcomb, and N. Mavalvala, "Optical Dilution and Feedback Cooling of a Gram-Scale Oscillator to 6.9 mK," *Physical Review Letters* **99**, 160801 (2007).

[76] Q. Lin, J. Rosenberg, X. Jiang, K. J. Vahala, and O. Painter, "Mechanical Oscillation and Cooling Actuated by the Optical Gradient Force," *Physical Review Letters* **103**, 103601 (2009).

[77] P. Zwahlen, A. M. Nguyen, Y. Dong, F. Rudolf, M. Pastre, and H. Schmid, "Navigation grade MEMS accelerometer," in *2010 IEEE 23rd International Conference on Micro Electro Mechanical Systems (MEMS)* pp. 631–634 (2010).

[78] X. Jiang, F. Wang, M. Kraft, and B. E. Boser, "An Integrated Surface Micromachined Capacitive Lateral Accelerometer with 2 μG/rt-Hz resolution," *Solid-State Sensor, Actuator and Microsystems Workshop, Hilton Head Island* **2**, 2–6 (2002).

[79] V. B. Braginskii and A. B. Manukin, *Measurement of weak forces in physics experiments* (Chicago, University of Chicago Press, 1977).

[80] I. Tittonen, G. Breitenbach, T. Kalkbrenner, T. Mller, R. Conradt, S. Schiller, E. Steinsland, N. Blanc, and N. F. de Rooij, "Interferometric measurements of the position of a macroscopic body: Towards observation of quantum limits," *Physical Review A* **59**, 1038–1044 (1999).

[81] G. Anetsberger, E. Gavartin, O. Arcizet, Q. P. Unterreithmeier, E. M. Weig, M. L. Gorodetsky, J. P. Kotthaus, and T. J. Kippenberg, "Measuring nanomechanical motion with an imprecision below the standard quantum limit," *Physical Review A* **82**, 061804 (2010).

[82] C. A. Regal, J. D. Teufel, and K. W. Lehnert, "Measuring nanomechanical motion with a microwave cavity interferometer," *Nature Physics* **4**, 555–560 (2008).

[83] J. B. Hertzberg, T. Rocheleau, T. Ndukum, M. Savva, A. A. Clerk, and K. C. Schwab, "Back-action-evading measurements of nanomechanical motion," *Nature Physics* **6**, 213–217 (2009).

[84] D. Kleckner and D. Bouwmeester, "Sub-kelvin optical cooling of a micromechanical resonator," *Nature* **444**, 75–78 (2006).

[85] K. Y. Yasumura, T. D. Stowe, E. M. Chow, T. Pfafman, T. W. Kenny, B. C. Stipe, and D. Rugar, "Quality factors in micron- and submicron-thick cantilevers," *Journal of Microelectromechanical Systems* **9**, 117–125 (2000).

[86] A. A. Clerk, M. H. Devoret, S. M. Girvin, F. Marquardt, and R. J. Schoelkopf, "Introduction to quantum noise, measurement, and amplification," *Reviews of Modern Physics* **82**, 1155–1208 (2010).

[87] C. P. Michael, M. Borselli, T. J. Johnson, C. Chrystal, and O. Painter, "An optical fiber-taper probe for wafer-scale microphotonic device characterization," *Optics Express* **15**, 4745–4752 (2007).

[88] Y. T. Li, S. Y. Lee, and H. L. Pastan, "Air Damped Capacitance Accelerometers and Velocimeters," *IEEE Transactions on Industrial Electronics and Control Instrumentation* **IECI-17**, 44–48 (1970).

[89] H. V. Allen, S. C. Terry, and D. W. De Bruin, "Accelerometer systems with self-testable features," *Sensors and Actuators* **20**, 153–161 (1989).

[90] B. C. Stipe, H. J. Mamin, T. D. Stowe, T. W. Kenny, and D. Rugar, "Noncontact Friction and Force Fluctuations between Closely Spaced Bodies," *Physical Review Letters* **87**, 096801 (2001).

[91] D. Sparks, S. Massoud-Ansari, and N. Najafi, "Chip-level vacuum packaging of micromachines using NanoGetters," *Advanced Packaging, IEEE Transactions on* **26**, 277 – 282 (2003).

[92] Honeywell, *Q-Flex datasheet* (2011).

[93] M. Winger, T. D. Blasius, T. P. Mayer Alegre, A. H. Safavi-Naeini, S. Meenehan, J. Cohen, S. Stobbe, and O. Painter, "A chip-scale integrated cavity-electro-optomechanics platform," *Optics Express* **19**, 24905–24921 (2011).

[94] A. G. Krause, T. D. Blasius, and O. Painter, "Optical feedback cooling of a photonic crystal optomechanical resonator," *In preparation* (TBD).

[95] A. G. Krause, M. Winger, T. D. Blasius, Q. Lin, and O. Painter, "A high-resolution microchip optomechanical accelerometer," *Nature Photonics* **6**, 768–772 (2012).

[96] E. Gavartin, P. Verlot, and T. J. Kippenberg, "A hybrid on-chip optomechanical transducer for ultrasensitive force measurements," *Nature Nanotechnology* **7**, 509–514 (2012).

[97] R. W. Andrews, R. W. Peterson, T. P. Purdy, K. Cicak, R. W. Simmonds, C. A. Regal, and K. W. Lehnert, "Bidirectional and efficient conversion between microwave and optical light," *Nature Physics* **10**, 321–326 (2014).

[98] A. Joeckel, A. Faber, T. Kampschulte, M. Korppi, M. T. Rakher, and P. Treutlein, "Sympathetic cooling of a membrane oscillator in a hybrid mechanical-atomic system," *arXiv:1407.6820* (2014).

[99] C. Monroe, D. M. Meekhof, B. King, S. Jefferts, W. M. Itano, and D. Wineland, "Resolved-Sideband Raman Cooling of a Bound Atom to the 3D Zero-Point Energy," *Phys. Rev. Lett.* **75**, 4011–4014 (1995).

[100] S. Mancini, D. Vitali, and P. Tombesi, "Optomechanical Cooling of a Macroscopic Oscillator by Homodyne Feedback," *Phys. Rev. Lett.* **80**, 688–691 (1998).

[101] P.-F. Cohadon, A. Heidmann, and M. Pinard, "Cooling of a Mirror by Radiation Pressure," *Phys. Rev. Lett.* **83**, 3174–3177 (1999).

[102] T. Li, S. Kheifets, and M. G. Raizen, "Millikelvin cooling of an optically trapped microsphere in vacuum," *Nature Physics* **7**, 527–530 (2011).

[103] J. Gieseler, B. Deutsch, R. Quidant, and L. Novotny, "Subkelvin Parametric Feedback Cooling of a Laser-Trapped Nanoparticle," *Physical Review Letters* **109**, 103603 (2012).

[104] M. Poggio, C. L. Degen, H. J. Mamin, and D. Rugar, "Feedback Cooling of a Cantilevers Fundamental Mode below 5 mK," *Physical Review Letters* **99**, 017201 (2007).

[105] LIGO Scientific Collaboration, "Observation of a kilogram-scale oscillator near its quantum ground state," *New Journal of Physics* **11**, 073032 (2009).

[106] S. Gröblacher, J. T. Hill, A. H. Safavi-Naeini, J. Chan, and O. Painter, "Highly efficient coupling from an optical fiber to a nanoscale silicon optomechanical cavity," *Applied Physics Letters* **103**, 181104 (2013).

[107] R. M. Camacho, J. Chan, M. Eichenfield, and O. Painter, "Characterization of radiation pressure and thermal effects in a nanoscale optomechanical cavity," *Optics Express* **17**, 15726–15735 (2009).

[108] COMSOL, "COMSOL Multiphysics," . http://www.comsol.com/products/multiphysics/

[109] A. R. Kermany, G. Brawley, N. Mishra, E. Sheridan, W. P. Bowen, and F. Iacopi, "Microresonators with Q-factors over a million from highly stressed epitaxial silicon carbide on silicon," *Applied Physics Letters* **104**, 081901 (2014).

[110] D. J. Wilson, V. Sudhir, N. Piro, R. Schilling, A. Ghadimi, and T. J. Kippenberg, "Measurement and control of a mechanical oscillator at its thermal decoherence rate," *arXiv:1410.6191* (2014).

[111] A. Szorkovszky, G. A. Brawley, A. C. Doherty, and W. P. Bowen, "Strong Thermomechanical Squeezing via Weak Measurement," *Physical Review Letters* **110**, 184301 (2013).

[112] M. R. Vanner, J. Hofer, G. D. Cole, and M. Aspelmeyer, "Cooling-by-measurement and mechanical state tomography via pulsed optomechanics," *Nature Communications* **4** (2013).

[113] J. J. Gorman and B. Shapiroeds.,, *Feedback Control of MEMS to Atoms* (Springer, New York, 2011), 2012 edition edition.

[114] J. L. Garbini, K. J. Bruland, W. M. Dougherty, and J. A. Sidles, "Optimal control of force microscope cantilevers. I. Controller design," *Journal of Applied Physics* **80**, 1951–1958 (1996).

[115] T. Ando, T. Uchihashi, and T. Fukuma, "High-speed atomic force microscopy for nano-visualization of dynamic biomolecular processes," *Progress in Surface Science* **83**, 337–437 (2008).

[116] A. G. Krause, J. T. Hill, M. Ludwig, A. Safavi-Naeini, J. Chan, F. Marquardt, and O. Painter, "Controlling nonlinear dynamics in an optomechanical crystal," *In preparation* (TBD).

[117] K. Srinivasan, H. Miao, M. T. Rakher, M. Davanco, and V. Aksyuk, "Optomechanical Transduction of an Integrated Silicon Cantilever Probe Using a Microdisk Resonator," *Nano Letters* **11**, 791–797 (2011).

[118] J. T. Hill, A. H. Safavi-Naeini, J. Chan, and O. Painter, "Coherent optical wavelength conversion via cavity optomechanics," *Nature Communications* **3**, 1196 (2012).

[119] W. Marshall, C. Simon, R. Penrose, and D. Bouwmeester, "Towards Quantum Superpositions of a Mirror," *Physical Review Letters* **91**, 130401 (2003).

[120] F. Marquardt, J. G. E. Harris, and S. M. Girvin, "Dynamical Multistability Induced by Radiation Pressure in High-Finesse Micromechanical Optical Cavities," *Physical Review Letters* **96**, 103901 (2006).

[121] S. Weis, R. Rivire, S. Delglise, E. Gavartin, O. Arcizet, A. Schliesser, and T. J. Kippenberg, "Optomechanically Induced Transparency," *Science* **330**, 1520 –1523 (2010).

[122] T. Carmon, H. Rokhsari, L. Yang, T. J. Kippenberg, and K. J. Vahala, "Temporal Behavior of Radiation-Pressure-Induced Vibrations of an Optical Microcavity Phonon Mode," *Physical Review Letters* **94**, 223902 (2005).

[123] H. Rokhsari, T. Kippenberg, T. Carmon, and K. Vahala, "Radiation-pressure-driven micromechanical oscillator," *Optics Express* **13**, 5293–5301 (2005).

[124] T. J. Kippenberg, H. Rokhsari, T. Carmon, A. Scherer, and K. J. Vahala, "Analysis of Radiation-Pressure Induced Mechanical Oscillation of an Optical Microcavity," *Physical Review Letters* **95**, 033901 (2005).

[125] K. Karrai, I. Favero, and C. Metzger, "Doppler Optomechanics of a Photonic Crystal," *Physical Review Letters* **100**, 240801 (2008).

[126] T. Carmon, M. C. Cross, and K. J. Vahala, "Chaotic Quivering of Micron-Scaled On-Chip Resonators Excited by Centrifugal Optical Pressure," *Physical Review Letters* **98**, 167203 (2007).

[127] C. Metzger, M. Ludwig, C. Neuenhahn, A. Ortlieb, I. Favero, K. Karrai, and F. Marquardt, "Self-Induced Oscillations in an Optomechanical System Driven by Bolometric Backaction," *Physical Review Letters* **101**, 133903 (2008).

[128] M. Bagheri, M. Poot, M. Li, W. P. H. Pernice, and H. X. Tang, "Dynamic manipulation of nanomechanical resonators in the high-amplitude regime and non-volatile mechanical memory operation," *Nature Nanotechnology* **6**, 726–732 (2011).

[129] M. Eichenfield, J. Chan, R. M. Camacho, K. J. Vahala, and O. Painter, "Optomechanical crystals," *Nature* **462**, 78–82 (2009).

[130] T. P. M. Alegre, A. Safavi-Naeini, M. Winger, and O. Painter, "Quasi-two-dimensional optomechanical crystals with a complete phononic bandgap," *Optics Express* **19**, 5658–5669 (2011).

[131] M. I. Dykman and M. A. Krivoglaz, "Theory of fluctuational transitions between stable states of a nonlinear oscillator," *Soviet Journal of Experimental and Theoretical Physics* p. 30 (1979).

[132] I. Siddiqi, R. Vijay, F. Pierre, C. M. Wilson, M. Metcalfe, C. Rigetti, L. Frunzio, and M. H. Devoret, "RF-Driven Josephson Bifurcation Amplifier for Quantum Measurement," *Physical Review Letters* **93**, 207002 (2004).

[133] I. Siddiqi, R. Vijay, F. Pierre, C. M. Wilson, L. Frunzio, M. Metcalfe, C. Rigetti, R. J. Schoelkopf, M. H. Devoret, D. Vion, and D. Esteve, "Direct Observation of Dynamical Bifurcation between Two Driven Oscillation States of a Josephson Junction," *Physical Review Letters* **94**, 027005 (2005).

[134] P. Jung, S. Butz, M. Marthaler, M. V. Fistul, J. Leppkangas, V. P. Koshelets, and A. V. Ustinov, "Multistability and switching in a superconducting metamaterial," *Nature Communications* **5** (2014).

[135] M. Ludwig, B. Kubala, and F. Marquardt, "The optomechanical instability in the quantum regime," *New Journal of Physics* **10**, 095013 (2008).

[136] S. Gröblacher, *Quantum opto-mechanics with micromirrors: combining nano-mechanics with quantum optics* (Springer, 2012).